Università di Bologna

Dottorato di Ricerca in Geofisica

XXI Ciclo

Tesi di Dottorato

Settore scientifico-disciplinare di afferenza Geo/10

3D Probability Tomography: theoretical developments and applications to high-resolution geophysical prospecting

Dottorando:

Dr. Raffaele Alaia

Coordinatore:

Prof. Michele Dragoni

Relatore:

Prof. Domenico Patella

Esame finale anno 2009

Introduction

During the last few years geophysical methods employed in underground exploration have been constantly and substantially evolving in both physical and technological aspects.

The geophysical prospecting methods can be divided, in the first instance, into two categories, artificial source and natural source. The artificial source methods are based on the study of the observed responses on the surface of the interested volume of ground to a physical stress artificially induced in the ground. For example, the geoelectric method takes in exam the electric properties of the subsoil by studying the flux of artificially injected currents, thus allowing the retrieval of information about the electric resistivity of the surveyed ground portion. It can successfully highlight even weak resistivity contrasts that buried objects create with the hosting background.

The natural source methods, instead, base their development on the study of the fields naturally found inside the earth, as e.g. the gravimetric method. By analysing the gravitational field, it allows the properties of the matter which originated the field to be detected and hence the mass distribution below the surface to be imaged.

In synthesis, the principal aim of the geophysical studies is to retrieve information about shape, location and physical characteristics of the investigated bodies. To this purpose, it is necessary to solve the so-called "inverse problem", i.e. to determine the characteristic parameters of the buried structures, starting from a series of measures obtained on the surface. The solution to this problem is very complex because of the many solutions compatible with an acquired data set, indeed, different bodies can cause the same image on the surface.

The probability tomography approach allows the analysis of the experimental data without introducing some a priori information on the investigated structures. In the limits of the experimental accuracy, the probability tomography is able to give a geometrical representation of the buried sources of anomalies. Therefore, the main

difference with the classical inversion methods is the absence of any possibility to estimate the intrinsic physical parameters of the source bodies. In many near-surface applications, e.g. in archaeological prospection, this is not a serious limitation, since in most cases location and geometry of the sources are more than sufficient to resolve the practical problem. In the cases in which the knowledge of the intrinsic physical parameter of the bodies is essential, the results of the probability tomography can suitably used as robust geometrical constraints in any of the classical inversion routines.

Geophysical probability tomography (GPT) was proposed as an approach to virtually explore the subsoil in the search for the most probable localization of the sources of anomalies appearing in a field dataset collected in a given datum domain. It was originally formulated for the self-potential method [41,42] and then extended to the geoelectric [25,26,32], em induction [27], gravity [28,29] and magnetic [18,19,30] prospecting methods. In all of these formulations, the buried bodies responsible for the observed anomalies were considered as aggregates of small cells, definitively assimilated to poles. A pole was thus assumed to represent the physical centre of a small cell with a constant electric charge density in the self-potential and, mass density in gravity and resistivity in geoelectrics. GPT sensitivity and resolution power have been and are still widely and successfully tested on synthetic and experimental data in many application fields [6,7,8,12,13,24,43,53] .

An extension of the GPT theory has been recently proposed [32] by postulating that some given geophysical dataset can be viewed as the simultaneous response of a double set of buried physical sources, say poles and dipoles. In this new formulation, while poles hold the original meaning as explained above, dipoles, instead, are assumed to simulate sharp boundary elements. The two-source GPT approach has been shown to provide a more reliable depiction of the most probable spatial collocation and extent of source bodies [1].

This thesis is composed of two parts. The first part , theoretical and methodological, has been addressed to the development of the GPT method to multipole source analysis in order to obtain more information on the shape and the position of the sources of the experimentally detected anomalies.

We develop the theory of the generalized 3D GPT to image source poles, dipoles, quadrupoles and octopoles, from a generic geophysical vector or scalar field dataset [2,3,4].

The generalised 3D GPT method is described by first assuming that any geophysical field dataset can be hypothesized to be caused by a discrete number of source poles, dipoles, quadrupoles and octopoles.

Then, the theoretical derivation of the source pole occurrence probability (SPOP) and source dipole occurrence probability (SDOP) tomography, previously published in detail for single geophysical methods, is symbolically restated in the most general way. Finally, the theoretical derivation of the source quadrupole occurrence probability tomography (SQOP) and source octopole occurrence probability tomography (SOOP) are given following a formal development similar to those of the SPOP and SDOP tomography.

These elementary sources are used to image, in the most complete way and without any a priori assumption, shape and position of the most probable anomaly source bodies, by picking out the location of the centres and of peculiar points of the boundaries, such as corners, wedges and vertices. In this new formulation, poles and dipoles still have the original meaning to represent centres and boundaries, respectively, of elementary bodies with constant constitutive parameters, while quadrupoles and octopoles are assumed to simulate sharp corners, wedges and vertices elements. The purpose of multipole analysis is to improve the resolution power of geophysical methods, using once more probability as a suitable paradigm allowing all possible equivalent solutions to be included into a unique 3D tomography image.

The second part is dedicated to the application of the developed theory to synthetic data for method testing and to real data for a comparison with the previous inversion results. The innovative aspects and the improvements of this method for the 3D tomographic imaging of buried targets is discussed in detail.

The applications fields have been archaeology for near-surface analysis and vulcanology for deep analysis.

In particular, for the near-surface analysis in archaeological prospection, a geoelectrical survey was planned in an unexplored site of the archaeological park of Pompei.

For the deep analysis in volcanological prospection, the experimental data taken into consideration are related to a gravity survey carried out in the volcanic area of Mount Etna (Sicily, Italy), and an SP dataset collected in the Mt. Somma-Vesuvius volcanic district (Naples, Italy).

1. Multipole Geophysical Tomography

1.1 General theory

Consider a reference coordinate system with a horizontal (x,y)-plane and the z-axis positive downwards, and a 2D datum domain S as in figure 1.1. The S-domain is generally a non-flat ground survey area characterised by a topographic function $z(x,y)$.

Let $\mathbf{A}(\mathbf{r})$ be a vector anomaly function at a set of datum points $\mathbf{r}\equiv(x,y,z)$, with $\mathbf{r}\in S$, we assume that $\mathbf{A}(\mathbf{r})$ can be discretised as

$$\mathbf{A}\left(\mathbf{r}\right)=\sum_{m=1}^{M}(\mathbf{p}_m\cdot\mathbf{P}_m)\mathbf{s}(\mathbf{r},\mathbf{r}_m)+\sum_{n=1}^{N}(\mathbf{d}_n^u\cdot\mathbf{L}_n^u)\mathbf{s}(\mathbf{r},\mathbf{r}_n)$$

$$+\sum_{g=1}^{G}(\mathbf{q}_g^{uv}\cdot\mathbf{S}_g^{uv})\mathbf{s}(\mathbf{r},\mathbf{r}_g)+\sum_{h=1}^{H}(\mathbf{o}_h^{uvw}\cdot\mathbf{C}_h^{uvw})\mathbf{s}(\mathbf{r},\mathbf{r}_h) \tag{1.1}$$

i.e. as a sum of effects due to:

- a set of M poles, the mth element of which is located at $\mathbf{r}_m\equiv(x_m,y_m,z_m)$ and has strength $\mathbf{p}_m\cdot\mathbf{P}_m$, where $\mathbf{p}_m$ and $\mathbf{P}_m$ are the pole moment and a point operator zero-order tensor, respectively;

- a set of N dipoles, whose nth element is located at $\mathbf{r}_n\equiv(x_n,y_n,z_n)$ with strength $(\mathbf{d}_n^u\cdot\mathbf{L}_n^u)$ $(u=x,y,z)$, where $\mathbf{d}_n^u$ and $\mathbf{L}_n^u$ are the dipole moment and a line operator first-order tensor, respectively;

- a set of G quadrupoles, whose gth element is located at $\mathbf{r}_g\equiv(x_g,y_g,z_g)$ with strength $\mathbf{q}_g^{uv}\cdot\mathbf{S}_g^{uv}$ $(u,v=x,y,z)$, where $\mathbf{q}_g^{uv}$ and $\mathbf{S}_g^{uv}$ are the quadrupole moment and a square operator second-order tensor, respectively;

- a set of *H* octopoles, whose *h*th element is located at $\mathbf{r}_h \equiv (x_h, y_h, z_h)$ and has strength $\mathbf{o}_h^{uvw} \cdot \mathbf{C}_h^{uvw}$ $(u,v,w=x,y,z)$, where $\mathbf{o}_h^{uvw}$ and $\mathbf{C}_h^{uvw}$ are the octopole moment and a cube operator third-order tensor, respectively.

The dot in the definition of the source strength tensors indicates inner product. The operator tensors $\mathbf{P}, \mathbf{L}^u, \mathbf{S}^{uv}$ and $\mathbf{C}^{uvw}$ $(u,v,w=x,y,z)$ are explicated in figure 1.2 .

The effect of the *M, N, G* and *H* source elements at a point $\mathbf{r} \in S$ is determined by the same kernel function $s(\mathbf{r}, \mathbf{r}_i)$, $(i=m,n,g,h)$.
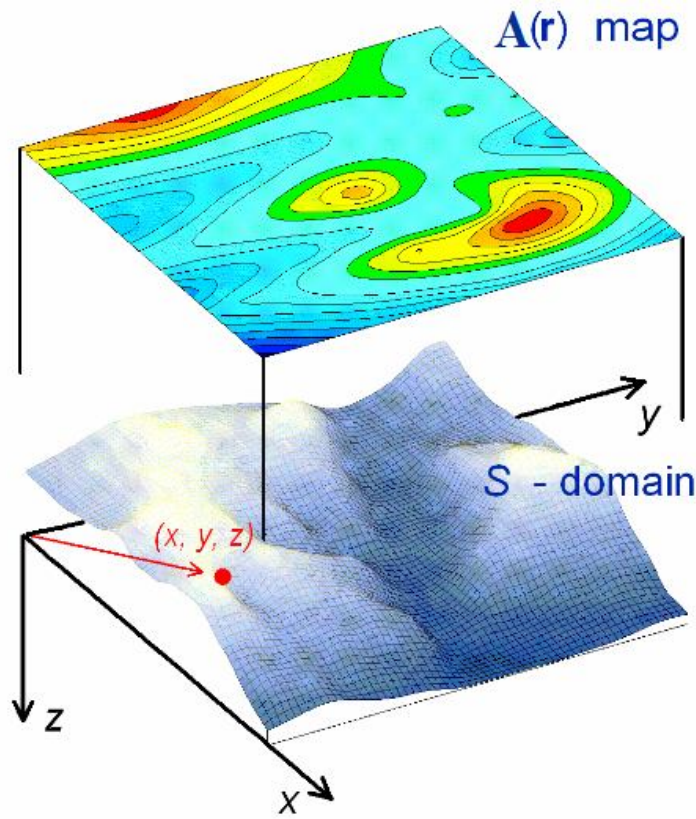

Figure 1.1 The datum domain (*S*-domain) generating the $\mathbf{A}(\mathbf{r})$ map on top. The (*x,y*)-plane is placed at sea level and the *z*-axis points into the earth.

We define the information power Λ, associated with $\mathbf{A}(\mathbf{r})$, over the surface *S* as

$$\Lambda = \int_S \mathbf{A}(\mathbf{r}) \cdot \mathbf{A}(\mathbf{r}) dS \tag{1.2}$$

which, using eq. 1.1, is expanded as

$$\Lambda = \sum_{m=1}^{M} p_m \int_S \mathbf{A}(\mathbf{r}) \cdot \mathbf{s}(\mathbf{r}, \mathbf{r}_m) \mathrm{d}S$$

$$+ \sum_{n=1}^{N} \sum_{u=x,y,z} d_n^u \int_S \mathbf{A}(\mathbf{r}) \cdot \frac{\partial \mathbf{s}(\mathbf{r}, \mathbf{r}_n)}{\partial u_n} \mathrm{d}S$$

$$+ \sum_{g=1}^{G} \sum_{u=x,y,z} \sum_{v=x,y,z} q_g^{uv} \int_S \mathbf{A}(\mathbf{r}) \cdot \frac{\partial^2 \mathbf{s}(\mathbf{r}, \mathbf{r}_g)}{\partial u_g \partial v_g} dS$$

$$+ \sum_{h=1}^{H} \sum_{u=x,y,z} \sum_{v=x,y,z} \sum_{w=x,y,z} o_h^{uvw} \int_S \mathbf{A}(\mathbf{r}) \cdot \frac{\partial^3 \mathbf{s}(\mathbf{r}, \mathbf{r}_h)}{\partial u_h \partial v_h \partial w_h} dS \qquad (1.3)$$
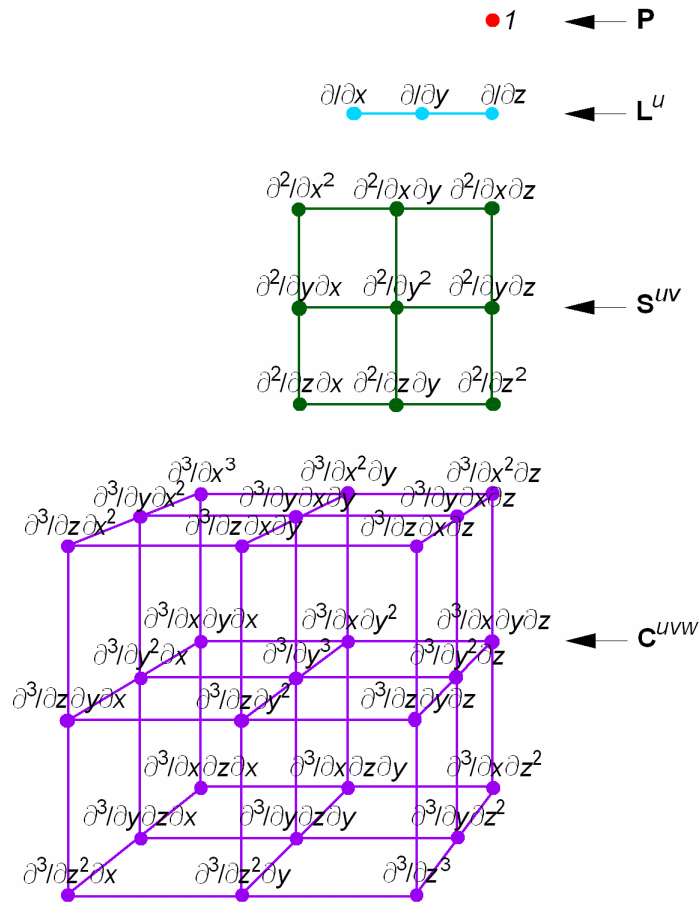

Figure 1.2 Explicit representation of the symbolic tensor operators appearing in the definition of the strengths of the pole, dipole, quadrupole and octopole source elements defined in eq. 1.1.

1.2 The source pole occurrence probability

We consider a generic mth integral of the first sum in eq. 1.3 and apply Schwarz's inequality, thus obtaining

$$\left[\int_S \mathbf{A}(\mathbf{r}) \cdot \mathbf{s}(\mathbf{r}, \mathbf{r}_m) dS \right]^2 \leq \int_S A^2(\mathbf{r}) dV \int_S s^2(\mathbf{r}, \mathbf{r}_m) dS \qquad (1.4)$$

where $A(\mathbf{r})$ and $s(\mathbf{r}, \mathbf{r}_m)$ are the modulus of $\mathbf{A}(\mathbf{r})$ and $\mathbf{s}(\mathbf{r}, \mathbf{r}_m)$, respectively.

Inequality 4 is used to define a *source pole occurrence probability* (SPOP) function [2,28] as

$$\eta_m^{(p)} = C_m^{(p)} \int_S \mathbf{A}(\mathbf{r}) \cdot \mathbf{s}(\mathbf{r}, \mathbf{r}_m) dS \qquad (1.5)$$

where

$$C_m^{(p)} = \left[\int_S A^2(\mathbf{r}) dS \int_S s^2(\mathbf{r}, \mathbf{r}_m) dS \right]^{-1/2} \qquad (1.6)$$

The 3D SPOP function, which satisfies the condition $-1 \leq \eta_m^{(p)} \leq 1$, is given as a measure of the probability of a source pole of strength p_m placed at $\mathbf{r}_m$, being responsible for the observed anomaly field $\mathbf{A}(\mathbf{r})$. The $\eta_m^{(P)}$ function can readily be computed knowing the mathematical expression of the function $\mathbf{s}(\mathbf{r}, \mathbf{r}_m)$, which is given the role of *source pole scanner*.

For computational purposes, we assume the projection of S onto the (x,y)-plane can be fitted to a rectangle R of sides $2X$ and $2Y$ along the x- and y-axis, respectively. Using the topography surface regularization factor $g(z)$ given by [28,29]

$$g(z_t) = \left[1 + (\partial z / dx)^2 + (\partial z / dy)^2\right]^{1/2} \tag{1.7}$$

eq. 1.5 is definitely written as follows

$$\eta_m^{(p)} = C_m^{(p)} \int\limits_{-X}^{+X} \int\limits_{-Y}^{+Y} \mathbf{A}(\mathbf{r}) \cdot \mathbf{s}(\mathbf{r}, \mathbf{r}_m) g(z) dx dy \tag{1.8}$$

with

$$C_m^{(p)} = \left[\int\limits_{-X}^{+X} \int\limits_{-Y}^{+Y} A^2(\mathbf{r}) g(z) dx dy \cdot \int\limits_{-X}^{+X} \int\limits_{-Y}^{+Y} s^2(\mathbf{r}, \mathbf{r}_m) g(z) dx dy\right]^{-1/2} \tag{1.9}$$

1.3 The source dipole occurrence probability

We take a generic nth integral of the second sum in eq. 1.3 and apply, as previously, Schwarz's inequality to each u-component ($u=x,y,z$). We can thus define a *source dipole occurrence probability* (SDOP) function [2,18] as

$$\eta_{n,u}^{(d)} = C_{n,u}^{(d)} \int\limits_{-X}^{+X} \int\limits_{-Y}^{+Y} \mathbf{A}(\mathbf{r}) \cdot \frac{\partial \mathbf{s}(\mathbf{r}, \mathbf{r}_n)}{\partial u_n} g(z) dx dy \tag{1.10}$$

with

$$C_{n,u}^{(d)} = \left[\int\limits_{-X}^{+X} \int\limits_{-Y}^{+Y} \mathbf{A}(\mathbf{r}) g(z) dx dy \cdot \int\limits_{-X}^{+X} \int\limits_{-Y}^{+Y} \left|\frac{\partial \mathbf{s}(\mathbf{r}, \mathbf{r}_n)}{\partial u_n}\right|^2 g(z) dx dy\right]^{-1/2} \tag{1.11}$$

where surface regularization has been accounted for.

Also $\eta_{n,u}^{(d)}$ falls in the range [-1,1]. Thus, at each $\mathbf{r}_n$, 3 values of $\eta_{n,u}^{(d)}$ can be computed. They are interpreted to give a probability measure, with which a single source dipole located at $\mathbf{r}_n$ can be retained responsible of the whole $\mathbf{A}(\mathbf{r})$ field.

Each first derivative of $s(\mathbf{r},\mathbf{r}_n)$ takes the role of *source dipole scanner*.

1.4 The source quadrupole occurrence probability

Accordingly, we consider now a generic *g*th integral of the third sum in eq. 1.3 and apply again Schwarz's inequality to each *uv*-element (*u,v=x,y,z*), which is used to define the *source quadrupole occurrence probability* (SQOP) function [2] as

$$\eta_{g,uv}^{(q)} = C_{g,uv}^{(q)} \int\limits_{-X}^{+X} \int\limits_{-Y}^{+Y} \mathbf{A}(\mathbf{r}) \cdot \frac{\partial^2 \mathbf{s}(\mathbf{r},\mathbf{r}_g)}{\partial u_g \partial v_g} g(z) dx dy \tag{1.12}$$

with

$$C_{g,uv}^{(q)} = \left[\int\limits_{-X}^{+X} \int\limits_{-Y}^{+Y} A^2(\mathbf{r}) g(z) dx dy \cdot \int\limits_{-X}^{+X} \int\limits_{-Y}^{+Y} \left| \frac{\partial^2 \mathbf{s}(\mathbf{r},\mathbf{r}_g)}{\partial u_g \partial v_g} \right|^2 g(z) dx dy \right]^{-1/2} \tag{1.13}$$

As previously, also the 3D SQOP function falls in the range [-1,1]. Thus, at each $\mathbf{r}_g$, 9 values of $\eta_{g,uv}^{(q)}$ are taken as a measure of the probability for a quadrupole source located at $\mathbf{r}_g$, to be responsible of the $\mathbf{A}(\mathbf{r})$ dataset. Since $\mathbf{S}_g^{uv}$ is a symmetric square tensor, it follows $\eta_{g,uv}^{(q)} = \eta_{g,vu}^{(q)}$. Hence, at each $\mathbf{r}_g$, the 3 diagonal plus the 3 right-up or left-down off-diagonal terms of $\eta_{g,uv}^{(q)}$ are sufficient.

Each second derivative of $s(\mathbf{r},\mathbf{r}_g)$ has the role of *source quadrupole scanner*.

1.5 The source octopole occurrence probability

Finally, we consider a generic hth integral of the fourth sum in eq. 1.3 and apply again Schwarz's inequality to each uvw-term ($u,v,w=x,y,z$), allowing a *source octopole occurrence probability* (SOOP) function [3,4] to be defined as

$$\eta_{h,uvw}^{(o)} = C_{h,uvw}^{(o)} \int\limits_{-X}^{+X} \int\limits_{-Y}^{+Y} \mathbf{A}(\mathbf{r}) \cdot \frac{\partial^3 \mathbf{s}(\mathbf{r},\mathbf{r}_h)}{\partial u_h \partial v_h \partial w_h} g(z) dx dy \tag{1.14}$$

with

$$C_{h,uvw}^{(o)} = \left[\int\limits_{-X}^{+X} \int\limits_{-Y}^{+Y} A^2(\mathbf{r}) g(z) dx dy \cdot \int\limits_{-X}^{+X} \int\limits_{-Y}^{+Y} \left| \frac{\partial^3 \mathbf{s}(\mathbf{r},\mathbf{r}_h)}{\partial u_h \partial v_h \partial w_h} \right|^2 g(z) dx dy \right]^{-1/2} \tag{1.15}$$

As previously, the 3D SOOP function falls in the range [-1,1]. At each $\mathbf{r}_h$, 27 values of $\eta_{h,uvw}^{(o)}$ may be calculated, which are interpreted as a measure of the probability of a single source octopole located at $\mathbf{r}_h$, being responsible of the whole $\mathbf{A}(\mathbf{r})$ dataset. However, as we are interested in finding only the position of the vertices of a source body, we will limit our analysis only to the SOOP function with $u \neq v \neq w$.

Each third derivative of $s(\mathbf{r},\mathbf{r}_h)$ takes the role of *source octopole scanner.*

2. Multipole Geoelectrical Tomography

2.1 The basic geoelectrical theory

The fundamental physical law used in resistivity surveys is Ohm's Law that governs the flow of current in the ground. The equation for Ohm's Law in vector form for current flow in a continuous medium is given by

$$\mathbf{J} = \boldsymbol{\sigma} \cdot \mathbf{E} \qquad (2.1)$$

where $\boldsymbol{\sigma}$ $(\Omega \cdot m)^{-1}$ is the conductivity of the medium, $\mathbf{J}$ (A/m^2) is the current density and $\mathbf{E}$ (V/m), is the electric field intensity. In practice, what is measured is the electric field potential. We note that in geophysical surveys the medium resistivity $\boldsymbol{\rho}$, which is equals to the reciprocal of the conductivity $\boldsymbol{\rho} = 1/\boldsymbol{\sigma}$, is more commonly used. The relationship between the electric potential U (Volt) and the field intensity is given by

$$\mathbf{E} = -\nabla U \qquad (2.2)$$

Combining equations (2.1) and (2.2), we get

$$\mathbf{J} = -\boldsymbol{\sigma} \nabla U \qquad (2.3)$$

In almost all surveys, the current sources are in the form of point sources. In this case, over an elemental volume ΔV surrounding the a current source I, located at (x_s, y_s, z_s) the relationship between the current density and the current [11] is given by

$$\nabla \cdot \mathbf{J} = \left(\frac{I}{\Delta V} \right) \delta(x - x_s) \delta(y - y_s) \delta(z - z_s) \qquad (2.4)$$

where δ is the Dirac delta function. Equation (2.4) can then be rewritten as

$$-\nabla \cdot \left[\boldsymbol{\sigma}(x,y,z) \cdot \nabla U(x,y,z) \right] = \left(\frac{I}{\Delta V} \right) \delta(x - x_s)\delta(y - y_s)\delta(z - z_s) \tag{2.5}$$

This is the basic equation that gives the potential distribution in the ground due to a point current source. A large number of techniques have been developed to solve this equation. This is the "forward" modeling problem, i.e. to determine the potential that would be observed over a given subsurface structure. Fully analytical methods have been used for simple cases, such as a sphere in a homogenous medium or a vertical fault between two areas each with a constant resistivity. For an arbitrary resistivity distribution, numerical techniques are more commonly used.

We consider simplest case with a homogeneous subsurface and a single point current source on the ground surface (figure 2.1). In this case, the current flows radially away from the source, and the potential varies inversely with distance from the current source. The equipotential surfaces have a hemisphere shape, and the current flow is perpendicular to the equipotential surface. The potential in this case is given by

$$U(r) = \frac{\rho I}{2\pi r} \tag{2.6}$$

where r is the distance of a point in the medium (including the ground surface) from the electrode.

In practice, all resistivity surveys use at least two current electrodes, a positive current and a negative current sources and two electrodes of measurement (for the potential difference). A typical arrangement with 4 electrodes is shown in figure 2.2.

The potential difference is then given by

$$\Delta U_{MN} = \left(U_{AM} + U_{BM} \right) - \left(U_{AN} + U_{BN} \right) = \frac{I\rho}{2\pi} \left[\left(\frac{1}{r_{AM}} - \frac{1}{r_{BM}} \right) - \left(\frac{1}{r_{AN}} - \frac{1}{r_{BN}} \right) \right] \tag{2.7}$$

The above equation gives the potential that would be measured over a homogenous half space with a 4 electrodes array.

Actual field surveys are invariably conducted over an inhomogenous medium where the subsurface resistivity has a 3-D distribution.
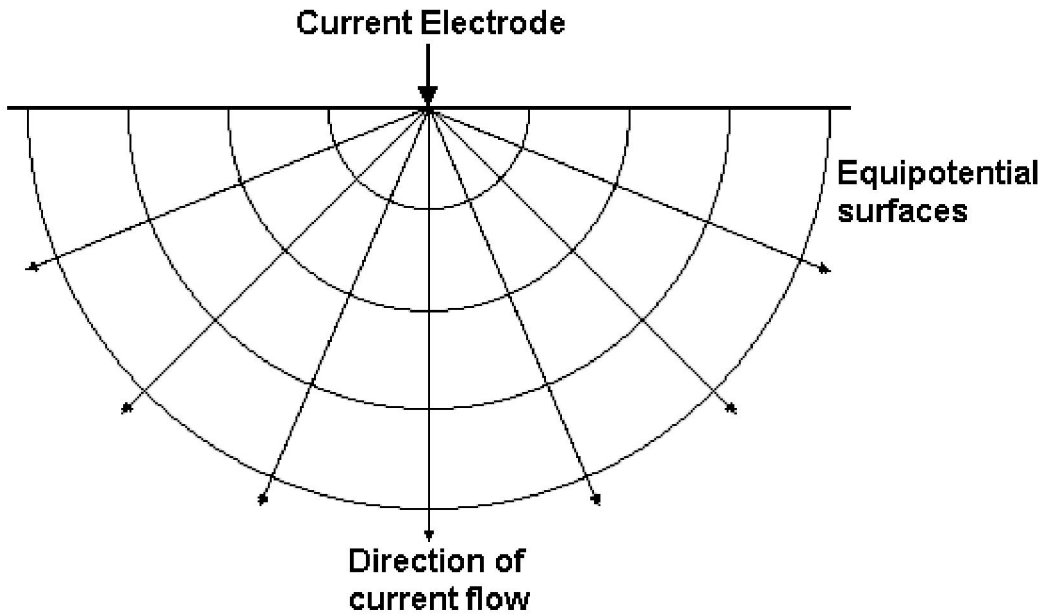

Figure 2.1 The flow of current from a point current source and the resulting potential distribution.

The resistivity measurements are still made by injecting current into the ground through the two current electrodes (A and B in figure 2.2), and measuring the resulting voltage difference at two potential electrodes (M and N). From the current (I) and potential (ΔU_{MN}) values, an apparent resistivity (ρ_a) value is calculated.

$$\rho = K_g \frac{\Delta U_{MN}}{I} \tag{2.8}$$

k_g is a geometric factor that depends on the arrangement of the four electrodes.
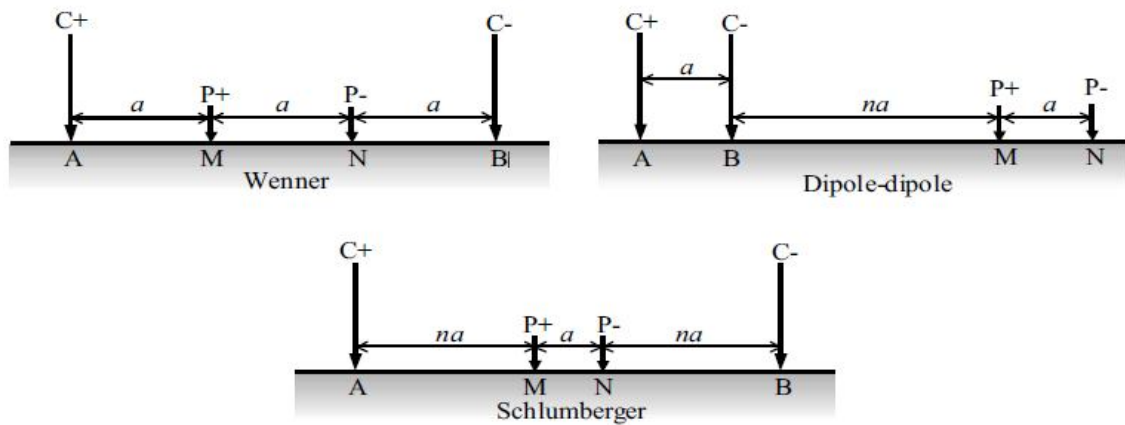
Figure 2.2 Example surface electrode configurations

The calculated resistivity value is not the true resistivity of the subsurface, but an "apparent" value that is the resistivity of a homogeneous ground that will give the same resistance value for the same electrode arrangement. The relationship between the "apparent" resistivity and the "true" resistivity is a complex relationship. To determine the true subsurface resistivity from the apparent resistivity values is the "inversion" problem.

2.2 The generalized formalism for geoelectrical method

To approach the geoelectric problem, we assume, for the sake of simplicity and without loss of generality, that the volume *V* in figure 2.3 is a rectangular prism with its upper surface *S* representing a portion of a flat ground level. We also assume that the apparent resistivity values are attributed to the nodes of a 3D regular grid filling *V*, each identified by a tern of integer numbers *i,j,k* specifying the position along the *x,y,z* axes, respectively, originating from a point arbitrarily chosen over *S*.
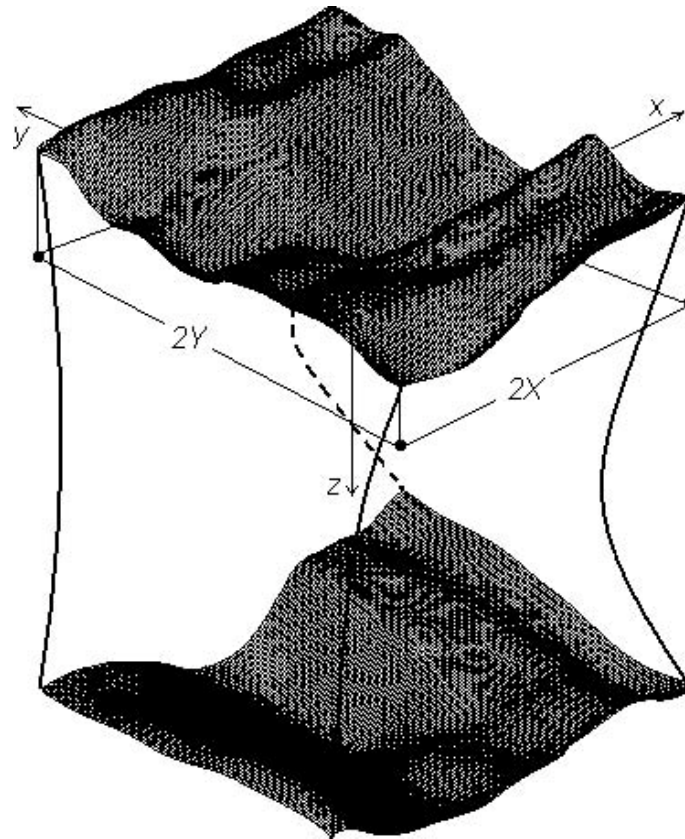
Figure 2.3 The 3D datum domain, characterized by irregular boundary surfaces. The (*x*,*y*)-plane is placed at sea level and the *z*-axis points into the earth .

In geoelectrics, the anomaly and kernel functions are scalar quantities. In order to obtain the explicit expressions of $A(\mathbf{r})$ and $s(\mathbf{r})$ we proceed as follows. We consider a homogeneous half-space with resistivity ρ_0, where a perturbation of resistivity, say $\Delta\rho_m=\rho_m-\rho_0\neq0$, is introduced at a generic single pole with coordinates (x_m,y_m,z_m). The apparent resistivity $\rho_a(i,j,k)$ of such a weakly perturbed model, where neither dipole nor quadrupole effects can generate, is approximated by a Taylor's expansion stopped to Born approximation, *i.e.* to the first derivative term, as

$$\rho_a(i,j,k) \approx \rho_0 + \frac{\partial\rho_a(i,j,k)}{\partial\rho_m}\bigg|_{\rho_m=\rho_0} \Delta\rho_m \qquad (2.9)$$

Using eq. 2.9, we readily construct the geoelectrical anomaly function as

$$A(\mathbf{r}) = \Delta\rho_a(i,j,k) = \rho_a(i,j,k) - \rho_0 \qquad (2.10)$$

and the kernel function as

$$s(\mathbf{r},\mathbf{r}_m) = \left.\frac{\partial\rho_a(i,j,k)}{\partial\rho_m}\right|_{\rho_m=\rho_0} \qquad (2.11)$$

In practice, the geoelectrical anomaly function $\Delta\rho_a(i,j,k)$ is calculated by subtracting from the measured apparent resistivities $\rho_a(i,j,k)$ a reference uniform resistivity, which can be either the background resistivity of the medium hosting the target bodies, if known, or, alternatively, any other reasonable value, as, *e.g.*, the average apparent resistivity. The geoelectrical anomaly function has thus a quite obvious relative meaning, as it represents the responses of whatever bodies which are assigned true resistivities differing from ρ_0.

For the calculation of the kernel function $\partial\rho_a(i,j,k)/\partial\rho_m\big|_{\rho_m=\rho_0}$, (appendix a), the reader can refer to an expanded version reported in previous papers [1,2,26], which was derived using the Frechet derivative [40] of the geoelectric potential, obtained by Loke and Barker [23].

Once the key functions $A(\mathbf{r})$ and $s(\mathbf{r})$ have been defined, we can readily apply the general 3D GPT theory, previously exposed, by admitting that the anomaly sources responsible of any $\Delta\rho_a(i,j,k)$ dataset can generally be made of M poles, each with its own strength $\Delta\rho_m$ ($m=1,2,..,M$), N dipoles, each with its own 3 moment vector components $\Delta\rho_n\Delta u_n$ ($n=1,2,..,N$; $u=x,y,z$), and G quadrupoles, each with its own 9 moment tensor elements $\Delta\rho_g\Delta u_g\Delta\upsilon_g$ ($g=1,2,..,G$; $u,\upsilon=x,y,z$). Eq. 1.1 is therefore explicated as follows

$$\Delta\rho_a(i,j,k) = \sum_{m=1}^{M}\Delta\rho_m\left.\frac{\partial\rho_a(i,j,k)}{\partial\rho_m}\right|_{\rho_m=\rho_0} + \sum_{n=1}^{N}\sum_{v=x,y,z}\Delta\rho_n\Delta u_n\left.\frac{\partial^2\rho_a(i,j,k)}{\partial\rho_n\partial v_n}\right|_{\rho_n=\rho_0} +$$

$$\sum_{g=1}^{G}\sum_{u=x,y,z}\sum_{\upsilon=x,y,z}\Delta\rho_g\Delta u_g\Delta\upsilon_g\left.\frac{\partial^3\rho_a(i,j,k)}{\partial\rho_g\partial u_g\partial\upsilon_g}\right|_{\rho_g=\rho_0} \qquad (2.12)$$

Skipping all intermediate steps, we directly arrive at the explicit expressions of the geoelectrical SPOP, SDOP and SQOP functions, using a discretised version of the integrals appearing in the pair of eq.s 1.8 and 1.9, eq.s 1.10 and 1.11 and eq.s 1.12 and 1.13. The geoelectrical 3D SPOP function is given as [1]

$$\eta_m^{(P)} = C_m^{(P)} \sum_{i,j,k} \Delta \rho_a(i,j,k) \frac{\partial \rho_a(i,j,k,)}{\partial \rho_m}\bigg|_{\rho_m = \rho_0} \tag{2.13}$$

with

$$C_m^{(P)} = \left\{ \sum_{i,j,k} \Delta \rho_a^2(i,j,k) \cdot \sum_{i,j,k} \left[\frac{\partial \rho_a(i,j,k)}{\partial \rho_m}\bigg|_{\rho_m = \rho_0} \right]^2 \right\}^{-1/2} \tag{2.14}$$

The geoelectrical 3D SDOP function is given as [1]

$$\eta_{n,u}^{(D)} = C_{n,u}^{(D)} \sum_{i,j,k} \Delta \rho_a(i,j,k) \frac{\partial^2 \rho_a(i,j,k,)}{\partial \rho_n \partial v_n}\bigg|_{\rho_n = \rho_0} \quad , (u = x,y,z) \tag{2.15}$$

with

$$C_{n,u}^{(D)} = \left\{ \sum_{i,j,k} \Delta \rho_a^2(i,j,k) \cdot \sum_{i,j,k} \left[\frac{\partial^2 \rho_a(i,j,k)}{\partial \rho_n \partial u_n}\bigg|_{\rho_n = \rho_0} \right]^2 \right\}^{-1/2} \quad , (u = x,y,z) \tag{2.16}$$
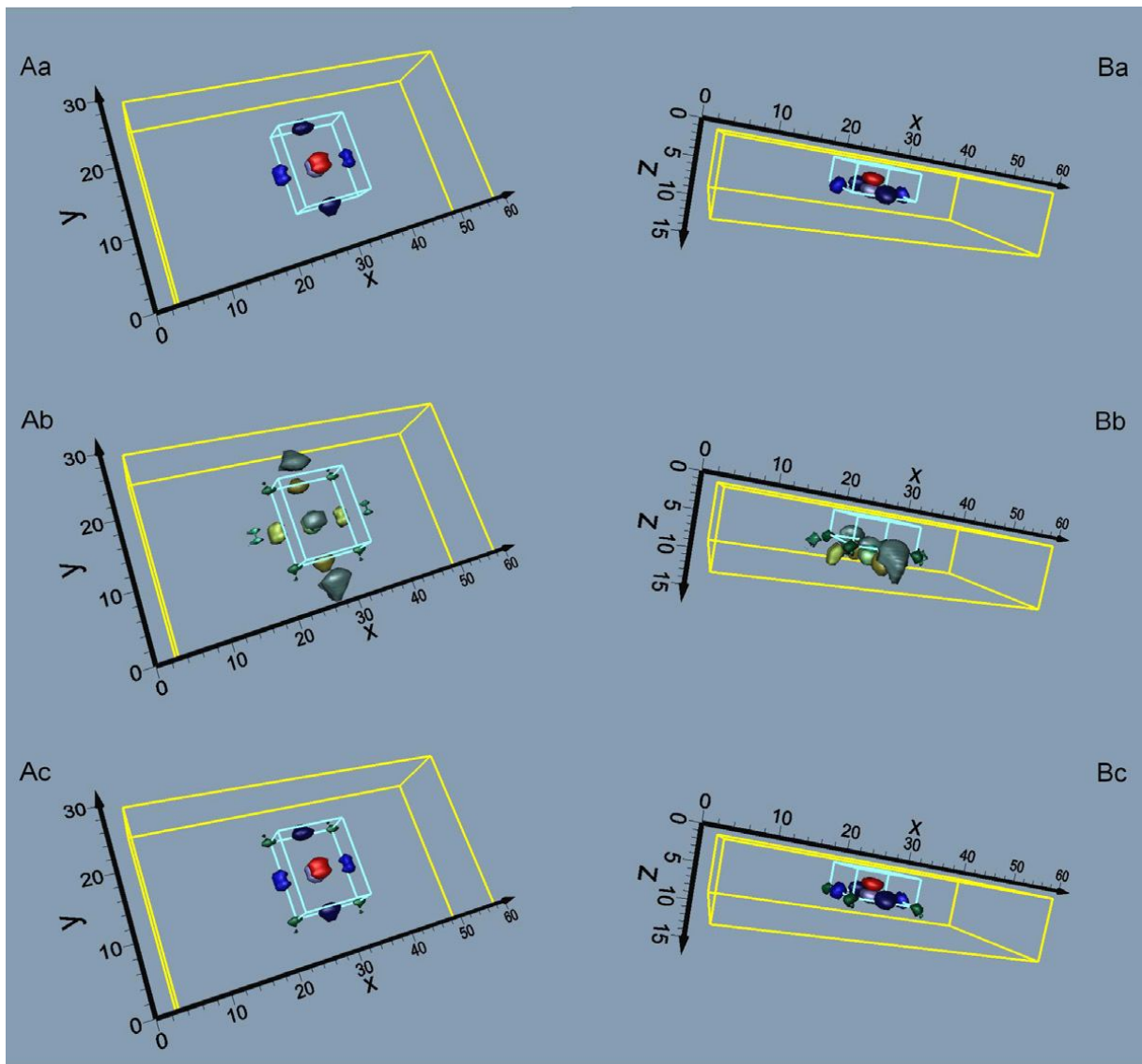
Finally, the geoelectrical 3D SQOP function is given as [2]

$$\eta_{g,uv}^{(Q)} = C_{g,uv}^{(Q)} \sum_{i,j,k} \Delta \rho_a(i,j,k) \frac{\partial^3 \rho_a(i,j,k,)}{\partial \rho_g \partial u_g \partial v_g}\bigg|_{\rho_g = \rho_0} \quad , (u,v = x,y,z) \tag{2.17}$$
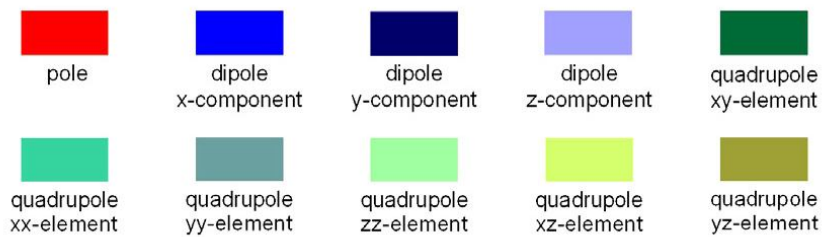
with

$$C_{g,u\upsilon}^{(Q)} = \left\{ \sum_{i,j,k} \Delta \rho_a^2(i,j,k) \cdot \sum_{i,j,k} \left[\left. \frac{\partial^3 \rho_a(i,j,k)}{\partial \rho_g \partial u_g \partial \upsilon_g} \right|_{\rho_g=\rho_0} \right]^2 \right\}^{-1/2} , (u,\upsilon=x,y,z) \qquad (2.18)$$

2.3 Synthetic examples

We show a few simple synthetic examples in order to highlight the main aspects of the SQOP tomography. In all of the examples, the new SQOP tomography will always be compared with the SPOP and SDOP tomographies in order to elicit complementary aspects. The first case is a rectangular prism with resistivity of 5000 Ω m , immersed in a homogeneous half-space with resistivity of 500 Ω m, reproduced in all templates of figures 2.4a and 2.4b with light blue lines, where the bigger prism with yellow lines represents the datum volume V, and columns A and B display the same results under different viewing angles.

coordinates of the prism corners: x-axis 25 and 37 m; y-axis 8 and 22 m; z-axis 2.5 and 7.5 m

pole	dipole x-component	dipole y-component	dipole z-component	quadrupole xy-element

quadrupole xx-element	quadrupole yy-element	quadrupole zz-element	quadrupole xz-element	quadrupole yz-element

(*a*)

Figure 2.4 (a) The SPOP, SDOP and SQOP 3D GPT for a rectangular prism of 5000 Ω m (bordered by light blue lines) and spatial location as in legend, immersed in a homogenous half space of 500 Ω m. The larger prism bordered by yellow lines is the 3D datum domain. Scale of axes is in m. For the isosurfaces bounding the coloured nuclei, containing the SPOP, SDOP and SQOP primary MAV, see table 2.1 appendix b. (*b*) The SPOP, SDOP and SQOP 3D GPT for a rectangular prism of 5000 Ω m (bordered by light blue lines) and spatial location as in legend, buried in a homogenous half space of 500 Ω m. The prism with yellow borders is the datum domain. The scale of axes is in m. For the isosurfaces bounding the coloured small (row a) and big (row b) nuclei, containing the SPOP, SDOP and SQOP MAV, see table 2.2 appendix b.

In figure 2.4a the $\eta_m^{(P)}$, $\eta_{n,u}^{(D)}$ ($u=x,y,z$) and $\eta_{g,xy}^{(Q)}$ primary maximum absolute values (MAV) are considered, which, for the sake of visibility, are each represented by a nucleus bounded by the isosurface relative to 95% of the corresponding primary MAV (table 2.1 appendix b). Row a refers to the combination of SPOP and SDOP nuclei, which confirm known results [32].

In fact, a $\eta_m^{(P)}$ nucleus, a pair of $\eta_{n,x}^{(D)}$ and $\eta_{n,y}^{(D)}$ nuclei and a $\eta_{n,z}^{(D)}$ appear in correspondence to the centre, close to the lateral faces oriented along the x- and y-axes and at the base of the prism, respectively.

Row b shows the position of the six SQOP nuclei, drawn as before by considering the isosurface relative to 95% of the corresponding primary MAV (table 2.1 appendix b). Of all of them, only the $\eta_{g,xy}^{(Q)}$ nuclei are assumed to give additional information. In fact, they appear located close to the prism basal vertices, whereas the other $\eta_{g,uv}^{(Q)}$ nuclei confirm the position of the prism central axis and its lateral and bottom faces.

Finally, row c shows the set of $\eta_m^{(P)}$, $\eta_{n,u}^{(D)}$ ($u=x,y,z$) and $\eta_{g,xy}^{(Q)}$ nuclei, which are assumed to provide a sufficient set of information as to the prism spatial location. One gets the impression that the $\eta_m^{(P)}$ nucleus locates right at the centre of the prism, whereas the $\eta_{n,u}^{(D)}$ ($u=x,y,z$) and $\eta_{g,xy}^{(Q)}$ nuclei appear confined around the base of the prism. Thus, the whole set of nuclei in figure 2.4a is interpreted as the simplest combination of pole, dipole and quadrupole source elements with maximum occurrence probability, out of the group of all equivalent, more complex multipole source combinations providing the same apparent resistivity dataset within V.

In order to see whether there is a way to highlight the 3D geometry of the source body, row b in figure 2.4b shows the $\eta_m^{(P)}$, $\eta_{n,u}^{(D)}$ ($u=x,y,z$) and $\eta_{g,xy}^{(Q)}$ isosurfaces relative to a percentage of the primary MAV as listed in table 2.2 appendix b. Except for the $\eta_m^{(P)}$ nucleus, for which the same reduction as before has been used, all other reductions have been set at 50%, so chosen as to fit to the following criterion. By gradually decreasing the percentage at steps of 5% from 95%, we have observed the growth of a bump in the isosurfaces, peaking up to a maximum and then gradually flattening, till vanishing. We have assumed the percent value corresponding to the observed maximum bump peaking.
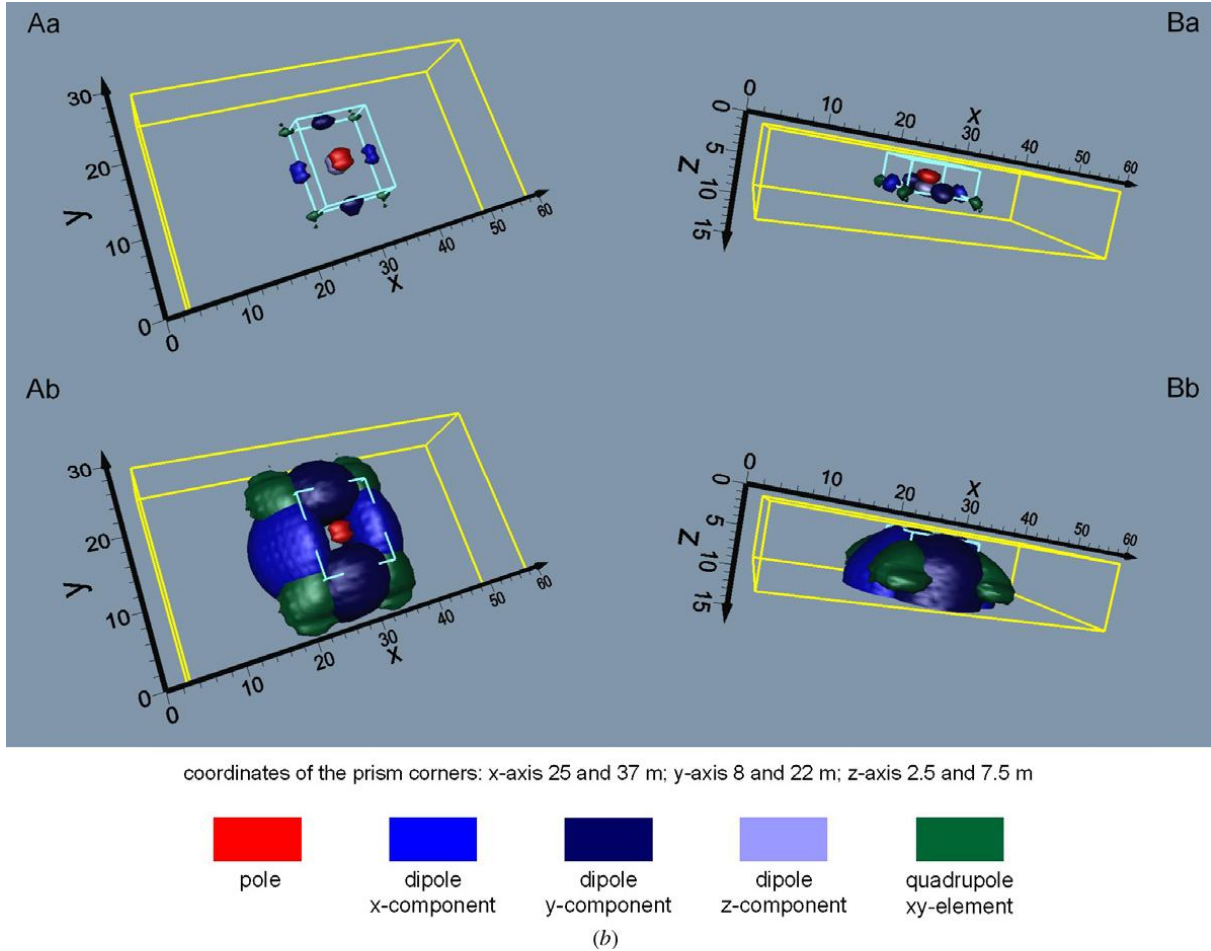
coordinates of the prism corners: x-axis 25 and 37 m; y-axis 8 and 22 m; z-axis 2.5 and 7.5 m

| pole | dipole x-component | dipole y-component | dipole z-component | quadrupole xy-element |

(b)

Figure 2.4 (b) (Continued.)

This approach is nothing but a quick inspection of the presence of secondary MAV. The picture thus obtained is compared with the previous one drawn in row c of figure 2.4a, and replicated in row a of figure 2.4b. The peaking bumps are all directed topwards, with those of $\eta_{n,u}^{(D)}$ ($u=x,y$) spreading against the lateral faces, and those of climbing $\eta_{g,xy}^{(Q)}$ along the vertical edges of the prism.

As a second example, we consider the situation where the same prism with a resistivity of 5000 Ω m as before emerges from a substratum with the same resistivity into a top layer of 500 Ω m. Figure 2.5 shows the results of the new simulation. In detail, row a shows the $\eta_m^{(P)}$, $\eta_{n,u}^{(D)}$ ($u=x,y$) and $\eta_{g,xy}^{(Q)}$ nuclei bounded by isosurfaces relative to 95% of the corresponding primary MAV (see table 2.2 appendix b).
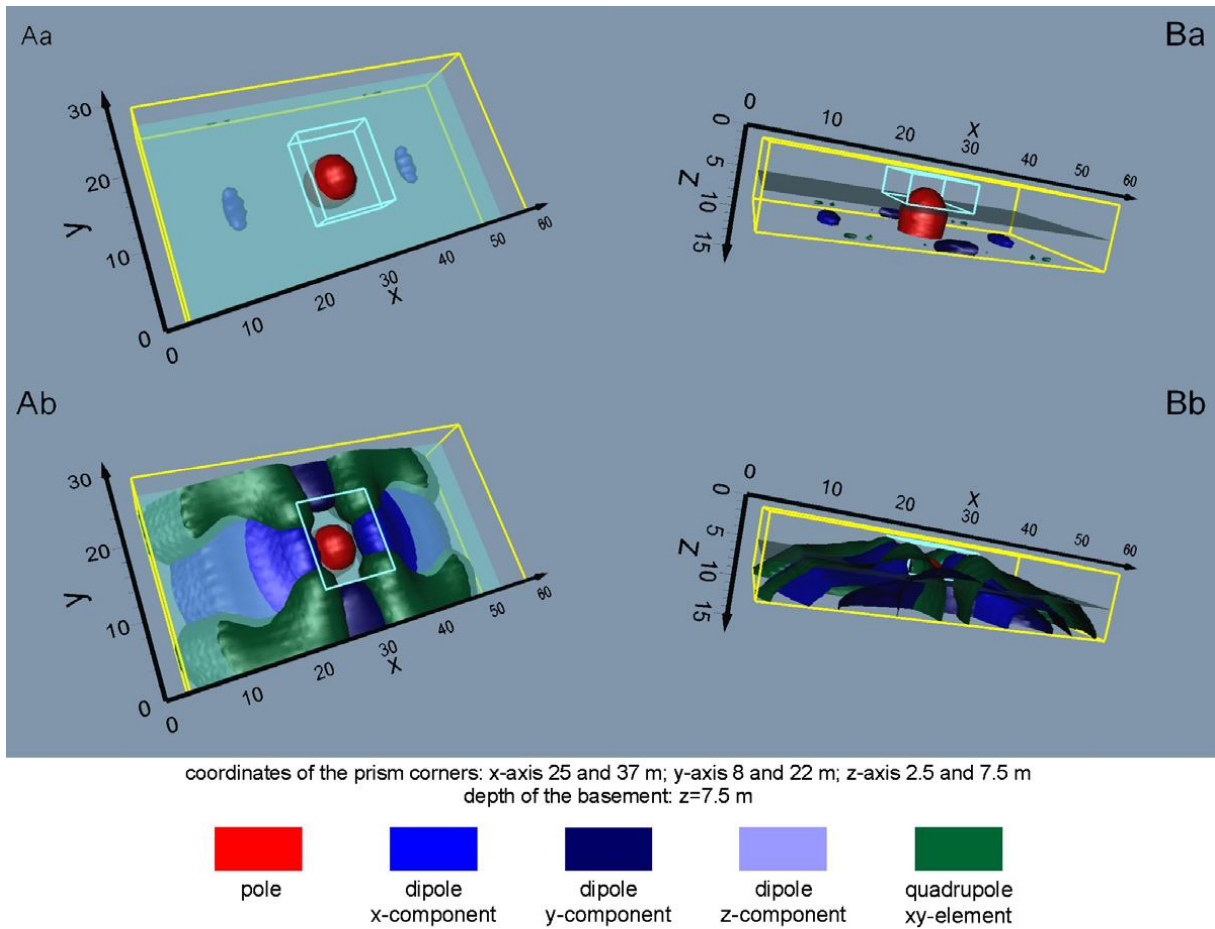
coordinates of the prism corners: x-axis 25 and 37 m; y-axis 8 and 22 m; z-axis 2.5 and 7.5 m
depth of the basement: z=7.5 m

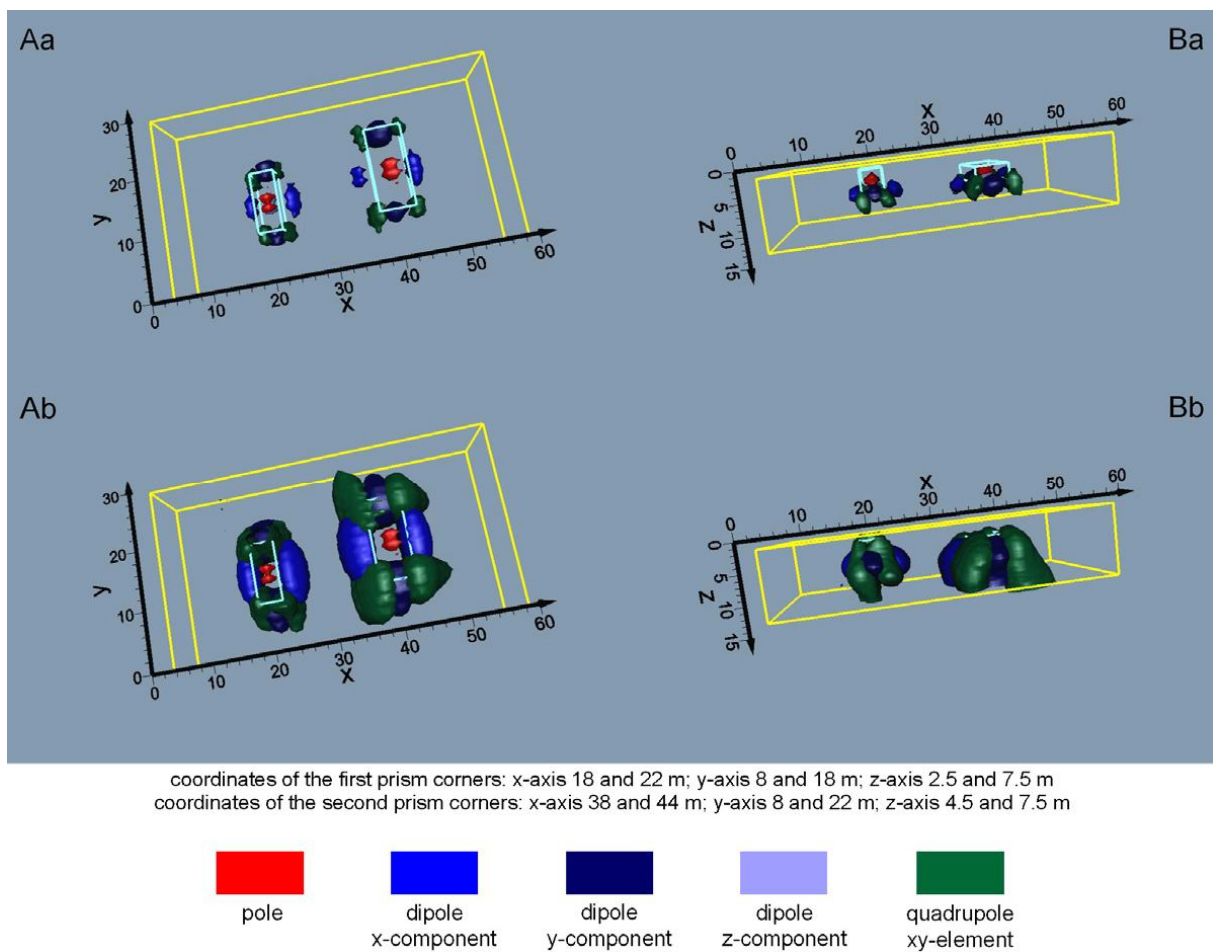| pole | dipole x-component | dipole y-component | dipole z-component | quadrupole xy-element |

Figure 2.5 The SPOP, SDOP and SQOP 3D GPT for a rectangular prism of 5000 Ω m (bordered by light blue lines) and spatial location as in legend, immersed in a two-layer host medium with an overburden of 500 Ω m and substratum of 5000 Ω m. The prism with yellow borders is the datum domain. Scale of axes is in m. For the isosurfaces bounding the coloured small (row a) and big (row b) nuclei, containing the SPOP, SDOP and SQOP MAV, see table 2.2 appendix b.

Compared with the previous case, we do not recognize now any relation of the nuclei with characteristic points of the prism, due to the presence of the high-resistivity basement. Once again, we must retain that this set of primary MAV nuclei represents the simplest array of source elements with maximum occurrence probability, within the class of equivalent arrangements. Row b shows the $\eta_m^{(P)}$, $\eta_{n,u}^{(D)}$ ($u=x,y$) and $\eta_{g,xy}^{(Q)}$ isosurfaces relative to the percentages of the primary MAV listed in table 2.2 Appendix B, obtained by the maximum bump peaking criterion previously illustrated.

Row b shows a clear smooth version of the prism-basement geometry, rather distorted at the margins due to the finite extent of V. The influence of the finite extent of the data volume is a topic poorly investigated in most modelling and inversion

approaches. We continue our simulation analysis by proposing a more complex target structure, made of two separated prisms, with different sizes and collocation, without and with basement. The results are depicted in figures 2.6 and 2.7 for the two-prism structure in a homogeneous half-space and in a two-layer host medium, respectively. For both simulations, the same comments as in the previous corresponding cases can be made, except for the evident loss of symmetry of the isosurfaces, due to the different size and collocation of the two prisms.

coordinates of the first prism corners: x-axis 18 and 22 m; y-axis 8 and 18 m; z-axis 2.5 and 7.5 m
coordinates of the second prism corners: x-axis 38 and 44 m; y-axis 8 and 22 m; z-axis 4.5 and 7.5 m

pole   dipole x-component   dipole y-component   dipole z-component   quadrupole xy-element

Figure 2.6 The SPOP, SDOP and SQOP 3D GPT for a two-prism model of 5000 Ω m (bordered by light blue lines) and spatial location as in legend, immersed in a homogenous half space of 500 Ω m. The larger prism with yellow borders is the 3D datum domain. Scales are in m. For the isosurfaces bounding the coloured small (row a) and big (row b) nuclei, containing the SPOP, SDOP and MAV, see table 2.2 appendix b.
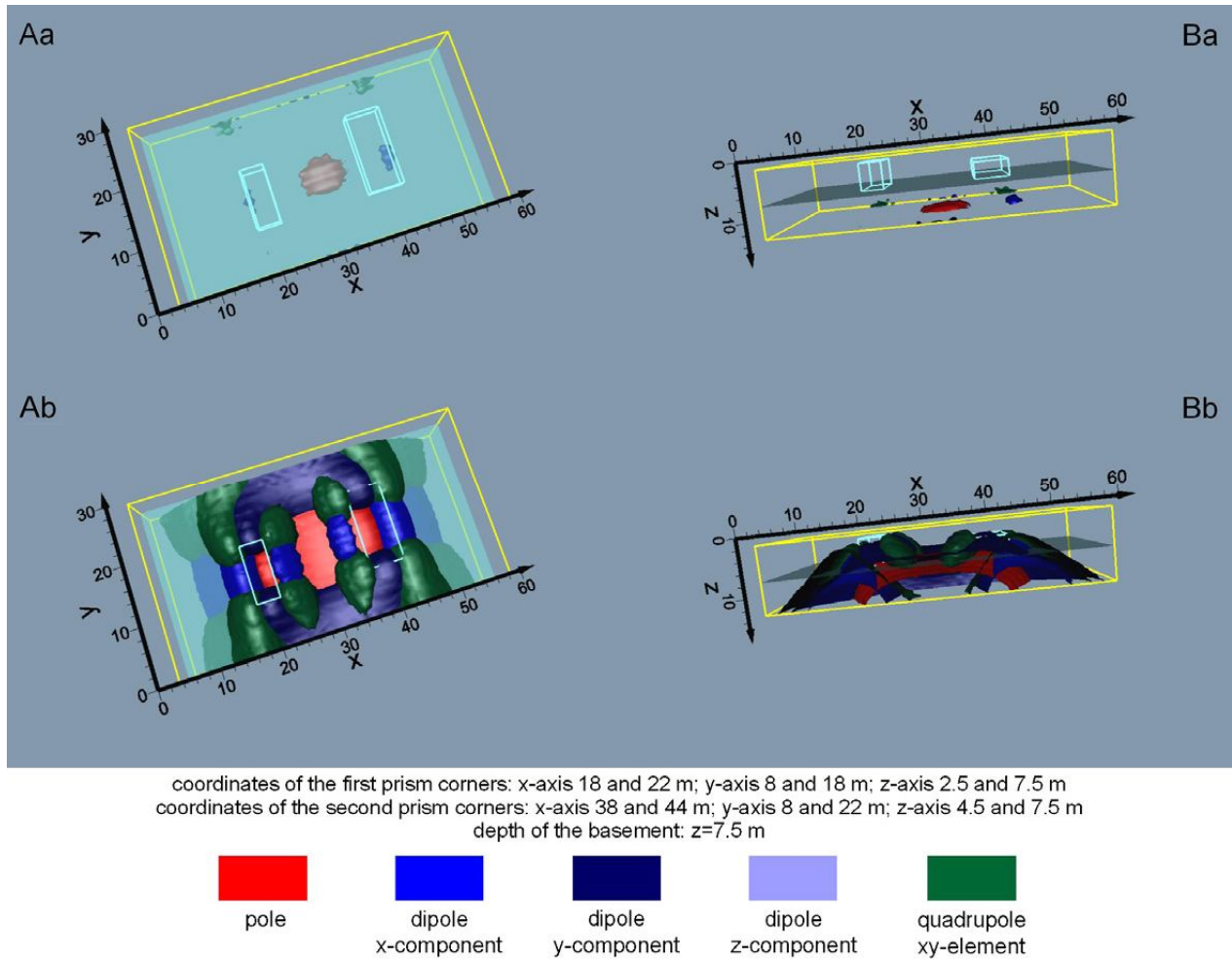
coordinates of the first prism corners: x-axis 18 and 22 m; y-axis 8 and 18 m; z-axis 2.5 and 7.5 m
coordinates of the second prism corners: x-axis 38 and 44 m; y-axis 8 and 22 m; z-axis 4.5 and 7.5 m
depth of the basement: z=7.5 m

pole   dipole x-component   dipole y-component   dipole z-component   quadrupole xy-element

Figure 2.7 The SPOP, SDOP and SQOP 3D GPT for a two-prism model of 5000 Ω m (bordered by light blue lines) and spatial location as in legend, immersed in a two-layer host medium with overburden of 500 Ω m and substratum of 5000 Ω m. The larger prism bordered by yellow lines is the 3D datum domain. The scale of the three coordinate axes is in m. For the isosurfaces bounding the coloured small (row a) and big (row b) nuclei, containing the SPOP, SDOP and SQOP MAV, see table 2.2 appendix b.

2.4   A field example at Pompei

.

We show the results obtained from the application of an advanced geoelectrical tomography survey performed in an unexplored site of the archaeological park of Pompei, aiming at identifying anomalies ascribable to remains of walls and roads, according to the expectation of the local archaeological authority.

The Roman town of Pompei, located 30 km SE of Naples, developed on a flat topographical surface gently degrading towards the Gulf of Naples, created by the

Vesuvius activity, which had prior deposited in this sector an alternating sequence of fall and flow pyroclastic products. Then, the 79 AD Vesuvius eruption completely destroyed the Roman town, covering it with even more than 10 m of pyroclastic fall products. Nowadays, only a little amount of the vestiges of the ancient Pompeian civilization has been brought to light.

The study area is located in the *Regio* III sector of the archaeological park (figure 2.8), on a locally flat topographic high created by the 79 AD pyroclastic deposits (figure 2.9a), placed at no more than 6 m above the original ground level of the ancient town, judging from the adjacent visible ruins (figure 2.9b).
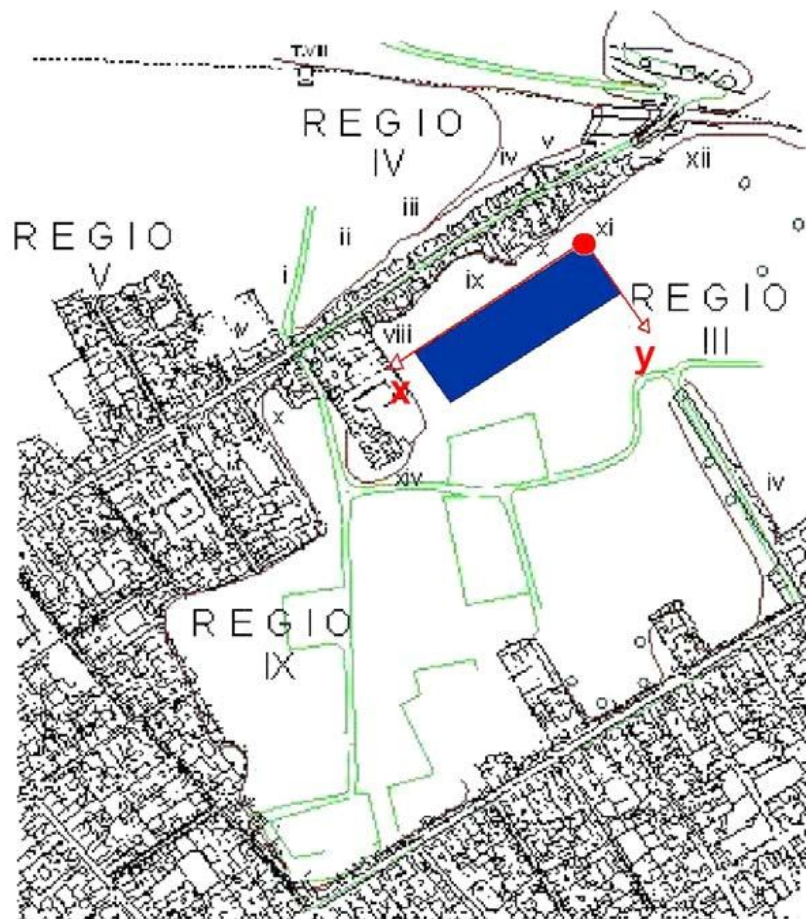
Figure 2.8 Plan view of a portion of the Pompei archaeological park. The rectangle in the *Regio* III sector is the area surveyed by the geoelectrical method. The top right corner of the rectangle is assumed to be the origin of the local reference coordinate system.

Figure 2.9 (*a*) The rectangular geoelectrical survey area in the *Regio* III sector of the Pompei archaeological park. The far-field left corner corresponds to the top right corner of the rectangle sketched in figure 2.8 and is assumed to be the origin of the local reference coordinate system. (*b*) Pompeian exposed ruins adjacent to the top longer side of the rectangle sketched in figure 2.8.

2.4.1 Geoelectrical data acquisition, processing and pseudoimaging

Figure 2.9a shows the rectangular area of 2820 m^2 (94 m × 30 m), where 16 parallel profiles of 94 m of length equispaced by 2 m were programmed. The longer side of the rectangle was oriented N60°E, normal to the main axis of the nearby excavated Roman *insulae* (figure 2.8). This axis was thus assumed as the strike of a prevailing 2D resistivity structure expected under the chosen rectangle. For this reason, the dipole-dipole (DD) electrode array, notoriously most sensitive to lateral resistivity contrasts [34], was run along each line according to the well known pseudosection data acquisition technique.

A programmable resistivity-meter was used, which allowed up to 23 simultaneous voltage measurements for every current injection, by setting the maximum standard deviation at 3% and selecting the number of stacking cycles between 3 and 10 for random noise attenuation. The spreads of the emitting and receiving dipoles and the advancing step along the profiles were fixed at 2 m. The distance between the centres of the dipoles was expanded from an initial spacing of 4 m up to 28 m, thus reaching the maximum pseudodepth of 14 m starting from 2 m and going down by 1 m every 2 m of

spacing increase. 507 DD apparent resistivity determinations were thus realized along each profile for a total of 8112 data collected inside the whole rectangle.

Figure 2.10 resumes the DD data acquisition procedure. As said, it consists of a sequence of parallel profiles on a flat ground surface, identified by the index $j=1,2,..,16$, as in figure 2.10a. The generic jth profile is then considered in detail in figure 2.10b, where the emitting (AB) and receiving (MN) dipoles are identified by the indices $i=1,2,..,45$ and $k=1,2,..,13$, and the depth of attribution of the apparent resistivity value (pseudodepth) by the index $k=1,2,..,13$. Hence, each apparent resistivity value is a function of the three indices, say $\rho_a(i,j,k)$.
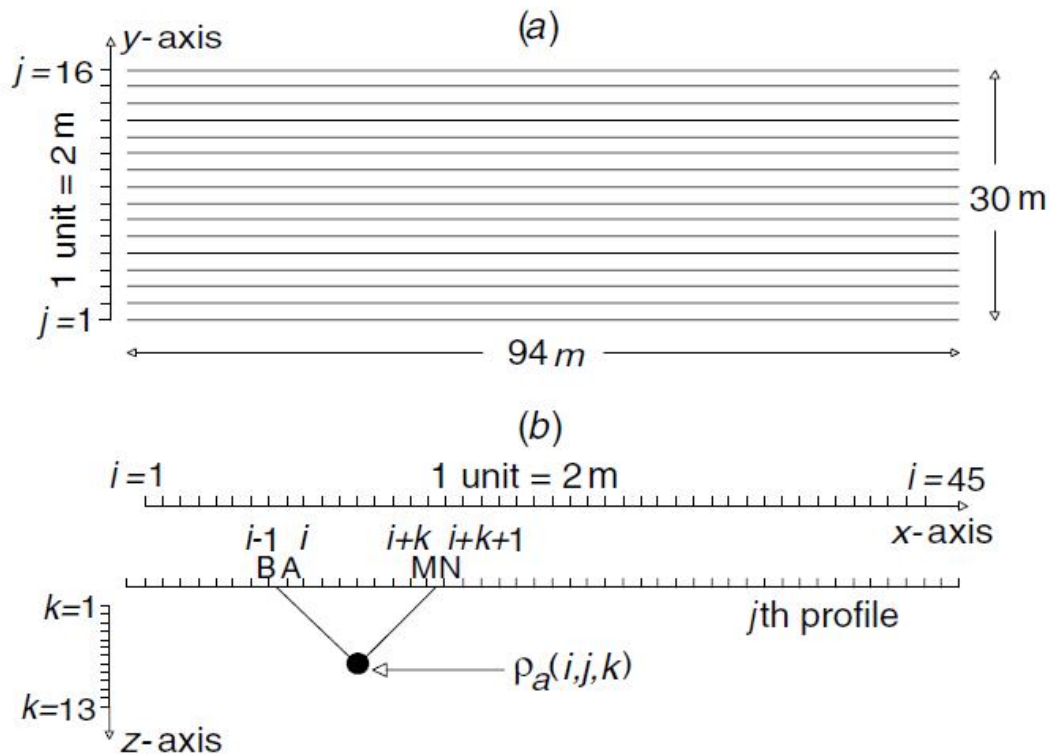
Figure 2.10 The dipole–dipole (DD) geoelectrical procedure in the rectangular survey area of figure 2.8 . (*a*) Plan view of the regular DD profile distribution in the area; (*b*) the pseudodepth data attribution technique along a DD profile.

Figure 2.11a displays a sequence of horizontal slices, in each of which the common logarithm of the DD apparent resistivities at the same pseudodepth are contoured. The slices were drawn using the whole dataset of the 16 parallel profiles. This slice sequence gives a quick view of the degree of inhomogeneity in the subsoil, which in the

pseudodepth range from 2 m down to about 8 m seems to dominate along the *x*-axis, i.e. the direction of the long side of the survey rectangle (figure 2.8). In the following pseudodepth range from 9 m down to 14 m, the DD apparent resistivity pattern radically changes showing the tendency to homogenize towards low apparent resistivity values, except for two evident anomalous highs, of which the biggest one dominates in the whole central area and the other one is confined in the top marginal area in the left-hand sector of the slices.
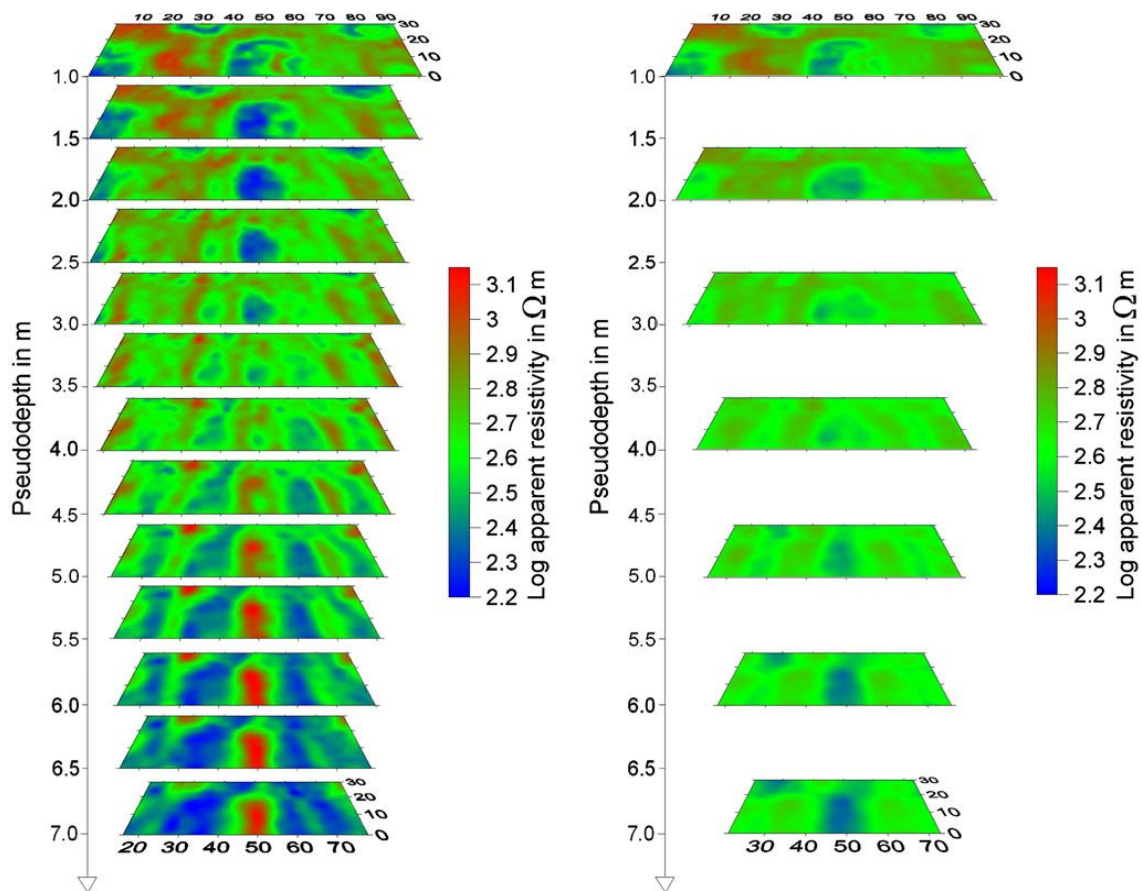
Figure 2.11 The DD (*a*) and Wenner (*b*) pseudoslice imaging of the apparent resistivity values collected in the rectangular survey area of figure 2.8.

The DD apparent resistivity pattern in the near-surface pseudodepth range can qualitatively be interpreted as the geoelectric signature of archaeological remains, in accordance with the initial hypothesis of anomalies expected to conform to a probable S30°E continuation of the wall-and-road mesh appearing aside in the partially excavated *insulae* viii-ix-x (figure 2.8 and figure 2.9b). The DD pattern in the deeper pseudodepth

range seems, instead, to represent the relatively less resistive nature of the local substratum. It appears to expand under the whole survey area, except for the mentioned positive nuclei, which are suspected to be ghost anomalies, typical of the dipole-dipole array, due to the diagonal downward dragging effect of shallow resistive anomalies, also known as the inverted V-shaped effect.

To better visualize this effect, figure 2.12 shows the pseudosections relative to two profiles selected in correspondence with the top marginal and the bigger central positive anomaly, respectively. These anomalies here appear as the result of a focalization of two nearby inverted V-shaped dragging effects, right where the inner tails intersect. Nonetheless, to take a final decision, we carried out in the whole area a further geoelectric survey, using the Wenner array, which is not influenced by dragging effects. An approach similar to the DD technique was used, consisting in expanding the Wenner spacing, equal to one third of the distance between the external A and B current electrodes, by multiples of 2 m, starting from 2 m up to 14 m. The Wenner apparent resistivity values conventionally are attributed along the vertical axis through the centre of the array at a pseudodepth set equal to the array spacing.
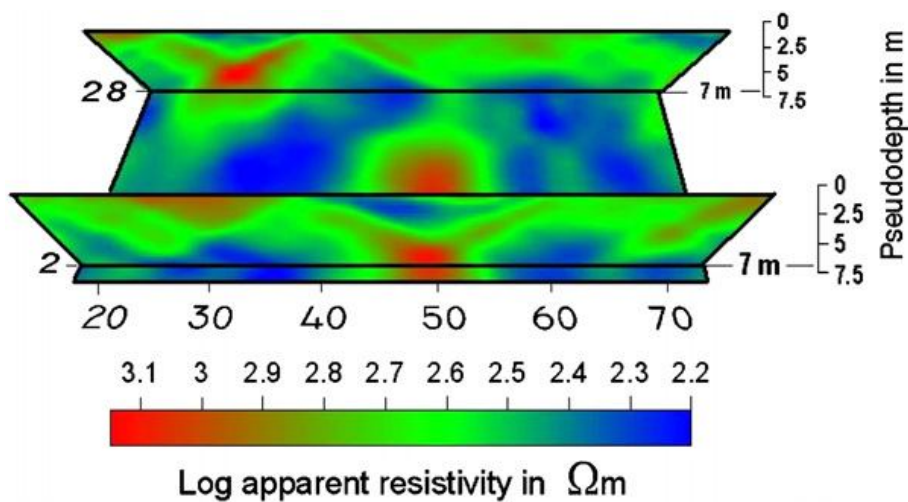

Figure 2.12 DD pseudosections across the profiles at $y = 2$m ($j= 2$)and $y = 28$m ($j= 15$) cutting the pseudoslice at the pseudodepth of 7 m ($k = 13$).

Figure 2.11b displays the sequence of horizontal slices so obtained, in each of which the common logarithm of the Wenner apparent resistivities at the same pseudodepth are contoured. No positive anomaly appears in the critical zones, at pseudodepths

comparable with those in figure 2.11a. Hence, we conclude that the deep DD positive nuclei in figure 2.11a are likely to be considered ghost anomalies.

It is finally worth noticing the less pronounced selectivity power of the Wenner array with respect to the DD array. The shallow anomalies of potential archaeological interest appear in figure 2.11b less articulated and more rapidly vanishing versus depth than the corresponding anomalies in figure 2.11a. This is the reason why we have definitely focused our attention only on the DD survey.

A DD apparent resistivity imaging like that in figure 2.11a has, however, only a rough relationship with the true resistivity structure, whose localization is the ultimate scope of this survey. In fact, shape and amplitude of the anomalies in figure 2.11a strictly represent the shift among different DD apparent resistivity values, each depending not only on the true resistivity distribution, but also on the array stepping used to sense the subsoil. In order to remove this last effect and get a more realistic imaging of the buried structures from the apparent resistivity dataset, we have applied the 3D probability tomography method [26] of which we give in the following section an extension according to the 3D DD data acquisition technique used in this survey. Probability tomography was originally proposed for the self-potential method [41,42], and very recently applied also to the magnetic method [30].

2.4.2 Result of the 3D probability tomography

Figure 2.13 shows the 3D geoelectric source pole tomography, represented as a sequence of slices at increasing depth from 2 m bgl down to 6.5 m bgl.
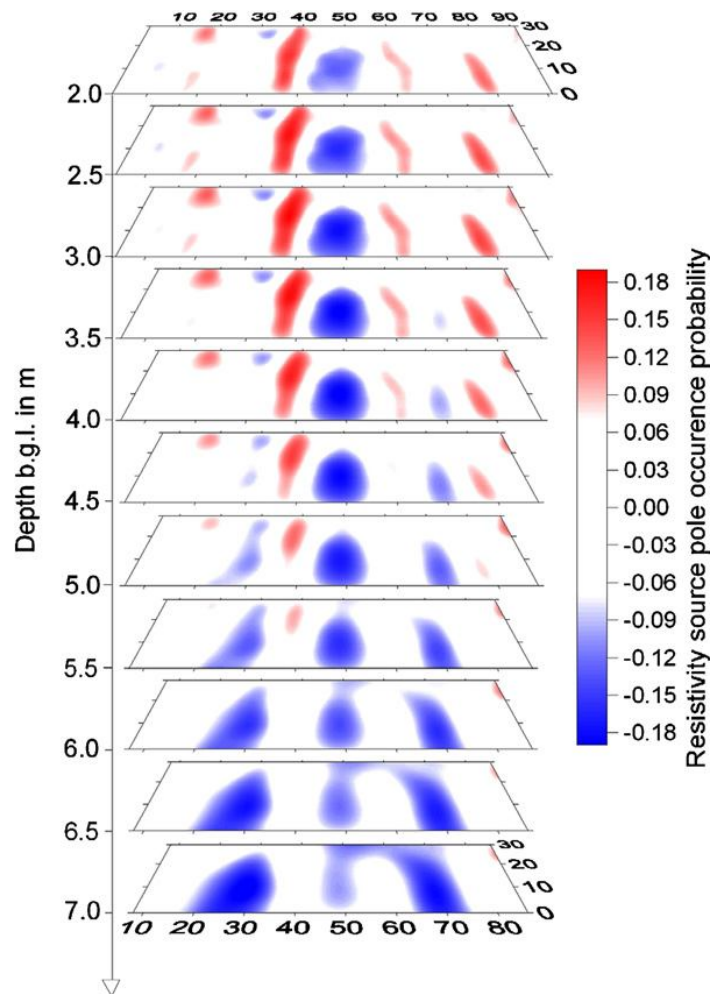
Figure 2.13 The near-surface 3D source pole tomography of the DD apparent resistivity values collected in the rectangular survey area of figure 2.8.

We have deliberately chosen this depth interval, because, as previously outlined, it is likely to represent the buried environment thickness of archaeological interest. In fact, all SPOP nuclei potentially associable to archaeological bodies appear in this range. Firstly, we notice the presence of positive nuclei, mostly aligned along the *y*-axis, representing the zones where higher is the probability to find true resistivities exceeding the reference value, which was taken equal to the mean apparent resistivity of 432.5 Ωm, whose common logarithm is 2.64. The maximum SPOP value of each of these positive nuclei is met at a depth around 3.5 m bgl, which is assumed as the depth of the centre of mass of the more resistive bodies. From the archaeological point of view, these masses can be associated with remains of walls and/or heaps of collapsed stone blocks.

Another clear signal is the central large negative nucleus, which of course identifies a zone where the probabilities to find true resistivities lower than the reference value are higher. The maximum absolute value within this negative nucleus is found again at a depth around 3.5 m bgl. From the archaeological point of view, we can now associate this less resistive volume to accumulation of wet volcanic products filling an originally open air space, very likely a *peristilio*, i.e. a home court with columned portico. Less intense are two other negative nuclei, one visible since the shallowest slice, around the point $x=32$ m and $y=28$ m, and the other starting from the slice at 2.5 m of depth, around the point $x=70$ m and $y=8$ m. As the previous negative nucleus, also the two smaller cores may be ascribed to accumulations of wet volcanic products filling again originally open spaces, very likely associable now to the presence of roads, as the cores seem to assume a narrow elongated shape from 4.5 m of depth down to 5.5-6 m. They finally tend to be fully absorbed inside deeper and much larger negative nuclei, visible in the far-surface tomography depicted in figure 2.12, very likely representing the virgin volcanic top soil existing before the 79 AD eruption.
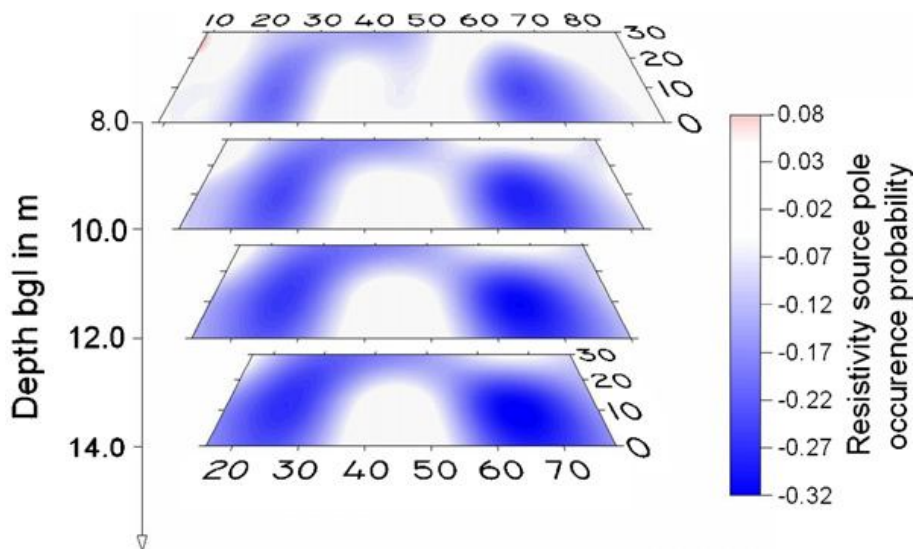

Figure 2.14 The far-surface 3D source pole tomography of the DD apparent resistivity values collected in the rectangular survey area of figure 2.8.

To enhance the previous archaeological tentative interpretation of the anomalies emerged from the 3D tomographic analysis, we show in figure 2.15 how the SPOP nuclei spread over the most significant slice at 3.5 m of depth correlate with the traces of the remains so far explored within the *insulae* viii, ix and x inside the *Regio* III sector of the park.

It is worthwhile to observe how the 3D probability tomography method behaves in presence of ghost anomalies, like *e.g.* the deep positive anomaly appearing in the central part of the deep pseudoslices in figure 2.11a. This ghost effect has almost completely dropped out as no positive nucleus appears in the same region across the bottom depth range in figure 2.8. This is a further evidence of the filtering power of the probability tomography method, already tested in previous applications [26,27].
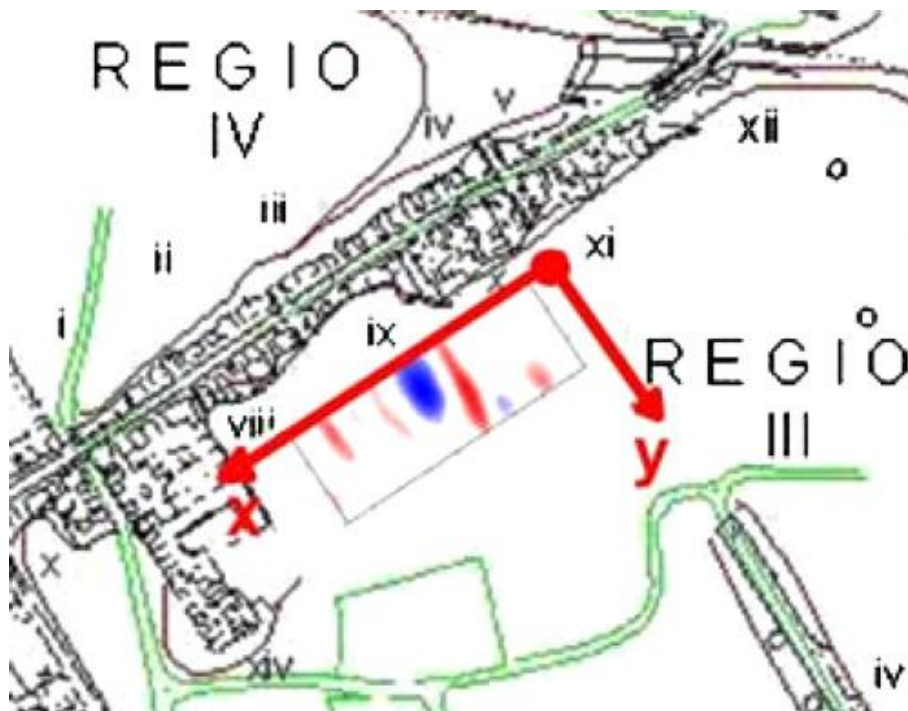

Figure 2.15 The investigated area in the archaeological park of Pompei with the SPOP tomographic slice at a depth of 3.5 m.

Figure 2.16 shows the 3D source dipole tomography, given as a sequence of slices from 2 m down to 6.5 m bgl. Owing to the vector character of the dipole, the 3D SDOP analysis is performed for each scalar dipole component along its relative reference axis.
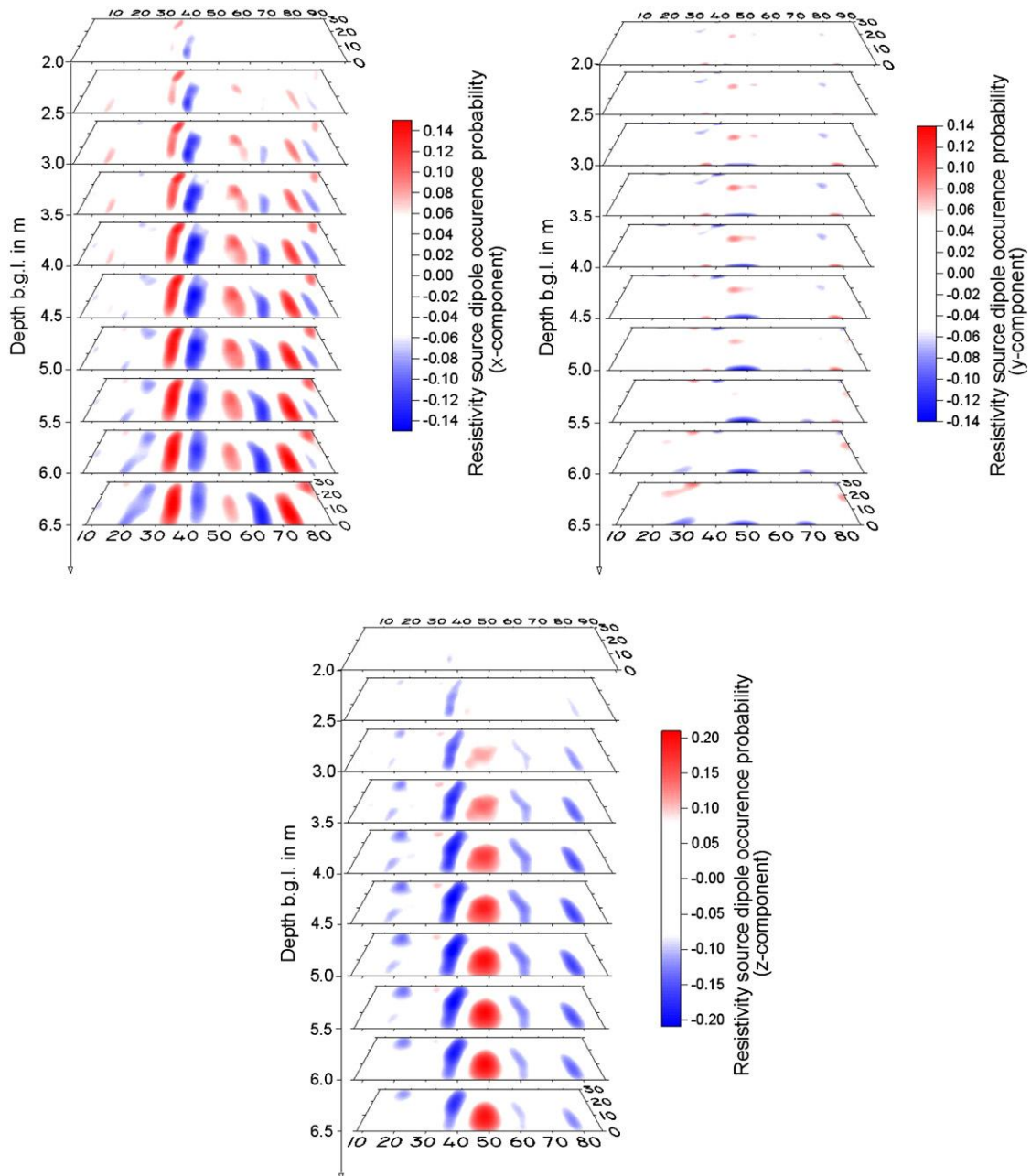

Figure 2.16 The 3D source dipole tomography of the DD apparent resistivity values collected in the survey area of figure 2.8. Tomography of the *x*-component (*a*), the *y*-component (*b*) and the *z*-component (*c*) of the dipole sources.

We recall that the presence of a SDOP nucleus along a given axis marks the passage from one to another different resistivity along that direction, thus providing an indication about the position of a resistivity boundary. Since in the present application the expected geometry of the concealed targets should nearly conform to right prismatic bodies with corners parallel to the *x,y,z* axes, the presence of a pair of adjacent SDOP nuclei with opposite sign occurring along one axis can be a useful indicator of the body size along that axis. Moreover, as it regards the sign of a SDOP nucleus we recall that, moving along the positive direction of a system axis, a positive sign of the relative dipole component marks the transition from a lower to a higher resistivity value across the boundary that the nucleus highlights, and the reverse for a negative sign.

Figure 2.16a refers to the *x*-component of the dipole sources. The sequence of pairs of opposite sign SDOP nuclei, elongated along the *y*-axis, is a clear evidence of where the transition from the resistive blocks to the conductive filled spaces and vice versa are most likely located along the *x*-axis. A similar conclusion can be reached along the *y*-axis looking at figure 2.16b, which shows the SDOP analysis of the *y*-component of the dipole sources, now characterized by less intense, but more concentrated nuclei. At last, figure 2.16c refers to the *z*-component of the dipole sources. This last representation is quite similar to the SPOP tomographic sequence in figure 2.16 as far as the shallow nuclei of archaeological concern are considered. The only difference, apart from the expected sign inversion, is that the nuclei of both signs are all shifted downwards, and their maximum absolute values are met around 5-6 m of depth bgl, *i.e.* approximately at the depth of the ancient ground level, amply visible north of the surveyed area (figure 2.9b).

Figure 2.17 shows the SPOP, SDOP and SQOP 3D tomographies obtained at Pompei, where, in order to put in evidence a source geometry as close as possible to the expected targets, only the $\eta_m^{(P)}$, $\eta_{n,u}^{(D)}$ (*u=x,y,z*) and $\eta_{g,xy}^{(Q)}$ isosurfaces relative to a percentage of the primary MAV as listed in table 2.3 appendix b have been plotted.
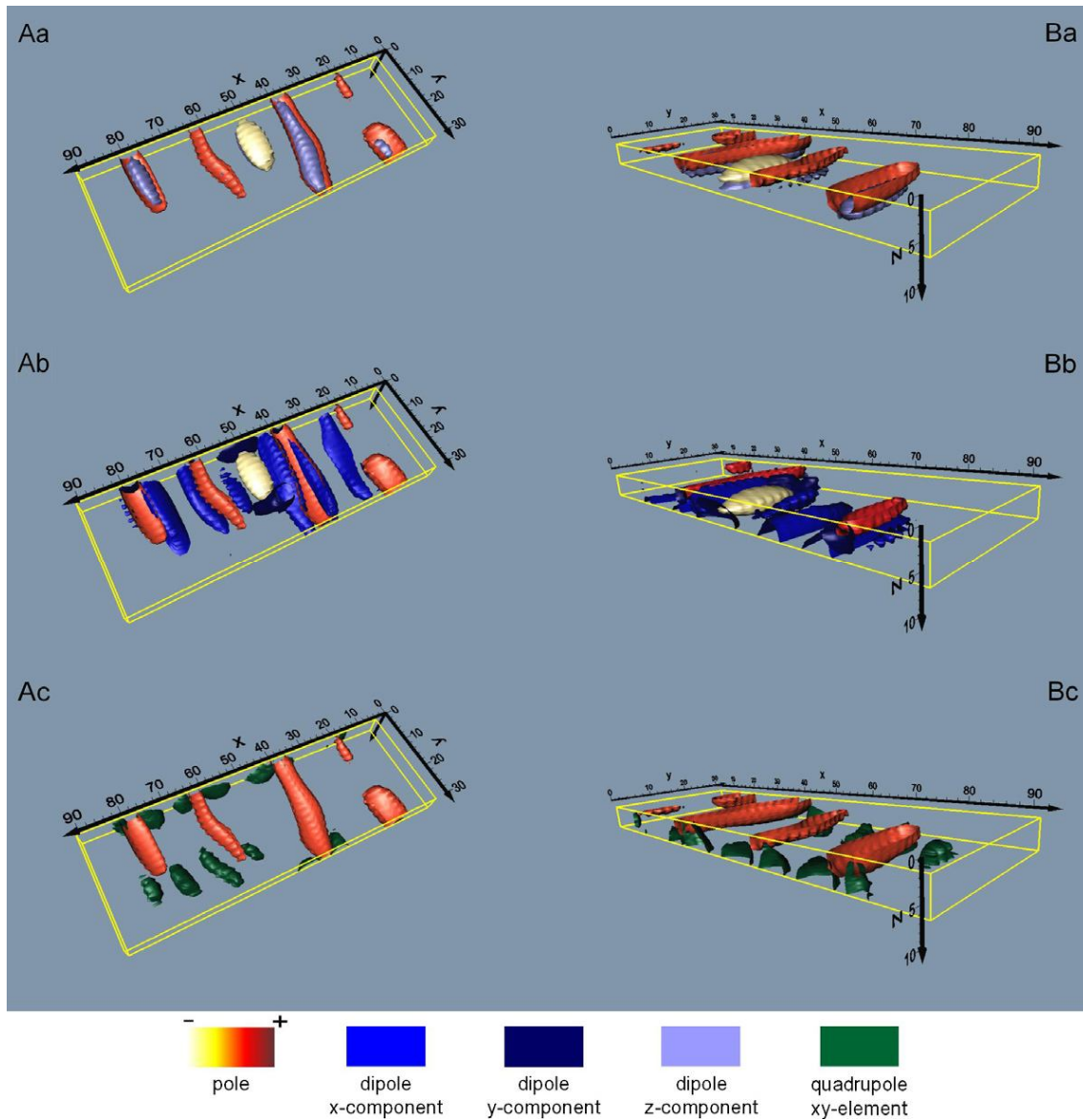
Figure 2.17 The SPOP, SDOP and SQOP 3D GPT of the geoelectrical survey in the archaeological park of Pompei (Naples, Italy). The prism bordered by yellow lines is the 3D datum domain. The scale of the three coordinate axes is in m. For the isosurfaces bounding the coloured nuclei, containing the SPOP, SDOP and SQOP MAV, see table 2.3 appendix b.

The pictures in figure 2.17 are now arranged in a different way as follows. Row a shows the combination of the $\eta_m^{(P)}$ and $\eta_{n,z}^{(D)}$ tomographies, where, for the importance that the sign has during interpretation, a distinction has been made between negative and positive SPOP nuclei using different colours.

Row b shows together $\eta_m^{(P)}$, $\eta_{n,u}^{(D)}$ ($u=x,y$) tomographies. From the archaeological point of view, the sequence of pairs of SDOP nuclei, elongated along the x- and y-axes,

may be taken as evidence of the existence of planar lateral bounds to the SPOP anomalies previously discussed, i.e., where the transition from the resistive blocks to the conductive filled spaces and vice versa are most likely located [1,2].

Finally, row c shows the new experimental result derived from the theory exposed, i.e. the $\eta_{g,xy}^{(Q)}$ tomography, combined with the $\eta_{m}^{(P)}$ tomography.

The SQOP nuclei clearly appearing at the corners of the positive SPOP nuclei would likely indicate the presence of vertical edges at the borders of the resistive structures delineated by the SPOP and SDOP analysis. For the marginal SQOP nuclei along the x-axis, the distortion due to the lateral wall of the data volume is also well evident. In conclusion, the prismatic shape of these structures, thus emerged from the combined SPOP, SDOP and SQOP analysis, is likely to be interpreted as belonging to elongated remnants of walls, rather than chaotic heaps of collapsed stones.

3. Multipole Gravity Tomography

3.1 The basic gravity theory

Gravity is defined as the force of mutual attraction between two bodies, which is a function of their masses and the distance between them, and is described by Newton's law of universal gravitation. An effect of gravity is observed when the fruit from a tree falls to the ground. The gravity field at each location on Earth consists of a global field which is superimposed by a local anomaly field. In a gravity survey, measurements are made of the local gravity field differences due to density variations in the subsurface. The effects of small scale masses are very small compared with the effects of the global part of the Earth's gravity field (often on the order of 1 part in 10^6 to 10^7).
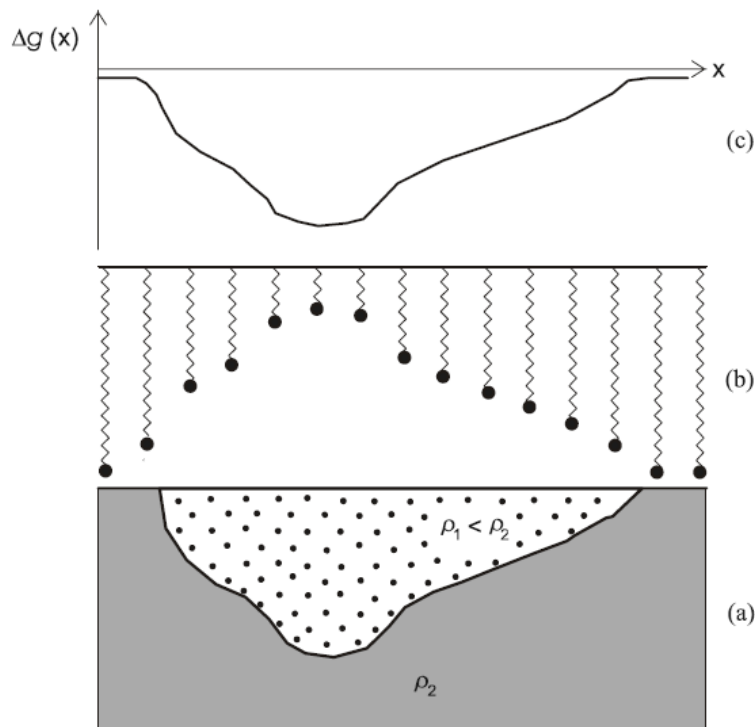

Figure 3.1 Principle of a gravity measurement: (a) the model shows a geological structure with a density ρ_1 embedded in material with a higher density ρ_2, (b) the spring with a small mass at the end of it changes length with changes in the gravity field, (c) the measurement results are plotted to document the gravity anomaly $\Delta g(x)$

Highly sensitive gravimeters are necessary for measuring such variations in gravitational attraction accurately. Special data processing and interpretation techniques are used to interpret the shape and amplitude of the anomalies in terms of subsurface geological or anthropogenic structures. Gravity measurements can be performed on land, at sea, and in the air. For environmental problems, land measurements are generally made. A necessary condition for the application of this method is the existence of density contrasts. The schematic in figure 3.1 shows structure with a density ρ_1 embedded in material with a higher density ρ_2. Considering a gravimeter as basically a mass on a spring, the amplitude of the gravity anomaly is a function of the expansion or contraction of the spring, the geological situation in figure 3.1 will cause the length of the spring to decrease above the anomalous structure. The fundamental physical law used in gravity surveys is the universal gravitation.

Each point *P* (identified by the position vector **r**) ,on, above and below the Earth's surface is affected by the gravitational (or gravity) field **g**(**r**). This is a natural potential field like, for example, the magnetic field. The gravity field is measured in units of acceleration [m s^{-2}]. This field is mainly caused by the attraction between masses of the Earth and an arbitrary mass at point *P* with the position vector **r**. The gravitational force *F* between two point masses *m* and *m'* with the distance $\vec{r}$ between them is:

$$\mathbf{F}(\mathbf{r}) = G\frac{mm'}{r^3}\mathbf{r} \tag{3.1}$$

where the gravitational constant G = $6.672 \cdot 10^{-11}$ (m^3 kg^{-1} s^{-2}). The effect of the gravitational field *g* of *m* on *m'* is derived from equation (3.1):

$$\mathbf{g}_E(\mathbf{r}) = G\frac{m}{r^3}\mathbf{r} \tag{3.2}$$

This effect is called gravitational acceleration. The mass *m* of a body is given by the product of its density ρ and volume *V*. In addition to the gravitational acceleration of the Earth $\mathbf{g}_E(\mathbf{r})$ point *P* is affected by centrifugal acceleration $\mathbf{g}_C(\mathbf{r})$ and by the gravitational attractions of mainly the moon and the sun $\mathbf{g}_T(\mathbf{r})$ the variations of which

are called tides. These tides vary with respect to place and time. The centrifugal acceleration $\mathbf{g}_C(\mathbf{r})$ is due to the rotation of the Earth and depends on the latitude φ of the point *P*. The gravitational field at point *P* is

$$\mathbf{g}(\mathbf{r}) = \mathbf{g}_E(\mathbf{r}) + \mathbf{g}_C(\mathbf{r}) + \mathbf{g}_T(\mathbf{r}) \tag{3.3}$$

This formula describes the global gravity field. The gravimeters measure the vertical component of acceleration due to gravity.

The anomalous gravity field Δg_z caused by density inhomogeneities of geological or anthropogenic structures is superimposed on the global field. Equation (3.2) can be used to calculate Δg_z if the mass *m* is replaced by the anomalous mass $\Delta m = \Delta\rho(\mathbf{r_q}) V_1$, where $\Delta\rho(\mathbf{r_q})$ is the density contrast between the inhomogeneity and the surrounding material, V_1 is the volume of the inhomogeneity.

Consequently, the gravity value $g_z(\mathbf{r})$ at point *P* is calculated from the theoretical gravity field value γ_z^{th}, the tidal effect and the anomalous field

$$g_z(\mathbf{r}) = \gamma_z^{th}(\mathbf{r}) + g_z^T(\mathbf{r}) + \Delta g_z(\mathbf{r}) \tag{3.4}$$

For geophysical surveys, only gravity anomalies $\Delta g_z(\mathbf{r})$ related to density inhomogeneities in the subsurface are of interest.

The gravity value is influenced by the elevation and the coordinates of the gravity station, the time of the measurement, and the surrounding morphology. Therefore, it is necessary to carry out several corrections. The aim of the corrections is to make the measurement at a single station comparable to the results at the other stations and to remove from the gravity value all known influences that are not due to the investigated structure . The repeated measurements at the reference station in a loop are normally different from the first measurement in the loop. This is due to the effect of tides and instrument drift. These effects have to be eliminated using the internal software of the gravimeter or PC software. When the measurement at the reference station is repeated at least every 45 - 60 minutes, the differences from the first measurement are due to

instrument drift and tidal changes; only when the measurements are repeated can the correction of both effects be carried out in one step. The result of this data processing is the drift and tidal corrected gravity value $\Delta g_z(\mathbf{r})$.

The resulting value due to unknown subsurface structures is called the *Bouguer* anomaly $B_a(\mathbf{r})$ and it is calculated as follows

$$B_a(\mathbf{r}) = \Delta g_z(\mathbf{r}) - \left(\gamma_z^{th}(\mathbf{r'}) + \delta g_{FA} + \delta g_{Boug} + \delta g_{Top} \right) \tag{3.5}$$

with $\gamma_z^{th}(\mathbf{r'})$ is the theoretical gravity field at sea level, δg_{FA} is the free air correction, δg_{Boug} is the Bouguer correction and δg_{Top} is the topographic correction.

Bouguer anomaly is write as follows

$$B_a(\mathbf{r}) = G \int_{V_1} \Delta\rho(\mathbf{r_q}) \frac{z_q - z}{\left| \mathbf{r_q} - \mathbf{r} \right|^3} d\mathbf{r_q} \tag{3.6}$$

and represents the difference between the observed and the theoretical gravity value in the point P, it describes the vertical component of gravity in the point station P due to an anomalous body with a density difference $\Delta\rho$ to the host material.
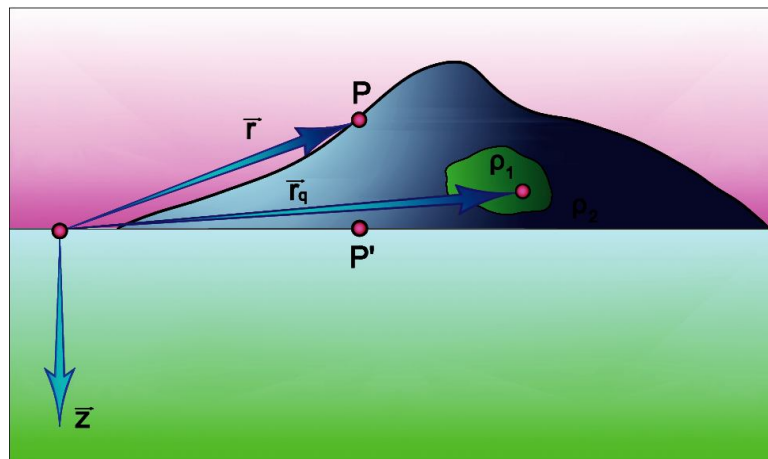

Figure 3.2 Schematic of a non-flat portion of the earth used to derivation of the Bouguer anomaly concept.

3.2 The generalized formalism for gravity

Let us consider a reference system with a horizontal (x,y)-plane and the z-axis positive downwards, and a 2D datum domain S as in figure 1.1. The S-domain is generally a nonflat ground survey area described by a topographic function $z(x,y)$. Indicating with $B_a(\mathbf{r})$ the Bouguer anomaly at a set of datum points $\mathbf{r} \equiv (x,y,z)$, with $\mathbf{r} \in S$, we assume that $B_a(\mathbf{r})$ can be discretised as

$$B_a(\mathbf{r}) = \sum_{m=1}^{M}(\mathbf{p}_m \cdot \mathbf{P}_m)s(\mathbf{r},\mathbf{r}_m) + \sum_{n=1}^{N}(\mathbf{d}_n^u \cdot \mathbf{L}_n^u)s(\mathbf{r},\mathbf{r}_n)$$

$$+ \sum_{g=1}^{G}(\mathbf{q}_g^{uv} \cdot \mathbf{S}_g^{uv})s(\mathbf{r},\mathbf{r}_g) + \sum_{h=1}^{H}(\mathbf{o}_h^{uvw} \cdot \mathbf{C}_h^{uvw})s(\mathbf{r},\mathbf{r}_h) \qquad (3.7)$$

The effect of the M, N, G and H source elements at a point $\mathbf{r} \in S$ is determined by the kernel $s(\mathbf{r},\mathbf{r}_i) = (z_i\text{-}z)/|\mathbf{r}_i\text{-}\mathbf{r}|^3$ $(i=m,n,g,h)$, which represents the vertical component of the gravitational acceleration due to a point mass of unitary strength [28,29].

We define the information power Λ, associated with $B_a(\mathbf{r})$, over the surface S as

$$\Lambda = \int_S B_a^2(\mathbf{r})dS \qquad (3.8)$$

which, using eq. 3.7, is expanded as

$$\Lambda = \sum_{m=1}^{M} p_m \int_S B_a(\mathbf{r})s(\mathbf{r},\mathbf{r}_m)\mathrm{d}S$$

$$+ \sum_{n=1}^{N} \sum_{u=x,y,z} d_n^u \int_S B_a(\mathbf{r})\frac{\partial s(\mathbf{r},\mathbf{r}_n)}{\partial u_n}\mathrm{d}S$$

$$+ \sum_{g=1}^{G} \sum_{u=x,y,z} \sum_{v=x,y,z} q_g^{uv} \int_S B_a(\mathbf{r})\frac{\partial^2 s(\mathbf{r},\mathbf{r}_g)}{\partial u_g \partial v_g}dS$$

$$+ \sum_{h=1}^{H} \sum_{u=x,y,z} \sum_{v=x,y,z} \sum_{w=x,y,z} o_h^{uvw} \int_S B_a(\mathbf{r})\frac{\partial^3 s(\mathbf{r},\mathbf{r}_h)}{\partial u_h \partial v_h \partial w_h}dS \qquad (3.9)$$

Skipping all intermediate steps, we directly arrive at the explicit expressions of the gravity SPOP, SDOP, SQOP and SOOP functions, using the pair of eq.s 1.8 and 1.9, eq.s 1.10 and 1.11, eq.s 1.12 and 1.13, eq.s 1.14 and 1.15

The gravity 3D SPOP function is given as

$$\eta_m^{(p)} = C_m^{(p)} \int\limits_{-X}^{+X} \int\limits_{-Y}^{+Y} B_a(\mathbf{r}) s(\mathbf{r},\mathbf{r}_m) g(z) dx dy \tag{3.10}$$

with

$$C_m^{(p)} = \left[\int\limits_{-X}^{+X} \int\limits_{-Y}^{+Y} B_a^2(\mathbf{r}) g(z) dx dy \cdot \int\limits_{-X}^{+X} \int\limits_{-Y}^{+Y} s^2(\mathbf{r},\mathbf{r}_m) g(z) dx dy \right]^{-1/2} \tag{3.11}$$

The gravity 3D SDOP function is given as

$$\eta_{n,u}^{(d)} = C_{n,u}^{(d)} \int\limits_{-X}^{+X} \int\limits_{-Y}^{+Y} B_a(\mathbf{r}) \frac{\partial s(\mathbf{r},\mathbf{r}_n)}{\partial u_n} g(z) dx dy \,, \; (u{=}x,y,z) \tag{3.12}$$

with

$$C_{n,u}^{(d)} = \left[\int\limits_{-X}^{+X} \int\limits_{-Y}^{+Y} B_a^2(\mathbf{r}) g(z) dx dy \cdot \int\limits_{-X}^{+X} \int\limits_{-Y}^{+Y} \left| \frac{\partial s(\mathbf{r},\mathbf{r}_n)}{\partial u_n} \right|^2 g(z) dx dy \right]^{-1/2} \,, \; (u{=}x,y,z) \tag{3.13}$$

Each first derivative of $s(\mathbf{r},\mathbf{r}_n)$ takes the role of *source dipole scanner*. The first derivatives of $s(\mathbf{r},\mathbf{r}_n)$ are given in expanded form in appendix c.

The gravity 3D SQOP function is given as [3]

$$\eta_{g,uv}^{(q)} = C_{g,uv}^{(q)} \int\limits_{-X}^{+X} \int\limits_{-Y}^{+Y} B_a(\mathbf{r}) \frac{\partial^2 s(\mathbf{r},\mathbf{r}_g)}{\partial u_g \partial v_g} g(z) dx dy \,, \; (u,\upsilon{=}x,y,z) \tag{3.14}$$

with

$$C_{g,uv}^{(q)} = \left[\int\limits_{-X}^{+X} \int\limits_{-Y}^{+Y} B_a^2(\mathbf{r}) g(z) dx dy \cdot \int\limits_{-X}^{+X} \int\limits_{-Y}^{+Y} \left| \frac{\partial^2 s(\mathbf{r}, \mathbf{r}_g)}{\partial u_g \partial v_g} \right|^2 g(z) dx dy \right]^{-1/2} ,(u,\upsilon=x,y,z) \qquad (3.15)$$

Each second derivative of $s(\mathbf{r}, \mathbf{r}_g)$ has the role of *source quadrupole scanner*. The second derivatives of $s(\mathbf{r}, \mathbf{r}_g)$ with $u \neq v$ are reported in appendix c.

Finally, the gravity 3D SOOP function is given as [3]

$$\eta_{h,uvw}^{(o)} = C_{h,uvw}^{(o)} \int\limits_{-X}^{+X} \int\limits_{-Y}^{+Y} B_a(\mathbf{r}) \frac{\partial^3 s(\mathbf{r}, \mathbf{r}_h)}{\partial u_h \partial v_h \partial w_h} g(z) dx dy , (u,\upsilon,w=x,y,z) \qquad (3.16)$$

with

$$C_{h,uvw}^{(o)} = \left[\int\limits_{-X}^{+X} \int\limits_{-Y}^{+Y} B_a^2(\mathbf{r}) g(z) dx dy \cdot \int\limits_{-X}^{+X} \int\limits_{-Y}^{+Y} \left| \frac{\partial^3 s(\mathbf{r}, \mathbf{r}_h)}{\partial u_h \partial v_h \partial w_h} \right|^2 g(z) dx dy \right]^{-1/2} , (u,\upsilon,w=x,y,z) \qquad (3.17)$$

Each third derivative of $s(\mathbf{r}, \mathbf{r}_h)$ takes the role of *source octopole scanner*. Its expression for $u \neq v \neq w$ is reported in appendix c.

3.3 Synthetic examples

We show a few synthetic examples, in order to highlight the main aspects of this GPT multipole generalisation.

3.3.1 The one-cube model

At first, we consider the cube model, which is assigned a density contrast $\Delta\sigma = 0.5$ g/cm^3, sides 6 m long parallel to the coordinate axes and ΔM centre at x=0, y=0, z=6 m. The B_a dataset has been calculated at the nodes of a square grid with a step of 2 m from -18 m to 18 m along both the x- and y-axis, using the formula for the rectangular parallelepiped reported by Parasnis [39, p.81, eq.2.27]. Figure 3.3 shows the calculated

B_a map on the x,y plane. We remind that an identical B_a image results if a change of the model distance scale is made, provided that the B_a values are all multiplied by the same scale factor.
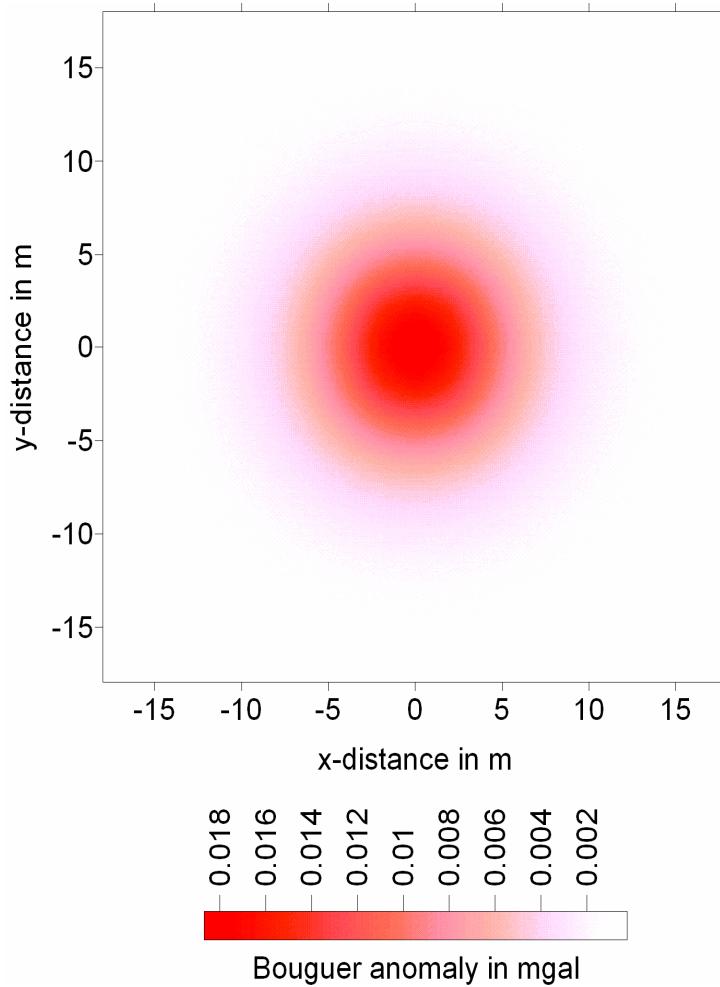

Figure 3.3 The B_a map for the one-cube model with $\Delta\sigma$=0.5 g/cm³, sides 6 m long and ΔM centre at x=0, y=0 and z=6 m.

Figure 3.4 shows the results from the application of the multipole GPT algorithms to the B_a map in figure 3.3 . For the sake of clarity, in this and all of the following 3D plots we will show sufficiently small SPOP, SDOP, SQOP and SOOP nuclei, each enclosing the maximum absolute value (MAV) of the corresponding η- function.

The SPOP image shows a positive nucleus around the ΔM source centre. The SDOP image shows, instead, three distinct doublets of nuclei with opposite sign very close to the centres of the corresponding opposite faces of the cube. Three distinct quadruplets appear around the centres of the cube sides in the SQOP tomographies of the off-

diagonal terms, and an octoplet located at the vertices of the cube is the peculiar result from the SOOP image.
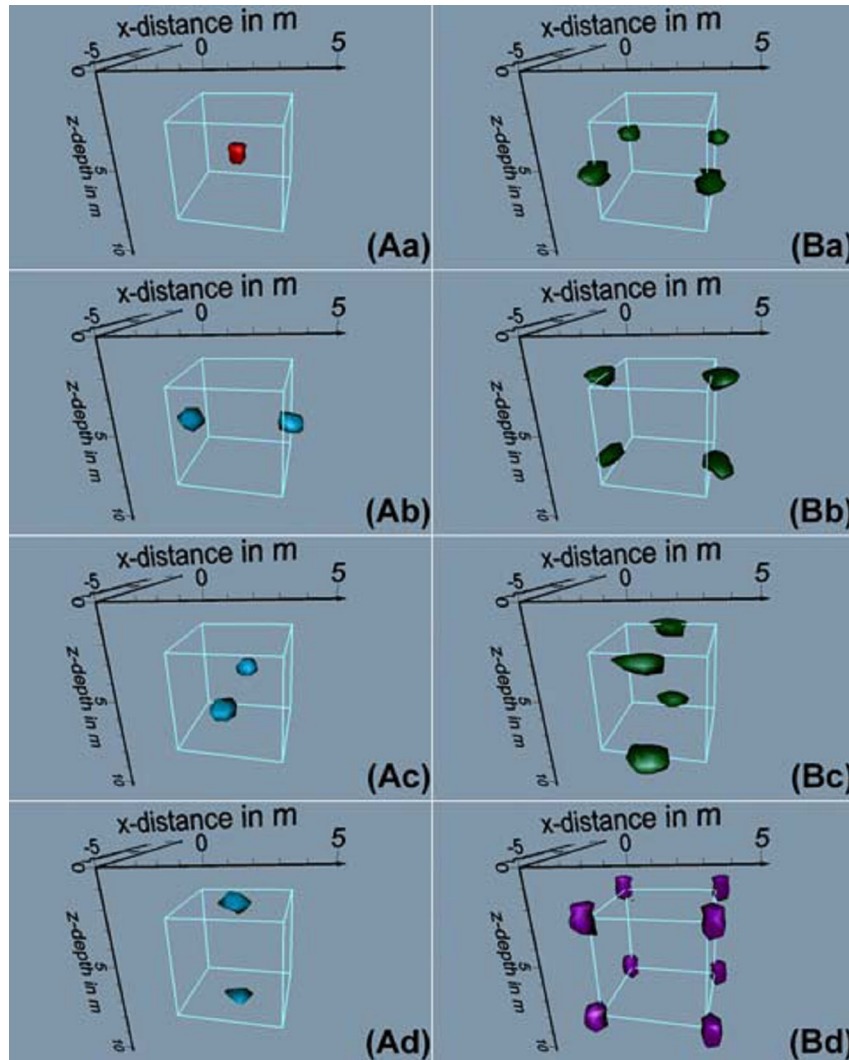
Figure 3.4 The SPOP (Aa), *x*-SDOP (Ab), *y*-SDOP (Ac), *z*-SDOP(Ad), *xy*-SQOP (Ba), *xz*-SQOP (Bb), *yz*-SQOP (Bc) and *xyz*-SOOP (Bd) tomographies derived from the B_a synthetic map in figure 3.3. The body with light blue lines is the cube model.

The parameters characterising the nuclei drawn in figure 3.4 are listed in table 3.1 appendix d. A shift of 0.1 m along the z-axis is estimated for the cube centre from its true position. Furthermore, an average error of about 3% affects the estimate of the side length of the cube, from the distance between the MAV points of two opposite nuclei in each multiplet. Of practical interest is to retrieve shape and position of the source body.

Figure 3.5 suggests that a quick modelling can be done, by plotting into a single image all of the nuclei drawn in figure 3.4.
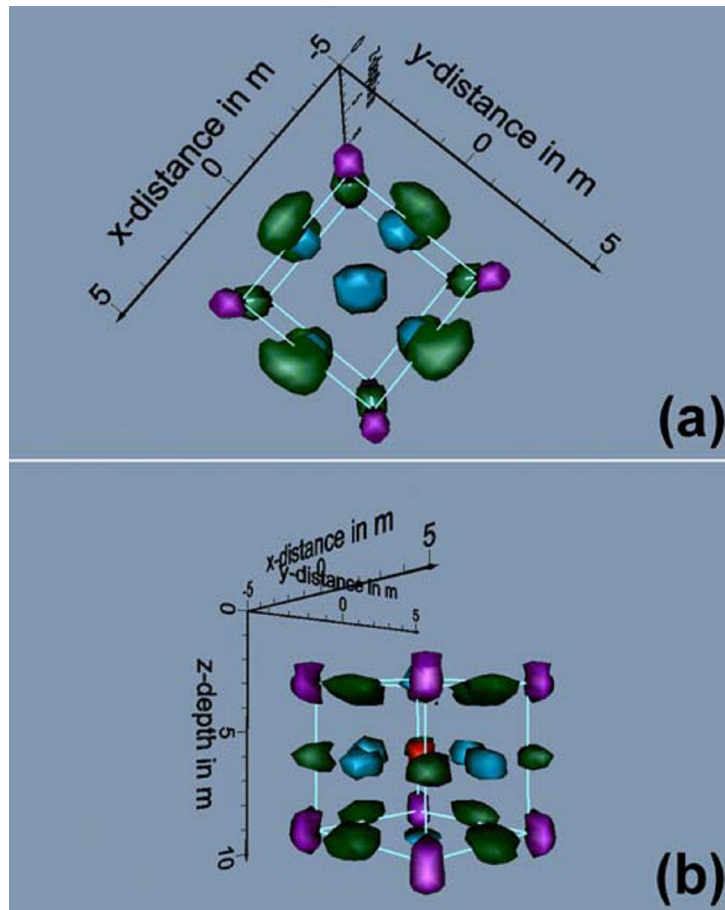
Figure 3.5 A joint representation of the SPOP (red), SDOP (light blue), SQOP (green) and SOOP (purple) nuclei, viewed from top (a) and laterally (b), useful to retrieve the source body of the B_a map in figure 3.3.

3.3.2 The sphere model

The B_a map in figure 3.3 has a very close resemblance with the map generated by a spherical body. It is thus instructive to analyse the GPT response of a sphere. To this purpose, we consider a sphere model, which is given $\Delta\sigma = 0.5$ g/cm^3, radius 3 m and ΔM centre at x=0, y=0, z=6 m. The B_a map has been computed at the nodes of a square grid with the same characteristics as in the previous case, using the formula for the sphere reported by Parasnis [39, p.76, eq.3.20]. Figure 3.6 depicts the B_a map thus obtained.
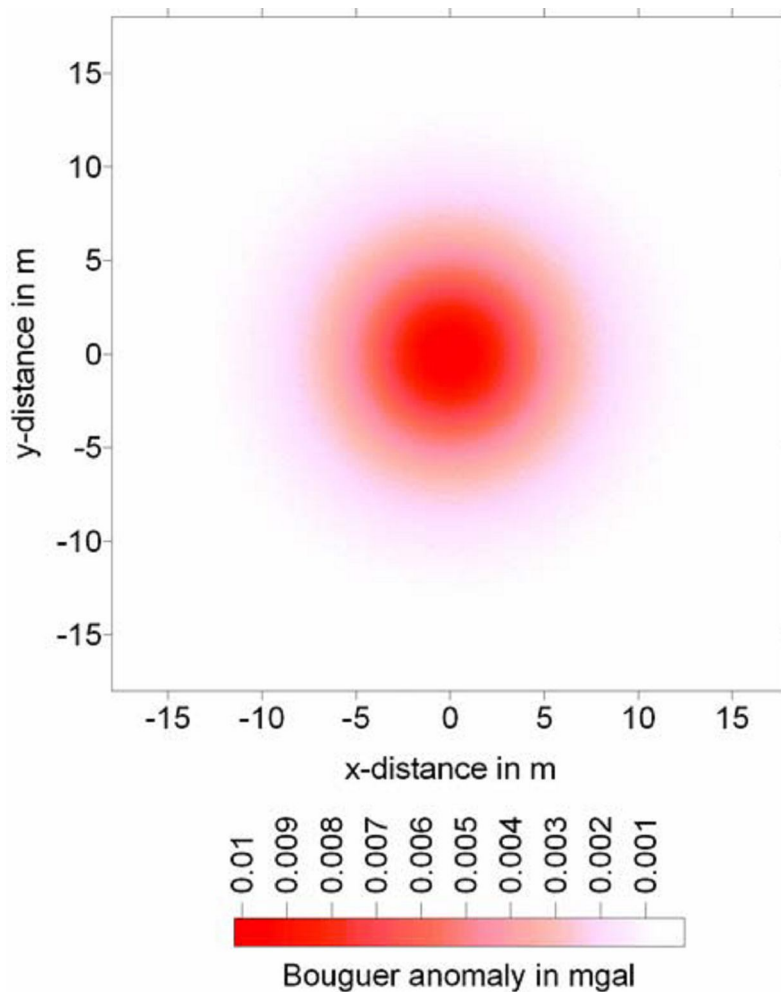
Figure 3.6 The B_a map for the sphere model with $\Delta\sigma = 0.5$ g/cm^3, radius 3 m and ΔM centre at x= 0, y= 0 and z= 6 m.

Figure 3.7 shows the results from the application of the multipole GPT imaging. As previously, in the SPOP image a nucleus appears about the ΔM centre.
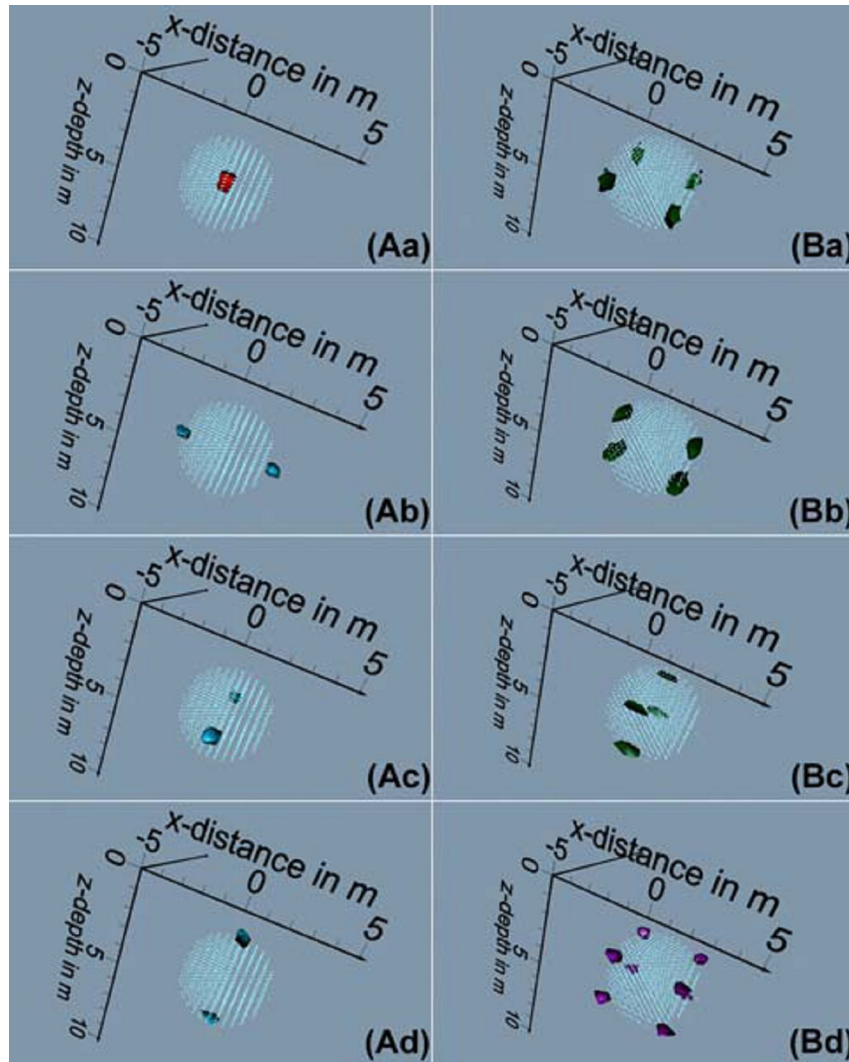

Figure 3.7 The SPOP (Aa), *x*-SDOP (Ab), *y*-SDOP (Ac), *z*-SDOP (Ad), *xy*-SQOP (Ba), *xz*-SQOP (Bb), *yz*-SQOP (Bc) and *xyz*-SOOP (Bd) tomographies derived from the *Ba* map in figure 3.6. The body with light blue scatter plot is the sphere model.

The SDOP images show the three doublets of nuclei with opposite sign closely where the coordinate axes cross the sphere. The nuclei of the off diagonal SQOP quadruplets and the SOOP octoplet also appear adjacent to the sphere. Considered singularly, the SPOP, SDOP, SQOP and SOOP nuclei are so regularly located that no difference can be detected with respect to the previous cube model. The situation changes notably if we plot the nuclei altogether into a multipole image as in figure 3.8. It is no longer possible, now, to combine a set of SDOP, SQOP and SOOP nuclei

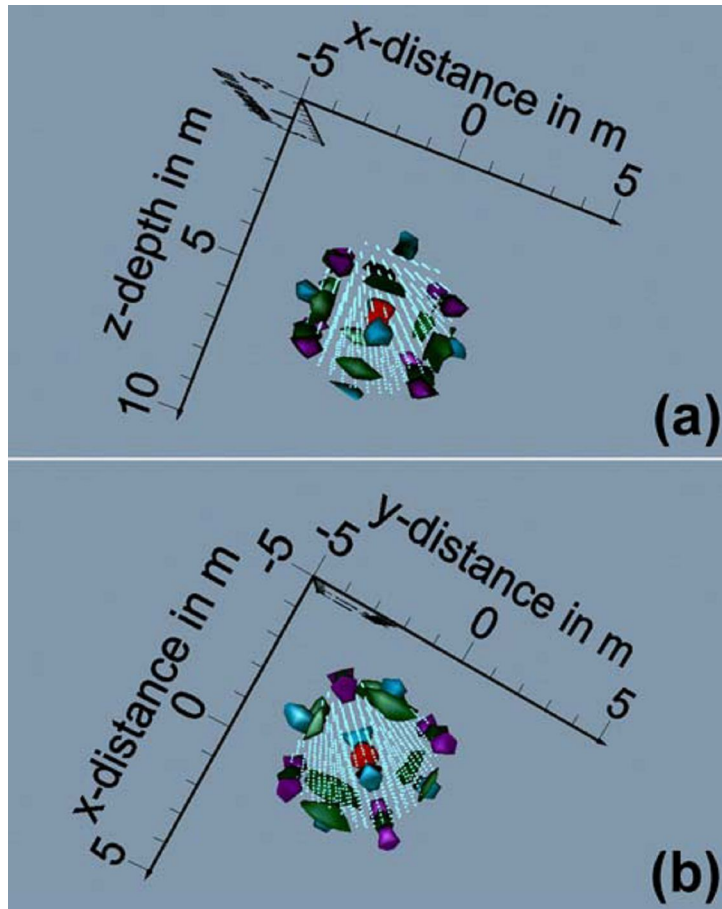crossed by a single plane as in the previous case. In other words, a cube's face can no longer be traced.

Figure 3.8 A joint representation of the SPOP (red), SDOP (light blue), SQOP (green) and SOOP (purple) nuclei under two different angles of view, useful to retrieve the source body of the B_a map in figure 3.6.

The multipole GPT seems thus capable to differentiate the response of a cube from that of a sphere. The parameters of the SPOP, SDOP, SQOP and SOOP nuclei depicted in figure 3.7.

3.3.3 The rotated and tilted cube model

We show now what happens when the sides of the cube are no longer parallel to the reference coordinate axes. A new model is thus analysed by rotating the cube previously dealt with by 45° around both the vertical axis and the *y*-oriented horizontal axis through the ΔM centre. Figure 3.9 shows the B_a map of this new source body configuration. Figure 3.10 illustrates the results from the application of the multipole GPT imaging.
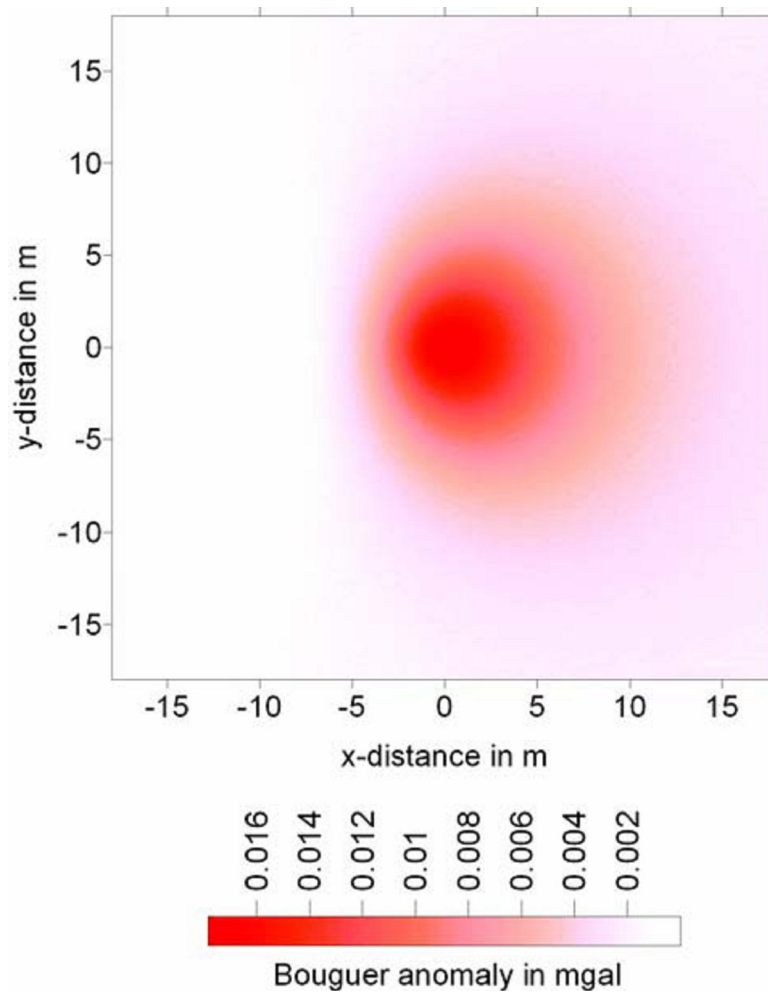

Figure 3.9 The B_a map for the tilted cube model with same parameters as in figure 3.3, rotated by 45° around the vertical and horizontal axes through the ΔM centre.

The SPOP image still shows a nucleus located around the ΔM centre. On the contrary, the SDOP, SQOP and SOOP nuclei exhibit a mixed behaviour compared with that of the coaxial cube model. While in the former case they distinctly represent the

faces, corners and vertices of the cube, respectively, now the same multiplets can indistinctly simulate any of these geometrical features. The only regularity is that the nuclei are always revealed in homologous couples. However, it must be stressed that this behaviour is not casual, since our procedure simply implies the search for the MAV points of the first, second and third order crossed derivatives of the kernel function with respect to the reference axes.
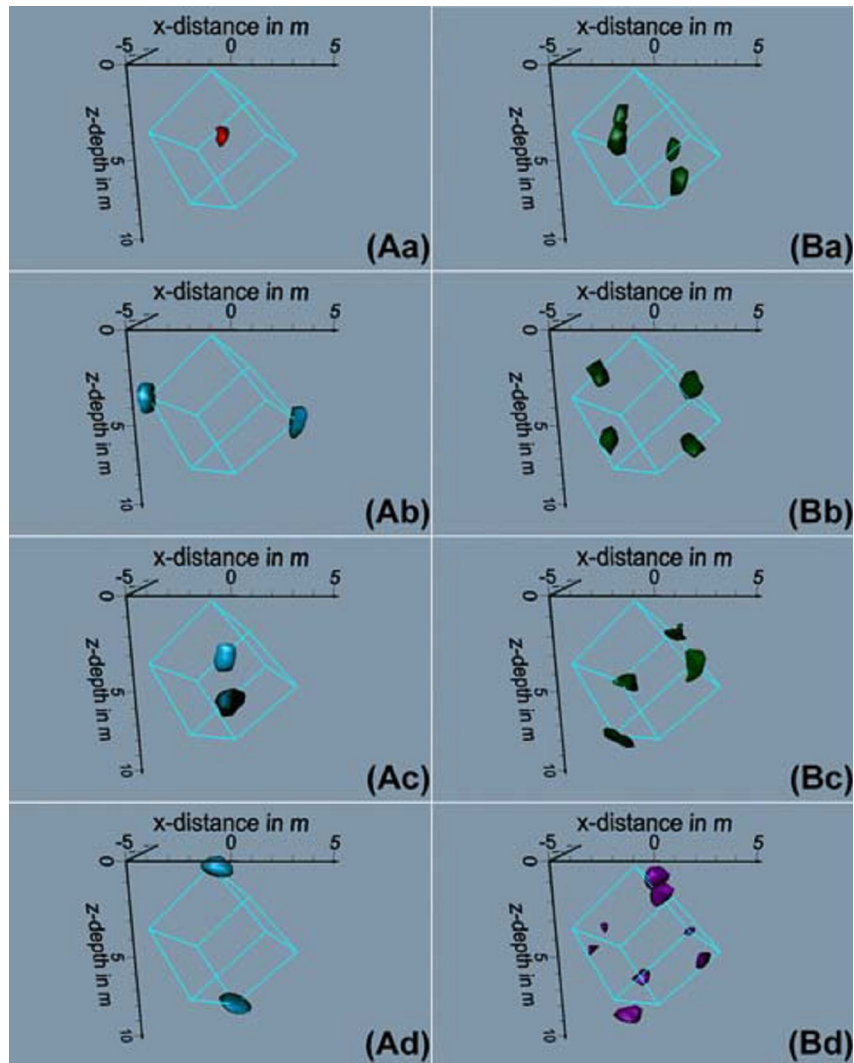

Figure 3.10 The SPOP (Aa), *x*-SDOP (Ab), *y*-SDOP (Ac), *z*-SDOP(Ad), *xy*-SQOP (Ba), *xz*-SQOP (Bb), *yz*-SQOP (Bc) and *xyz*- SOOP (Bd) tomographies derived from the B_a synthetic map drawn in figure 3.9. The body with light blue lines is the inclined cube model.
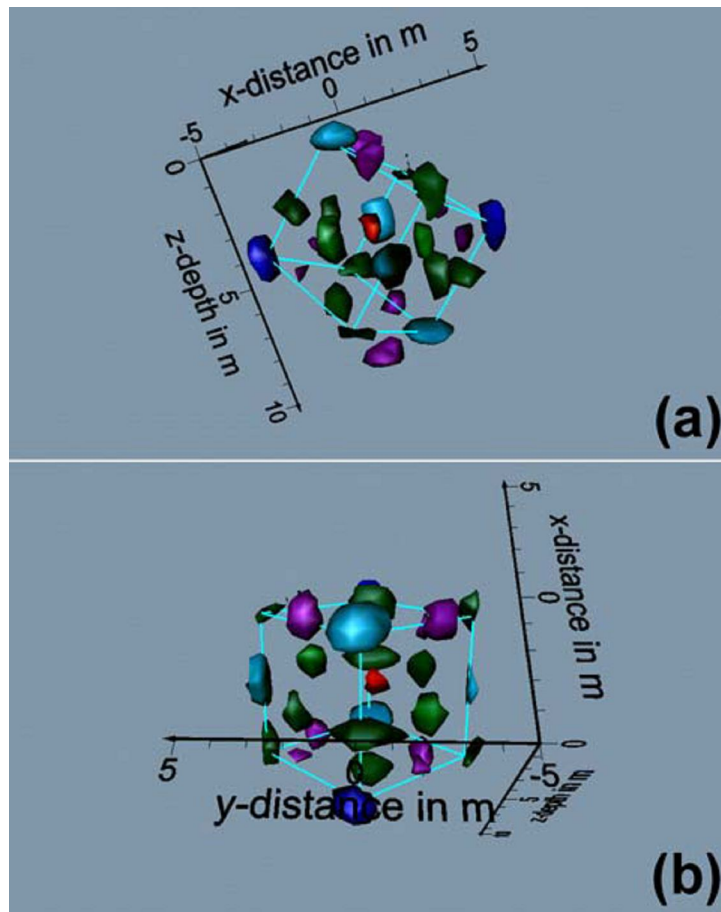
Figure 3.11 A joint representation of the SPOP (red), SDOP (light blue), SQOP (green) and SOOP (purple) nuclei, under two different angles of view, useful to retrieve the source body of the *Ba* map in figure 3.9.

3.3.4 The two prism model

The forth example is the coaxial two prisms model, whose aim is to test the resolution power of the new GPT method. The first prism is simply a cube with $\Delta\sigma$ =0.5 g/cm^3 and the second one is a parallelepiped with $\Delta\sigma$ =-1.0 g/cm^3. Three cases are shown with three different distances between the ΔM centres of the two prisms. Positions and side lengths of the two bodies are detailed in the caption of figure 3.12. The B_a datasets have been computed at the nodes of a square grid by a 2 m step in the rectangle [-60,60]×[-30,30] m^2. Figure 3.12 shows the B_a maps for the three cases in order of decreasing distance between the centres from the top (a) to the bottom plot (b).

It is quite evident that the decreasing distance is the cause of an increasing compression of the B_a contour lines in the region of highest mutual interference.
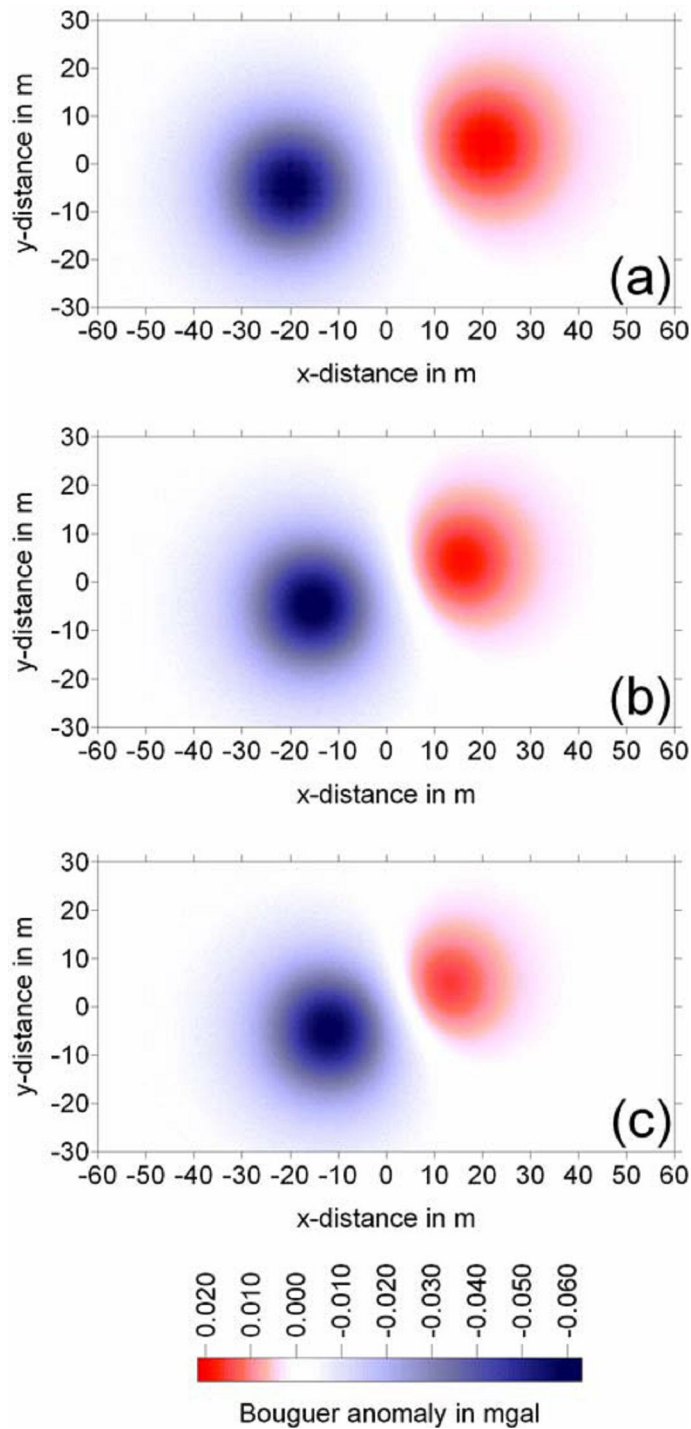

Figure 3.12 The B_a map for the two prisms model made of a cube with $\Delta\sigma$ =0.5 g/cm³, side 12 m long and centre at *x*=20 m (a), *x*=14.5 m (b) and *x*=11 m (c), *y*=4 m, *z*=15 m, and a parallelepiped with $\Delta\sigma$ =-1.0 g/cm³, *x*- and *z*-oriented sides 13 m long and y-oriented sides 13.5 m long, and centre at *x*=-20 m (a), *x*=-15 m (b) and *x*=-11.5 m (c), *y*=-4.75 m, *z*=15 m.

Figure 3.13 displays the GPT results for the three cases, where, for brevity only the combined multipole images are reported.
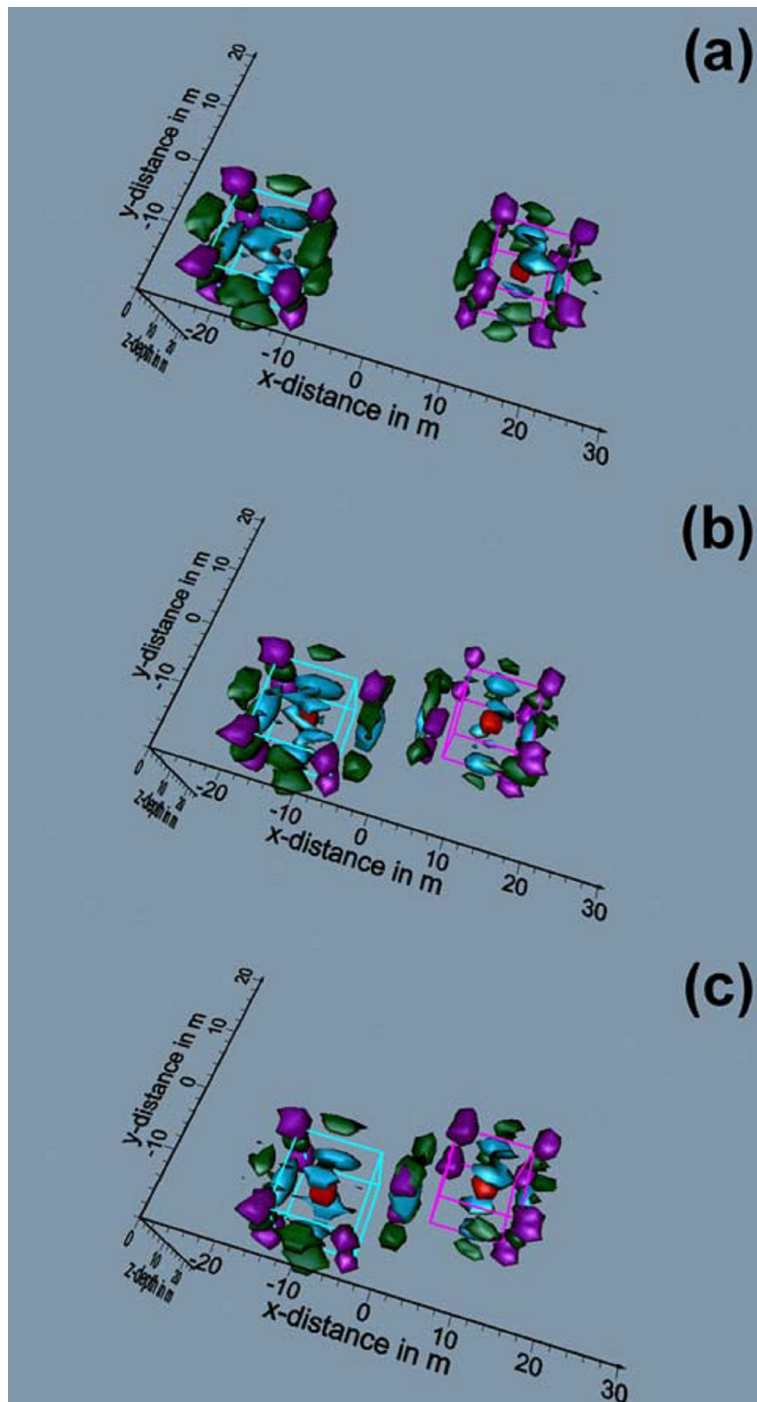

Figure 3.13 A joint representation of the SPOP (red), SDOP (light blue), SQOP (green) and SOOP (purple) nuclei for the two-cube model with decreasing distance between the centres of the two cubes. The sequence of the images is the same as that of the B_a maps in figure 3.12.

In the top one, which refers to a distance between the centres greater than 3 times the average side length of the bodies, the interaction between the two prisms is rather negligible and their true shape can still be recognised. In the middle image, which refers to a distance between the centres of about 2,5 times the average side length, all of the facing SDOP, SQOP and SOOP nuclei depart from their initial places to converge to the centre of the two bodies' system. Finally, in the bottom picture, which refers to a distance a little greater than 2 times the average side length, the detached facing nuclei of same type are wholly melted midway between the prisms. The facing faces, corners and vertices of the two nearby bodies have therefore completely lacked resolution.

3.4 A field example

We show the application of the 3D GPT to a gravity survey of Mt. Etna (Eastern Sicily, Italy), carried out in the frame of a multi-method geophysical project, aimed at delineating the structural setting of the whole volcanic apparatus. Etna is the biggest and most active volcano in Southern Europe, which formed within a large extension zone related to the subduction of the African under the Eurasian Plate. Figure 3.14 shows the survey area and the relative B_a residual map, obtained from the B_a field map after the application of a 2D high-pass filter of 50 km cut-off wavelength. The reference mean crustal density of 2.67 g/cm^3 was taken for slab and terrain corrections. Further details on field data acquisition and processing are in [22] The B_a residual map was already elaborated by the GPT method, limitedly, however, only to the SPOP analysis [29].
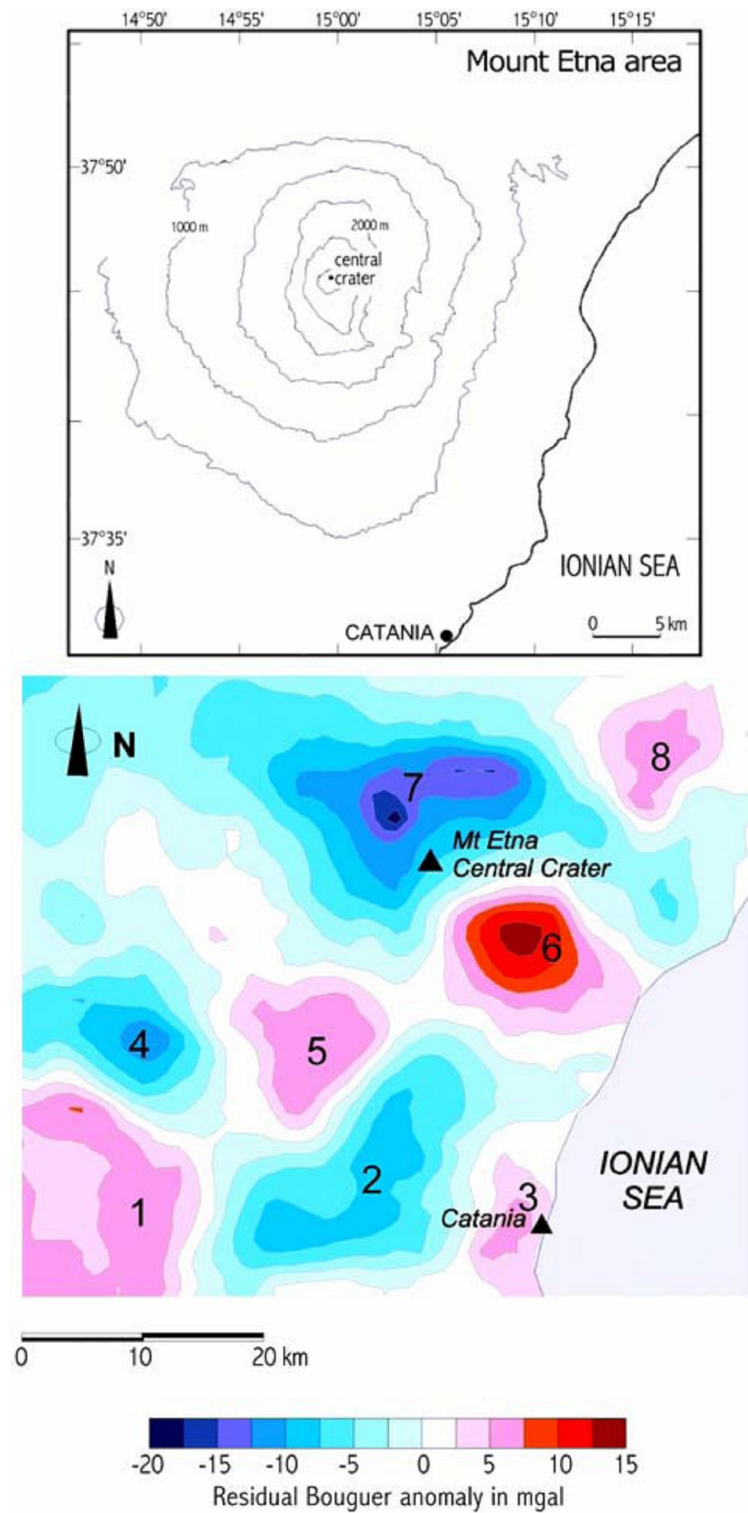
Figure 3.14 The Mt. Etna survey area and corresponding residual B_a map [22]. Numbers in the *Ba* map indicate the dominant closed anomalies.

The SPOP image in figure 3.15 displays a set of distinct nuclei containing the poles, which are interpreted as the ΔM centres responsible of the B_a closed anomalies in figure 3.14 . Combining in pairs and altogether the SPOP, SDOP, SQOP and SOOP nuclei into single pictures, regardless of their algebraic sign, the images in figure 3.16 are obtained.
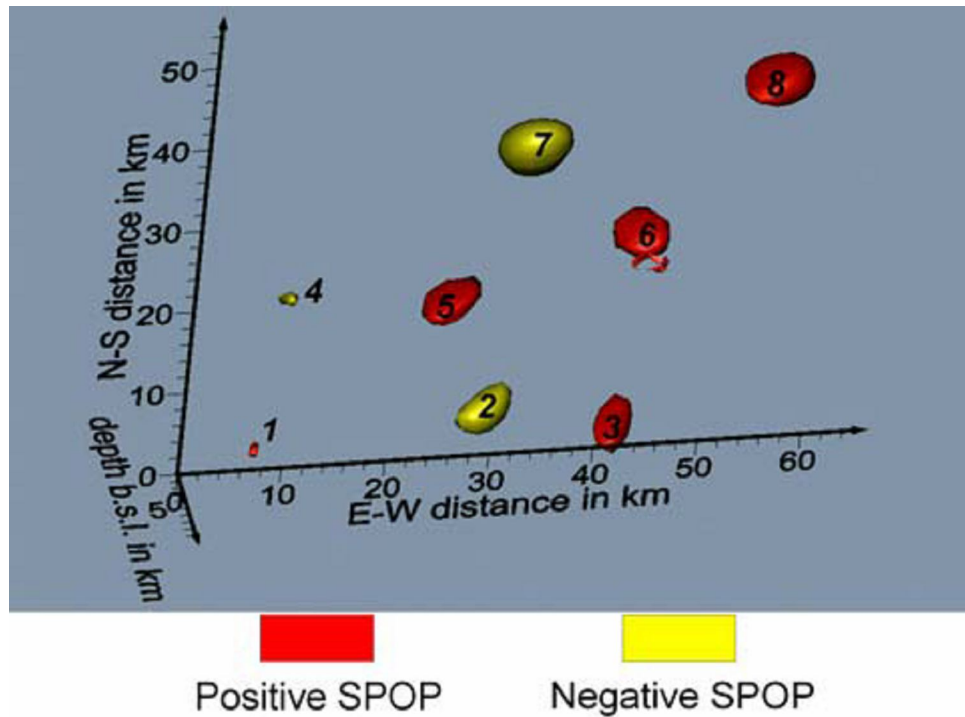

Figure 3.15 The Mt. Etna 3D SPOP tomography of the residual gravity map reported in figure 3.14.

Figure 3.16 shows a complex assemblage of the SDOP, SQOP and SOOP multiplets. All the related nuclei appear clustered around the 8 poles of figure 3.15, tending thus to configure 8 distinct blocks. Some remarkable features can now be noted in this 3D block pattern.

Compared with the results from the previous synthetic examples with simple confined bodies, the first feature is a rather frequent incompleteness of the multiplets around the poles. For instance, the three doublets of the dipole sources never total 6 nuclei, and in one case, around the pole n.1 in figure 3.15, they even drop to only 3, one for each doublet. A similar situation occurs for the 3 quadruplets, which drop to only 5 nuclei from a total of 12, around the pole n.3 in figure 3.15, and for the octoplet, which drops to only 2 nuclei from a total of 8, around the pole n.4 in figure 3.15.
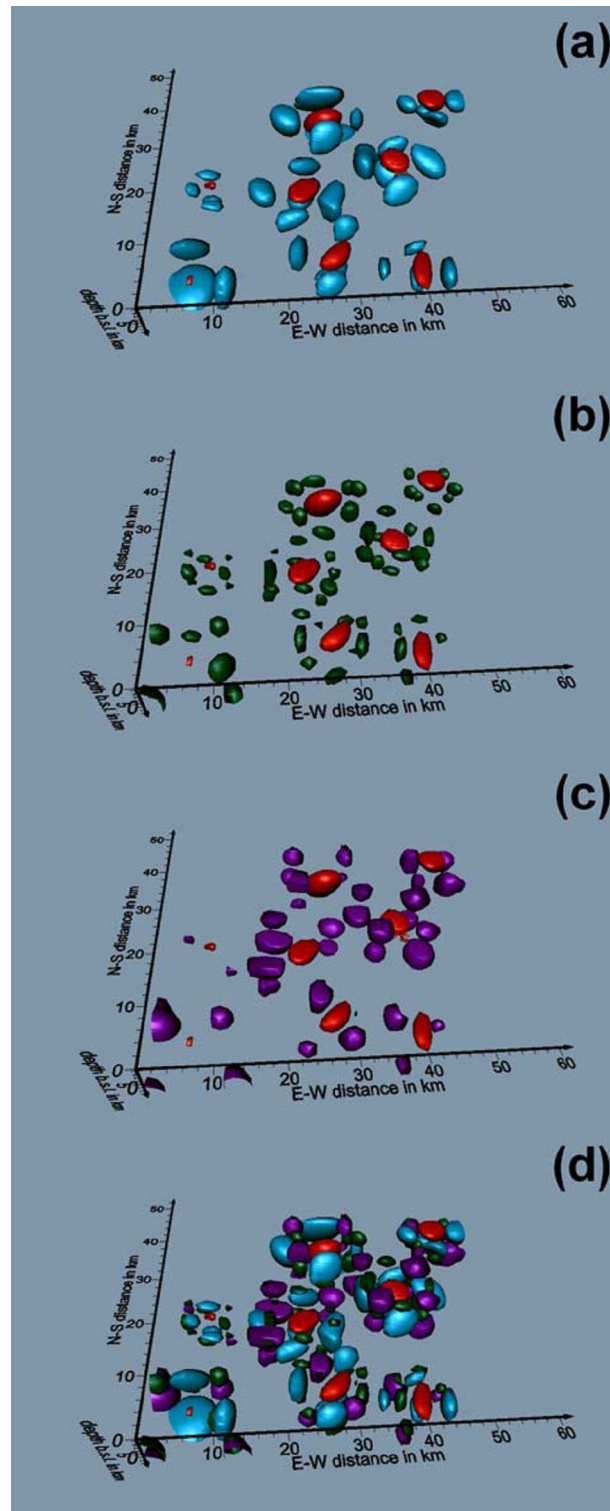
Figure 3.16 A joint representation of the SPOP and SDOP (a), SPOP and SQOP (b), SPOP and SOOP (c), SPOP, SDOP, SQOP and SOOP (d) nuclei, resulting from the application of he GPT method to the Mt. Etna gravity map in figure 3.14.

Also, we do not happen to see in each cluster a number of multiplets, belonging to any of the source typologies, greater than the corresponding maximum number as detected by the GPT of the synthetic cases previously considered. Another feature is the presence of the detachment and melting effects due to closeness of the causative bodies, as explained along with the discussion of the two prisms model. This feature can particularly be viewed in figure 3.16, midway between the poles n.6 and n.7 and the poles n.2 and n.5, marked in figure 3.15. No tilts can be appreciated around any horizontal axis, while moderate horizontal rotations can be observed for the sources n.3, n.4 and n.8, reported in figure 3.15. In conclusion, basing on the above remarked features, an assemblage of vertical prismatic blocks seems to be the most probable gravity model of the Etna apparatus within the first 5 km of depth b.s.l..

The biggest central blocks n.5, n.6 and n.7 appear as truly confined bodies with a roughly quadrangular section. All of the other peripheral blocks, are reasonably to be interpreted as partially unconfined bodies, because of either an insufficient number of data or the lack of a density contrast, at least along one of the reference directions[3]. The geometry of the source bodies responsible of the anomalies in figure 3.14 appears now much better delineated than in the former GPT study by the single SPOP algorithm [28,29]

4. Multipole Self-Potential Tomography

4.1 The basic Self Potential theory

The SP measurements refer to that part of the natural electrical field which is stationary in time, or slowly varying in relation to the time span required for the execution of a survey, and whose current source system is generated and sustained by phenomena occurring underground within geological structures. The most important source mechanism in rocks, which has been proposed to explain SP field data both in exploration geophysics and in tectonophysics, is the so called electrokinetic effect related to the movement of fluids in porous systems in presence of an electrical double layer at the fluid-rock matrix interface. Basically, the electrokinetic effect is included within the constitutive relationships that formalise Onsager's coupled flow theory [20]. From the physical point of view, the common aspect of the many source models is that an electrical charge polarization is developed, which is assumed to be responsible for the electrical current circulation in conductive rocks. It follows that the detected SP anomalies are simply the surface evidence of a more or less steady state of electric polarization. Therefore, in the final interpretation stage, the SP inverse problem merely consists of finding the location and outlining the shape of the electrical charges accumulations underground. SP data are collected in field surveys as potential drops, ΔU, across a passive dipole, normally consisting of a pair of liquid junction copper-copper sulphate porous pots as grounded electrodes. If the dipole length is sufficiently small relative to the expected anomaly wavelengths, the ratio SP drop to dipole length gives an estimate of the component of the natural electrical field along the dipole axis on the measurement surface. The sequence of progressive readings of this ratio along a survey line is currently known as the gradient technique and is the most commonly used procedure in difficult areas. Furthermore, a standard polarity cable- connecting convention, with reversal of leading and trailing electrodes between successive measurements, known as the leapfrog profiling technique, permits measurement of SP

data which is virtually free of electrode polarization error. Finally, the use of loops or two-way profiles helps to eliminate virtually any spurious effects of SP drift, by distributing the tie-in closure error among all the readings around the closed circuit [10].

Let us consider a reference system with a horizontal (x,y)-plane placed at sea level and the z-axis positive downwards, and a 2D datum domain S as in figure 1.1. The S-domain is generally a non-flat ground survey area described by a topographic height function $z(x,y)$. We indicate with $\mathbf{E}_S(\mathbf{r})$ the SP electrical field vector at a set of datum points $\mathbf{r}\equiv[x,y,z(x,y)]$, with $\mathbf{r}\in S$. In areas with rough topography and inaccessible sites the current practice in collecting SP data consists of a continuous displacement of the measuring dipole along a generally irregular network of closed circuits and/or two-way interconnected branched lines. In order to provide a uniform and dense distribution of $\mathbf{E}_S(\mathbf{r})$ data, a pre-processing is required according to the following three steps [41,42]. The first step consists in assigning a zero potential value to an arbitrary reference point in the area, where an electrode had been placed, and in recovering from the original sequence of SP drops, by simple algebraic summation, a new sequence of SP values, all defined to within an unknown common constant. The second step consists in contouring the new set of potential data, in order to draw an SP anomaly map covering the entire survey area, as sketched in figure 1.1. The third step consists in selecting a double set of curvilinear φ- and ψ-profiles with horizontal surface projections onto the horizontal (x,y)-plane, parallel to the x-axis and the y-axis and equally spaced from each other by the spacings Δy and Δx, respectively. Along any φ-profile or ψ-profile, the sampling interval projection onto the (x,y)-plane, equal to Δy and Δx, respectively, is assumed constant and, for the sake of easier calculations, such that $\Delta x=\Delta y=\Delta\tau$, where $\Delta\tau$ is taken once for all as the unique distance discretization element. Using a regular square grid on the (x,y)- plane, at each cross point of every pair of perpendicular x-line and y-line, a pair of values of the electrical field components, $E_\varphi(\mathbf{r})$ and $E_\psi(\mathbf{r})$, is assigned. These are estimated by interpolation from the SP map across dipoles of length $\Delta\varphi$ and $\Delta\psi$, respectively, and attributed to the midpoint of the projected dipoles, both of length $\Delta\tau$. By indicating with ΔU_φ and ΔU_ψ the potential difference across $\Delta\varphi$ and $\Delta\psi$, respectively, we readily obtain the estimates of $E_\varphi(\mathbf{r})$ and $E_\psi(\mathbf{r})$ as

$$E_\varphi(\mathbf{r}) = -\frac{\Delta U_\varphi(\mathbf{r})}{\Delta\varphi} = -\frac{\Delta U_\varphi(\mathbf{r})}{\Delta\tau\left[1+(\Delta z/\Delta\tau)^2\right]^{1/2}} \tag{4.1}$$

$$E_\psi(\mathbf{r}) = -\frac{\Delta U_\psi(\mathbf{r})}{\Delta\psi} = -\frac{\Delta U_\psi(\mathbf{r})}{\Delta\tau\left[1+(\Delta z/\Delta\tau)^2\right]^{1/2}} \tag{4.2}$$

4.2 The generalized formalism for Self Potential

We assume that $\mathbf{E}_S(\mathbf{r})$ can be discretised as

$$\mathbf{E}_S(\mathbf{r}) = \sum_{m=1}^{M}(\mathbf{p}_m\cdot\mathbf{P}_m)\mathbf{s}(\mathbf{r},\mathbf{r}_m) + \sum_{n=1}^{N}(\mathbf{d}_n^u\cdot\mathbf{L}_n^u)\mathbf{s}(\mathbf{r},\mathbf{r}_n)$$
$$+ \sum_{g=1}^{G}(\mathbf{q}_g^{uv}\cdot\mathbf{S}_g^{uv})\mathbf{s}(\mathbf{r},\mathbf{r}_g) + \sum_{h=1}^{H}(\mathbf{o}_h^{uvw}\cdot\mathbf{C}_h^{uvw})\mathbf{s}(\mathbf{r},\mathbf{r}_h) \tag{4.3}$$

The effect of the *M*, *N*, *G* and *H* source elements at a point $\mathbf{r}\in S$ is determined by the vector kernel $\mathbf{s}(\mathbf{r},\mathbf{r}_i)$ ($i=m,n,g,h$), which represents the electrical field vector due to a point positive charge of unitary strength. The components $s_\varphi(\mathbf{r},\mathbf{r}_i)$ and $s_\psi(\mathbf{r},\mathbf{r}_i)$ of $\mathbf{s}(\mathbf{r},\mathbf{r}_i)$ over the *S*-domain are explicitly given as

$$s_\varphi(\mathbf{r},\mathbf{r}_i) = \frac{(x-x_i)+(z-z_i)z_x'}{\left[(x-x_i)^2+(y-y_i)^2+(z-z_i)^2\right]^{3/2}}x_\varphi' \tag{4.4}$$

$$s_\psi(\mathbf{r},\mathbf{r}_i) = \frac{(y-y_i)+(z-z_i)z_y'}{\left[(x-x_i)^2+(y-y_i)^2+(z-z_i)^2\right]^{3/2}}y_\psi' \tag{4.5}$$

where it is $z_x' = \partial z/\partial x$, $z_y' = \partial z/\partial y$, $x_\varphi' = \mathrm{d}x/\mathrm{d}\varphi$ and $y_\psi' = \mathrm{d}y/\mathrm{d}\psi$.

We define the information power Λ, associated with $\mathbf{E}_S(\mathbf{r})$, over the surface *S* as

$$\Lambda = \int_S \mathbf{E}_S(\mathbf{r})\cdot\mathbf{E}_S(\mathbf{r})dS \tag{4.6}$$

$$\Lambda = \sum_{m=1}^{M} p_m \int_S \mathbf{E}_S(\mathbf{r}) \cdot \mathbf{s}(\mathbf{r}, \mathbf{r}_m) dS + \sum_{n=1}^{N} \sum_{u=x,y,z} d_n^u \int_S \mathbf{E}_S(\mathbf{r}) \cdot \frac{\partial \mathbf{s}(\mathbf{r}, \mathbf{r}_n)}{\partial u_n} dS$$

$$+ \sum_{g=1}^{G} \sum_{u=x,y,z} \sum_{v=x,y,z} q_g^{uv} \int_S \mathbf{E}_S(\mathbf{r}) \cdot \frac{\partial^2 \mathbf{s}(\mathbf{r}, \mathbf{r}_g)}{\partial u_g \partial v_g} dS$$

$$+ \sum_{h=1}^{H} \sum_{u=x,y,z} \sum_{v=x,y,z} \sum_{w=x,y,z} o_h^{uvw} \int_S \mathbf{E}_S(\mathbf{r}) \cdot \frac{\partial^3 \mathbf{s}(\mathbf{r}, \mathbf{r}_h)}{\partial u_h \partial v_h \partial w_h} dS \qquad (4.7)$$

Skipping all intermediate steps, we directly arrive at the explicit expressions of the self-potential SPOP, SDOP, SQOP and SOOP functions, using the pair of eq.s 1.8 and 1.9, eq.s 1.10 and 1.11, eq.s 1.12 and 1.13, eq.s 1.14 and 1.15

The self-potential 3D SPOP function is given as

$$\eta_m^{(p)} = C_m^{(p)} \int_{-X}^{+X} \int_{-Y}^{+Y} \mathbf{E}_S(\mathbf{r}) \cdot \mathbf{s}(\mathbf{r}, \mathbf{r}_m) g(z) dx dy \qquad (4.8)$$

with

$$C_m^{(p)} = \left[\int_{-X}^{+X} \int_{-Y}^{+Y} E_S^2(\mathbf{r}) g(z) dx dy \cdot \int_{-X}^{+X} \int_{-Y}^{+Y} s^2(\mathbf{r}, \mathbf{r}_m) g(z) dx dy \right]^{-1/2} \qquad (4.9)$$

The self-potential 3D SDOP function is given as

$$\eta_{n,u}^{(d)} = C_{n,u}^{(d)} \int_{-X}^{+X} \int_{-Y}^{+Y} \mathbf{E}_S(\mathbf{r}) \cdot \frac{\partial \mathbf{s}(\mathbf{r}, \mathbf{r}_n)}{\partial u_n} g(z) dx dy \quad , (u=x,y,z) \qquad (4.10)$$

with

$$C_{n,u}^{(d)} = \left[\int_{-X}^{+X} \int_{-Y}^{+Y} E_S^2(\mathbf{r}) g(z) dx dy \cdot \int_{-X}^{+X} \int_{-Y}^{+Y} \left| \frac{\partial \mathbf{s}(\mathbf{r}, \mathbf{r}_n)}{\partial u_n} \right|^2 g(z) dx dy \right]^{-1/2} , (u=x,y,z) \qquad (4.11)$$

Each first derivative of $s(\mathbf{r},\mathbf{r}_n)$ has the role of *source dipole scanner*. The first derivatives of the components $s_\varphi(\mathbf{r},\mathbf{r}_n)$ and $s_\psi(\mathbf{r},\mathbf{r}_n)$ of $\mathbf{s}(\mathbf{r},\mathbf{r}_n)$ over the *S*-domain are reported in appendix e.

The self-potential 3D SQOP function is given as [4]

$$\eta_{g,uv}^{(q)} = C_{g,uv}^{(q)} \int\limits_{-X}^{+X} \int\limits_{-Y}^{+Y} \mathbf{E}_S(\mathbf{r}) \cdot \frac{\partial^2 \mathbf{s}(\mathbf{r},\mathbf{r}_g)}{\partial u_g \partial v_g} g(z) dx dy \quad ,(u,\upsilon = x,y,z) \tag{4.12}$$

with

$$C_{g,uv}^{(q)} = \left[\int\limits_{-X}^{+X} \int\limits_{-Y}^{+Y} E_S^2(\mathbf{r}) g(z) dx dy \cdot \int\limits_{-X}^{+X} \int\limits_{-Y}^{+Y} \left| \frac{\partial^2 \mathbf{s}(\mathbf{r},\mathbf{r}_g)}{\partial u_g \partial v_g} \right|^2 g(z) dx dy \right]^{-1/2} ,(u,\upsilon = x,y,z) \tag{4.13}$$

Each second derivative of $s(\mathbf{r},\mathbf{r}_g)$ has the role of *source quadrupole scanner*. The useful second derivatives of the components $s_\varphi(\mathbf{r},\mathbf{r}_g)$ and $s_\psi(\mathbf{r},\mathbf{r}_g)$ of $\mathbf{s}(\mathbf{r},\mathbf{r}_g)$ over the *S*-domain with $u \neq v$ are reported in appendix e.

The self-potential 3D SOOP function is given as [4]

$$\eta_{h,uvw}^{(o)} = C_{h,uvw}^{(o)} \int\limits_{-X}^{+X} \int\limits_{-Y}^{+Y} \mathbf{E}_S(\mathbf{r}) \cdot \frac{\partial^3 \mathbf{s}(\mathbf{r},\mathbf{r}_h)}{\partial u_h \partial v_h \partial w_h} g(z) dx dy \, , (u,\upsilon,w = x,y,z) \tag{4.14}$$

with

$$C_{h,uvw}^{(o)} = \left[\int\limits_{-X}^{+X} \int\limits_{-Y}^{+Y} E_S^2(\mathbf{r}) g(z) dx dy \cdot \int\limits_{-X}^{+X} \int\limits_{-Y}^{+Y} \left| \frac{\partial^3 \mathbf{s}(\mathbf{r},\mathbf{r}_h)}{\partial u_h \partial v_h \partial w_h} \right|^2 g(z) dx dy \right]^{-1/2} , (u,\upsilon,w = x,y,z) \tag{4.15}$$

Each third derivative of $s(\mathbf{r},\mathbf{r}_h)$ has the role of *source octopole scanner*. The third derivatives of the components $s_\varphi(\mathbf{r},\mathbf{r}_h)$ and $s_\psi(\mathbf{r},\mathbf{r}_h)$ of $\mathbf{s}(\mathbf{r},\mathbf{r}_h)$ over the *S*-domain with $u \neq v \neq w$ are reported in appendix e.

4.3 Synthetic examples

We show some synthetic examples, in order to outline the main aspects of the multipole generalisation of the SP probability tomography.

4.4.1 The one-cube model

At first, we consider a coaxial cube model with sides 6 m long parallel to the coordinate axes and centre at x=0, y=0, z=6 m. A positive charge of 0.5 C is assumed uniformly distributed on the surface of the cube with a charge surface density $\Delta\sigma \cong 2.315 \cdot 10^{-3}$ C/m^2. The SP data have been computed at the nodes of a square grid using a 1 m step from −18 m to 18 m along both the x-axis and y-axis. Figure 4.1 shows the synthetic SP map on the (x,y)-plane.
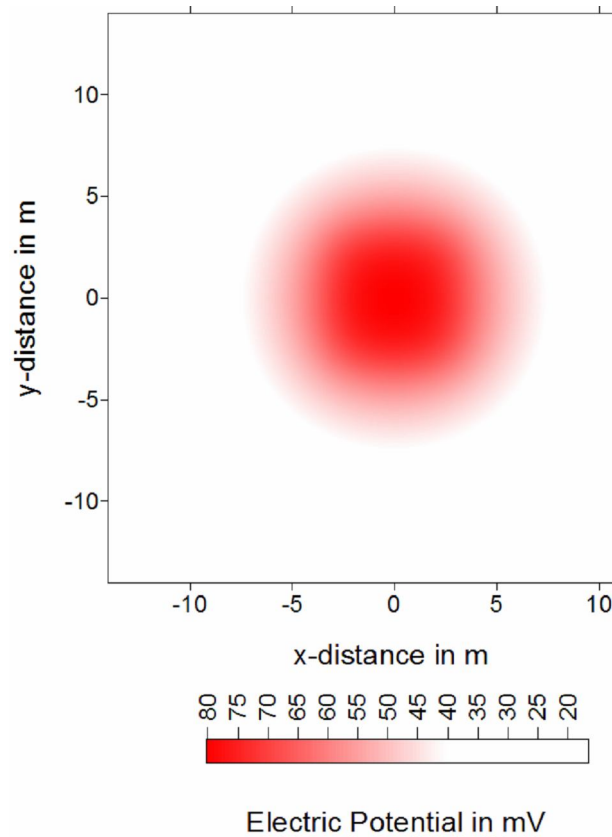
Figure 4.1. The SP map for the cube model with a positive charge surface density $\Delta\sigma \cong 2.315 \cdot 10^3$ C/m², sides 6 m long and centre at x=0, y=0 and z=6 m.

Figure 4.2 shows the results from the application of the multipole probability tomography algorithm to the SP map in figure 4.1. Since no topographic effects have been simulated, the scanner functions used to compute the η functions have been obtained from the previous formulae putting $z'_x = z'_y = 0$, $x'_\phi = y'_\psi = 1$ and g(z)=1.
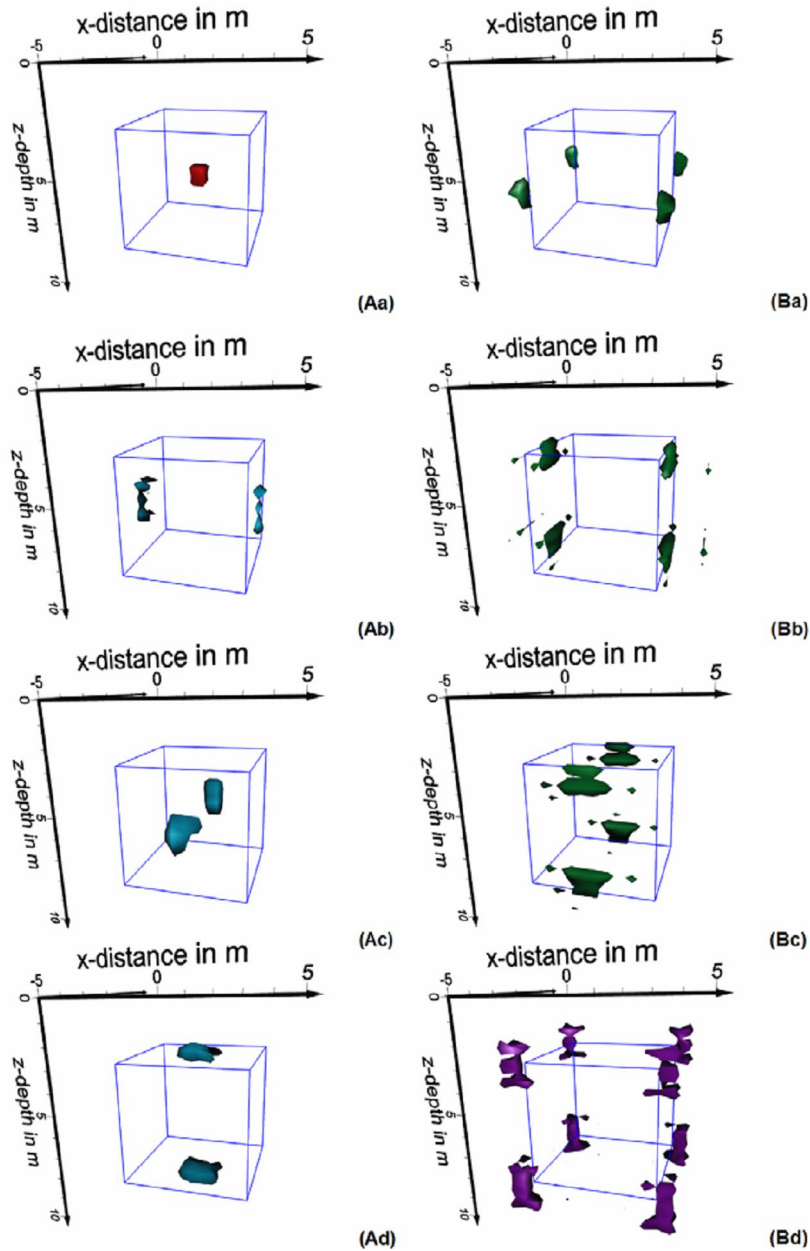

Figure 4.2 The SPOP (Aa), *x*-SDOP (Ab), *y*-SDOP (Ac), *z*-SDOP (Ad), *xy*-SQOP (Ba), *xz*-SQOP (Bb), *yz*-SQOP (Bc) and *xyz*-SOOP (Bd) tomographies derived from the SP synthetic map in figure 4.1. The body with blue lines is the cube model.

For the sake of clarity, in all of the 3D probability tomography plots we will show sufficiently small SPOP, SDOP, SQOP and SOOP nuclei, each enclosing the maximum absolute value (MAV) of the corresponding η-function.

The SPOP image shows a positive nucleus around the cube centre. The SDOP image shows, instead, three distinct doublets of nuclei with opposite sign very close to the centres of the corresponding opposite faces of the cube. Three distinct quadruplets appear around the centres of the cube sides in the SQOP tomographies of the off-diagonal terms, and an octoplet located at the vertices of the cube is the peculiar result from the SOOP image. The parameters of the nuclei in figure 4.2 are listed in table 4.1 appendix f.
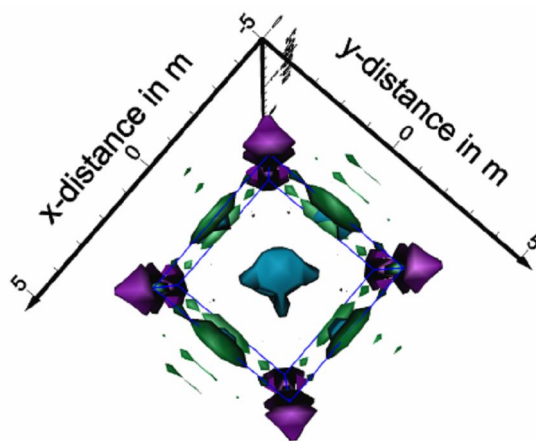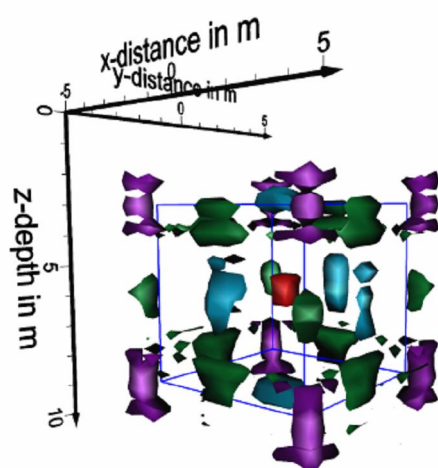
Figure 4.3 A joint representation of the SPOP (red), SDOP (light blue), SQOP (green) and SOOP (purple) nuclei, viewed from top (a) and laterally (b), useful to retrieve the source body of the SP map in figure 4.1.

A shift of 0.1 m along the *z*-axis is estimated for the cube centre from its true position. Furthermore, an average error of about 3% affects the estimate of the side length of the cube, from the distance between the MAV points of two opposite nuclei in each multiplet. Of practical interest is to retrieve shape and position of the source body. Figure 4.3 suggests that a quick modelling can be done, by plotting into a single image all of the nuclei drawn in figure 4.2.

4.4.2 The single point charge model

The SP map in figure 4.1 has a very close resemblance with the map due to a point charge. To this aim, we consider a point charge of 0.5 C placed at *x*=0, *y*=0, *z*=6 m. The SP map has been computed at the nodes of a square grid with the same characteristics as in the previous case. Figure 4.4 depicts the SP map thus obtained.
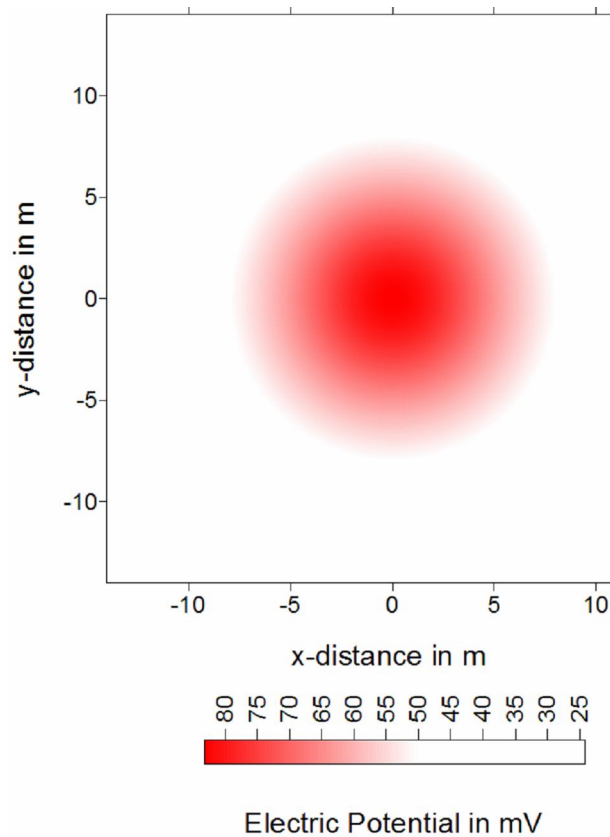

Figure 4.4 The SP map due to a point charge of 0.5 C placed at *x*=0, *y*=0 and *z*=6 m.

Figure 4.5 shows the results from the application of the multipole tomography imaging. As in the coaxial cube case, the SPOP image gives a clear indication as to the correct position of the point charge.
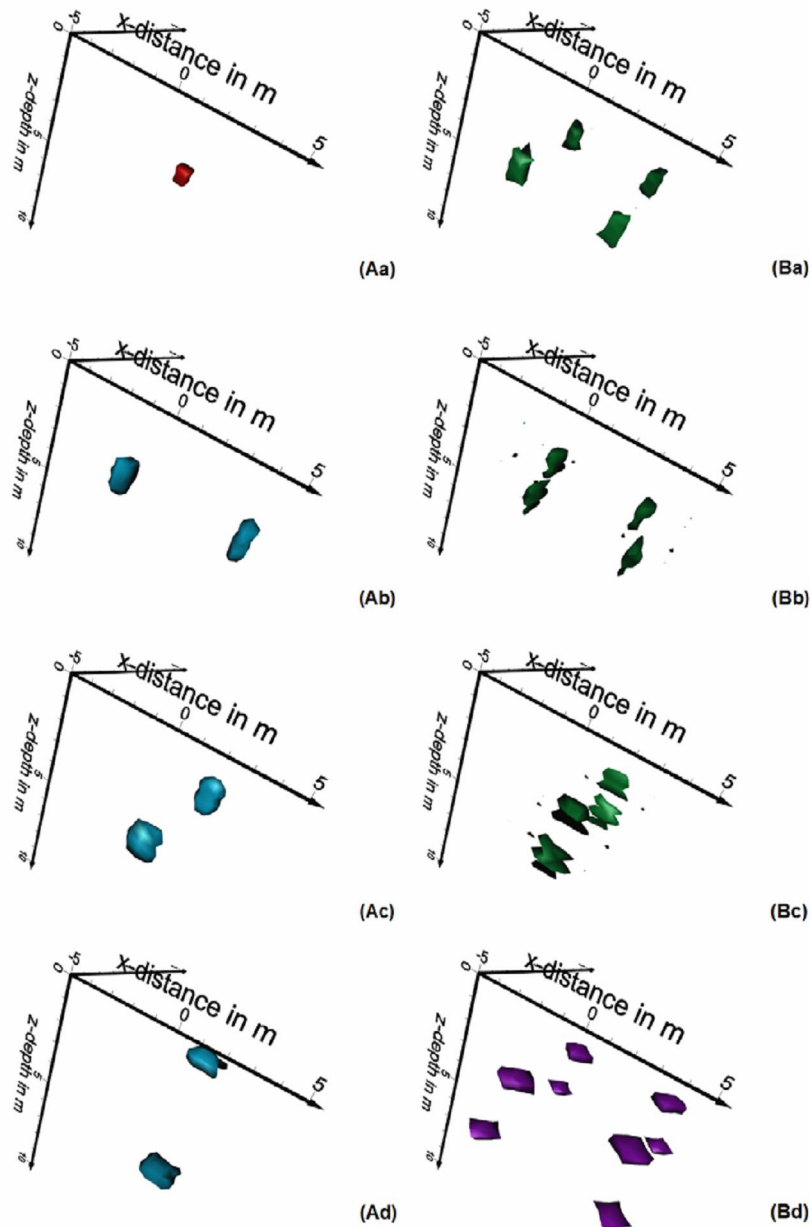

Figure 4.5 The SPOP (Aa), *x*-SDOP (Ab), *y*-SDOP (Ac), *z*-SDOP (Ad), *xy*-SQOP (Ba), *xz*-SQOP (Bb), *yz*-SQOP (Bc) and *xyz*-SOOP (Bd) tomographies derived from the SP map in figure 4.4.

However, in spite of the fact that the source is a single pole, SDOP, SQOP and SOOP nuclei also appear so regularly located that, considered singularly, no difference

can be detected with respect to the previous cube model. The situation changes considerably if we plot the SDOP, SQOP and SOOP nuclei altogether into a multipole image as in figure 4.6. It is no longer possible, now, to combine a set of SDOP, SQOP and SOOP nuclei crossed by a single plane as in the previous case. In other words, a cube's face can no longer be traced.
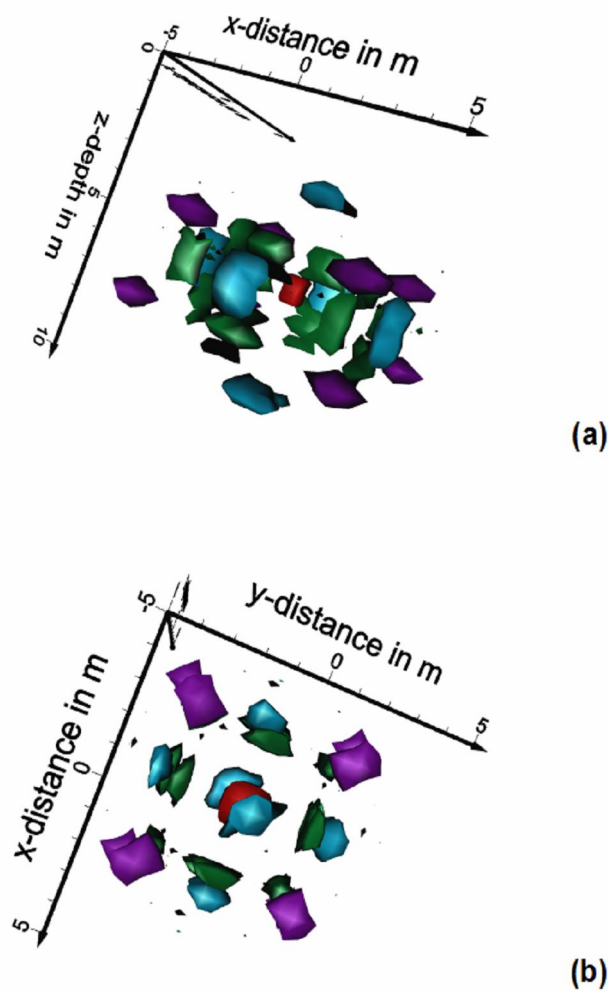

Figure 4.6 A joint representation of the SPOP (red), SDOP (light blue), SQOP (green) and SOOP (purple) nuclei under two different angles of view, derived from the SP map in figure 4.4.

The multipole analysis seems thus able to differentiate the response of a cube from that of a point source. The fact that SDOP, SQOP and SOOP nuclei are developed also for the single point charge model must be interpreted as the consequence of how the corresponding η-functions operate and the degree of equivalence of the responses due to

different source patterns. In other words, the multipole source geometry in figure 4.6 is likely to represent the most probable polyhedral figure generating an SP response equivalent to that drawn in figure 4.1. The parameters of the SPOP, SDOP, SQOP and SOOP nuclei are listed in table 4.2 appendix f.

4.4.3 The rotated and tilted cube model

We show now what happens when the sides of the cube are no longer parallel to the reference coordinate axes. A new model is thus analysed by rotating the cube previously dealt with by 45° around both the vertical *z*-axis and the *y*-axis through the centre. Figure 4.7 shows the SP map of this new source body configuration.
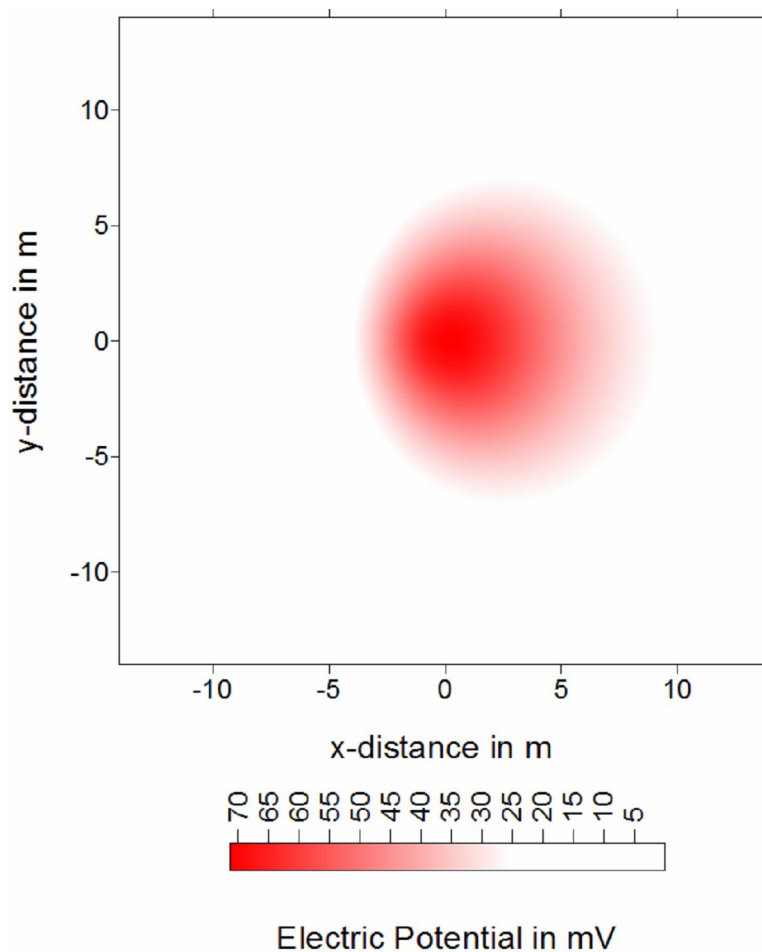

Figure 4.7 The SP map for the tilted cube model with same parameters as in figure 4.1, rotated by 45° around the vertical and horizontal axes through the centre.

Figure 4.8 illustrates the results from the application of the multipole tomography imaging. The SPOP image still shows a nucleus located around the centre. On the contrary, the SDOP, SQOP and SOOP nuclei exhibit a mixed behaviour compared with that of the coaxial cube model.
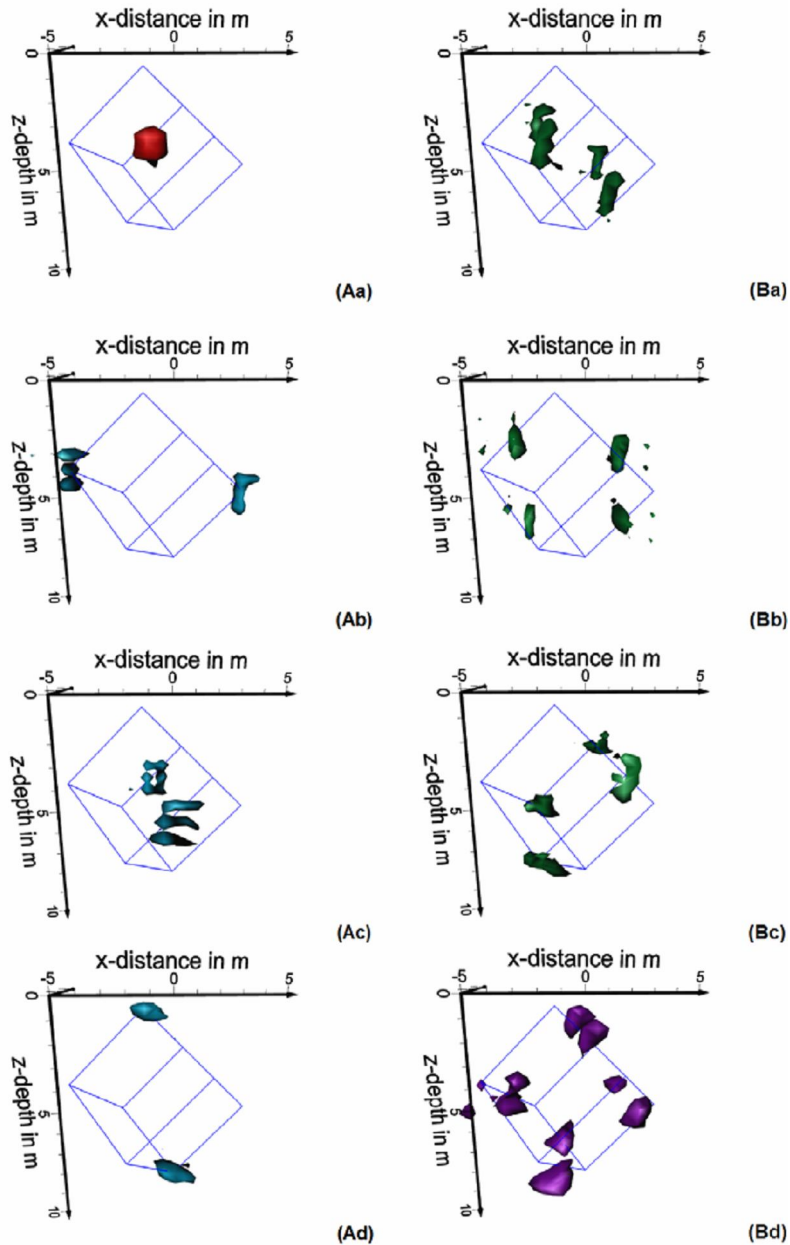

Figure 4.8 The SPOP (Aa), *x*-SDOP (Ab), *y*-SDOP (Ac), *z*-SDOP (Ad), *xy*-SQOP (Ba), *xz*-SQOP (Bb), *yz*-SQOP (Bc) and *xyz*-SOOP (Bd) tomographies derived from the SP synthetic map drawn in figure 4.7. The body with light blue lines is the inclined cube model.

While in the former case they distinctly represent the faces, corners and vertices of the cube, respectively, now the same multiplets can simulate any of these geometrical features, indistinctly. The only regularity is that the nuclei are always revealed in homologous pairs. However, it must be stressed that this behaviour is not casual, since the procedure simply implies the search for the MAV points of the first, second and third order crossed derivatives of the kernel function with respect to the reference axes.
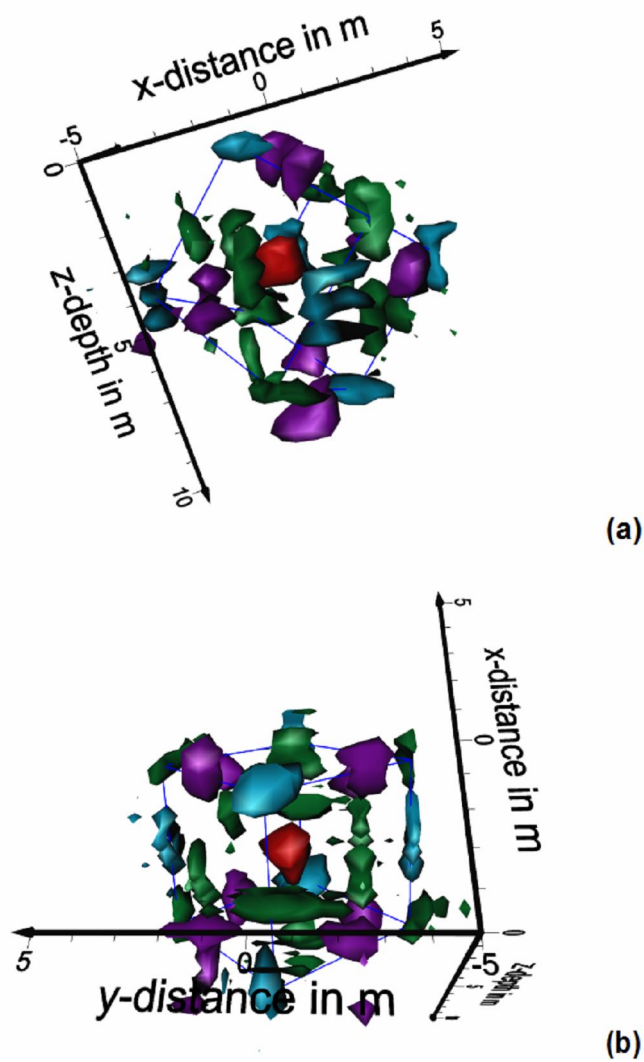

Figure 4.9 A joint representation of the SPOP (red), SDOP (light blue), SQOP (green) and SOOP (purple) nuclei, under two different angles of view, useful to retrieve the source body of the SP map in figure 4.6.

4.4.4 The two prism model

The forth example is the coaxial two-prism model, whose aim is to test the resolution power of the new tomography method. The first prism is a cube with $\Delta\sigma \cong 5.787 \cdot 10^{-4}\,C/m^2$ and the second one is a parallelepiped $\Delta\sigma \cong -4.822 \cdot 10^{-4}\,C/m^2$.

Three cases are shown with three different distances between the centres of the two prisms. Position and side lengths of the two bodies are detailed in the caption of figure 4.10.
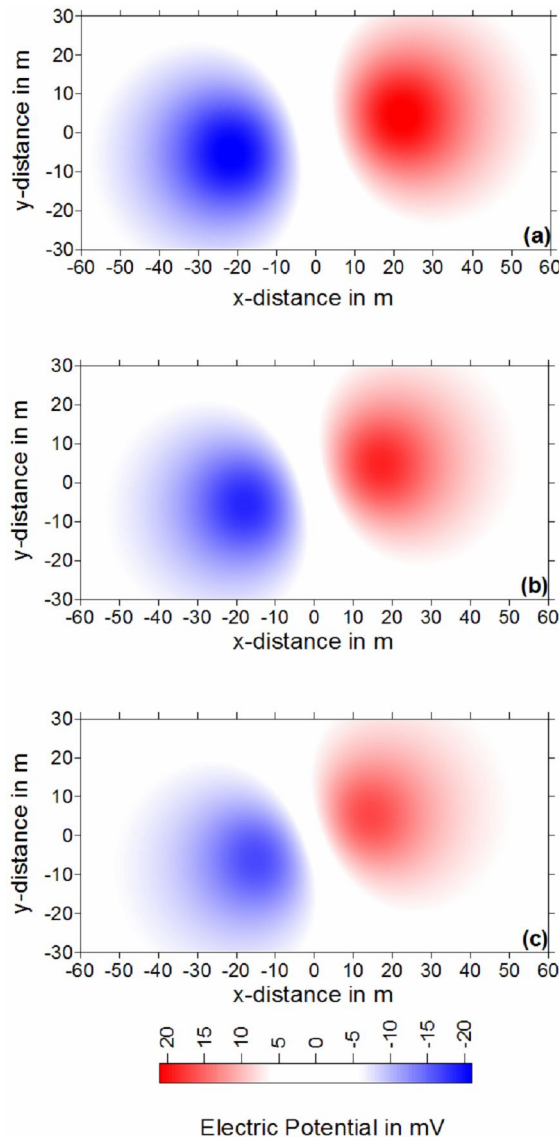

Figure 4.10 The SP map for the two-prism model made of: 1) a cube with $\Delta\sigma \cong 5.787 \cdot 10^{-4}\,C/m^2$, sides parallel to the three coordinate axes and 12 m long each, and centre at *x*=20 m (a), *x*=14.5 m (b) and *x*=11 m (c), *y*=4 m, *z*=15 m; 2) a parallelepiped with $\Delta\sigma \cong -4.822 \cdot 10^{-4}\,C/m^2$, *x*- and *z*-oriented sides 13 m long and *y*-oriented sides 13.5 m long, and centre at *x*=−20 m (a), *x*=−15 m (b) and *x*=−11.5 m (c), *y*=−4.75 m, *z*=15 m.

The SP datasets have been computed at the nodes of a square grid by a 1 m long step in the rectangle [−60,60]×[−30,30] m^2.

Figure 4.10 shows the SP maps for the three cases in order of decreasing distance between the centres from the top (a) to the bottom plot (b).
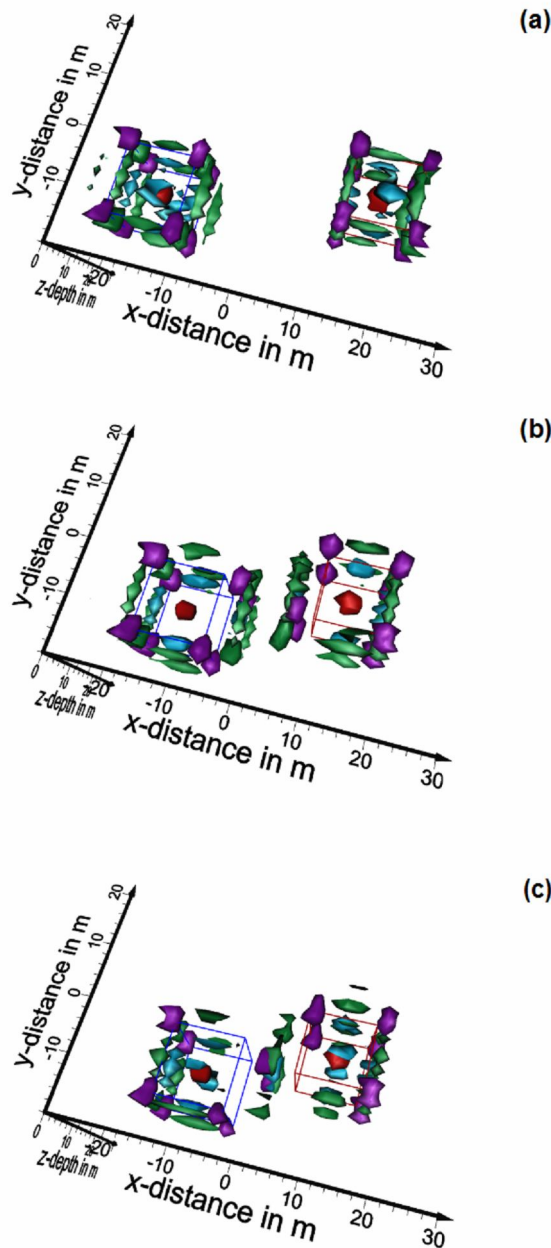

Figure 4.11 A joint representation of the SPOP (red), SDOP (light blue), SQOP (green) and SOOP (purple) nuclei for the two-prism model with decreasing distance between the centres of the two prisms. The sequence of the images is the same as that of the SP maps in figure 4.10.

It is quite evident that the decreasing distance is the cause of an increasing compression of the SP contour lines in the region of highest mutual interference. Figure 4.11 displays the tomography results for the three cases, where, for brevity only the combined multipole images are reported.

In the top one, which refers to a distance between the centres greater than 3 times the average side length of the bodies, the interaction between the two prisms is rather negligible and their true shape can still be recognised. In the middle image, which refers to a distance between the centres of about 2,5 times the average side length, all of the facing SDOP, SQOP and SOOP nuclei depart from their initial places to converge to the centre of the two bodies' system. Finally, in the bottom picture, which refers to a distance a little greater than 2 times the average side length, the detached facing nuclei of same type are wholly melted midway between the prisms. The facing faces, corners and vertices of the two nearby bodies have therefore completely lacked resolution.

4.5   A field example

As is well documented, in natural hydrothermal systems SP signals are generated mainly by electrokinetic flows. Generally speaking, in active volcanic areas, SP positive anomalies correspond to upward migrating fluids, while negative ones to a downward fluid movement [32,46]. We illustrate now the application of the SP 3D multipole probability tomography to an SP survey carried in the volcanic area of Mt. Somma-Vesuvius (Naples, Italy), which aimed to configure the main plumbing system of the volcanic complex. Mt. Somma-Vesuvius is a polygenic strato-volcano, whose most recent period of history (1631-1944) was characterized by a semipersistent, relatively mild activity (lava fountains, gases and vapour emission from the crater), frequently interrupted by short quiet periods that never exceeded seven years. From 1944 to the present time, Mt. Somma-Vesuvius has remained quiet. The SP data were collected in 1995 by the gradient technique with a 100 m long passive dipole, continuously displaced along a wide net of randomly distributed circuits within an area of about 144 km^2 [13], sketched in figure 4.12. Figure 4.13 shows the behaviour of the SP field in mV, resulting from the processing of 1250 measurements [13,19].
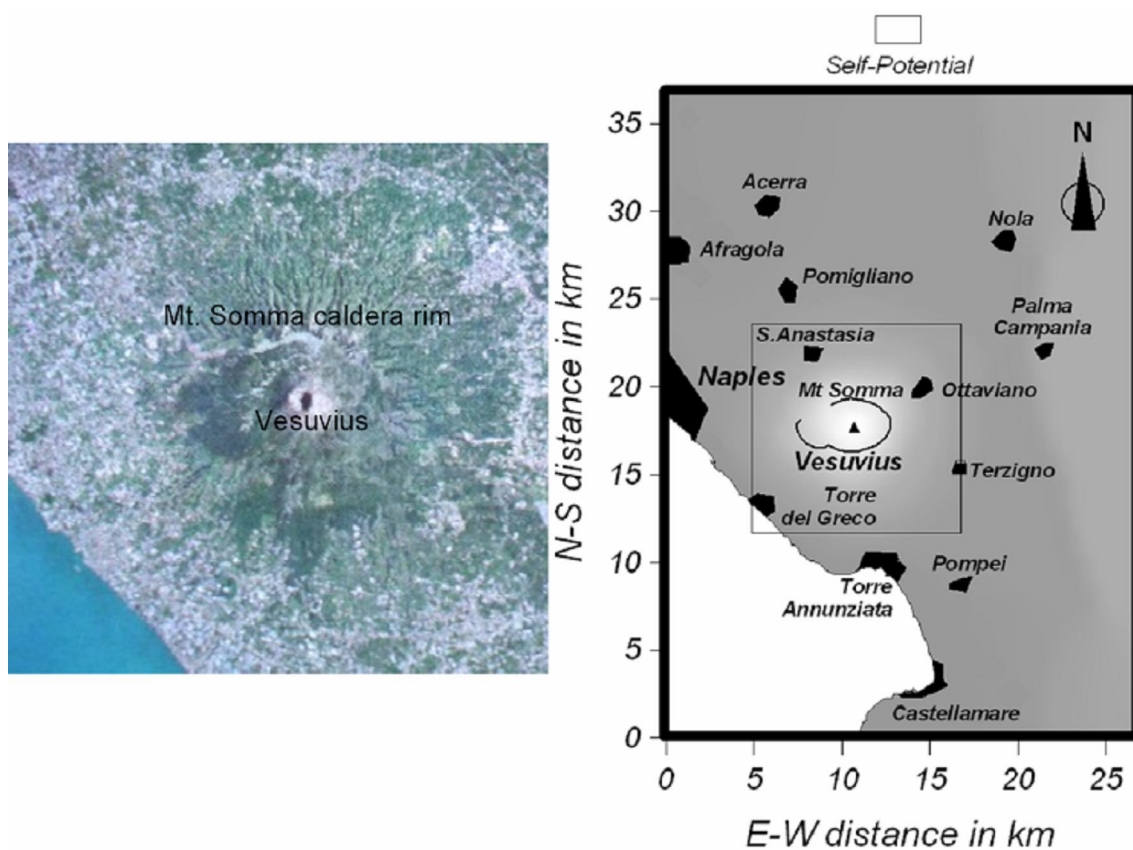
Figure 4.12 The Mt. Somma-Vesuvius survey area.

As the area is characterized by a strongly uneven topography, the 3D multipole tomography algorithm with topographic effects has been used. The SP map in figure 4.13 was already elaborated by the probability tomography method, limitedly, however, only to the source pole and dipole analysis [13,19,32].

The SPOP image in figure 4.14 displays a pair of nuclei of opposite sign containing two poles with the highest occurrence probability. They are interpreted as the centres of the polarised bodies responsible of the SP biggest anomalies of opposite sign drawn in figure 4.13. The negative pole appears to correspond closely to the Mt. Somma caldera rim, while the positive pole closely corresponds to the summit portion of the Vesuvius chimney.
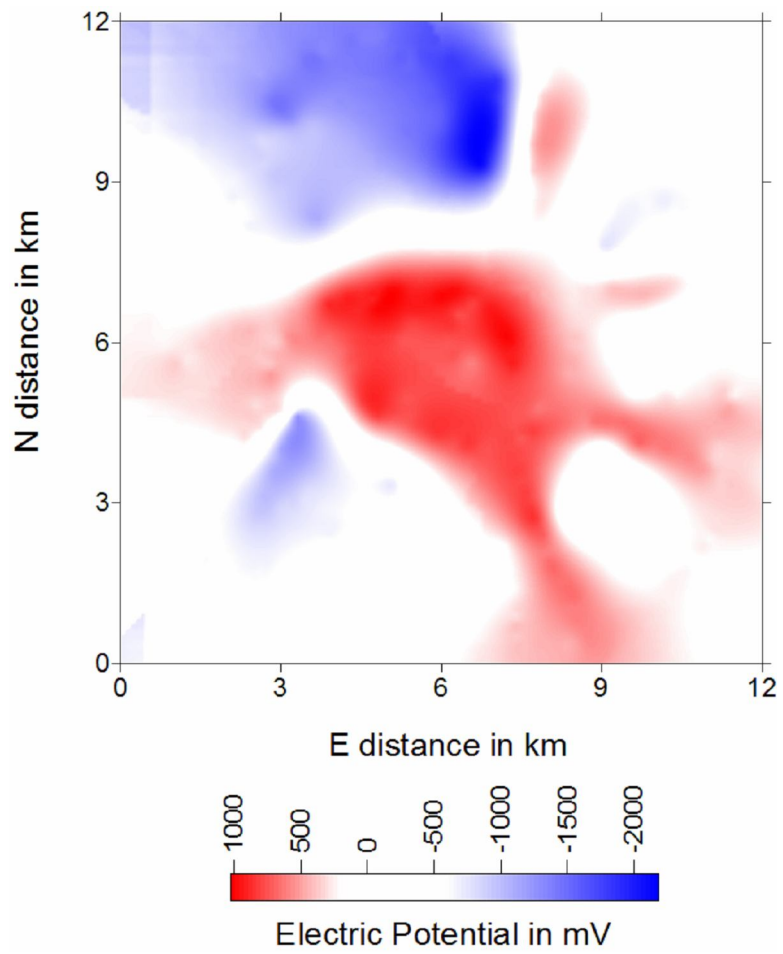
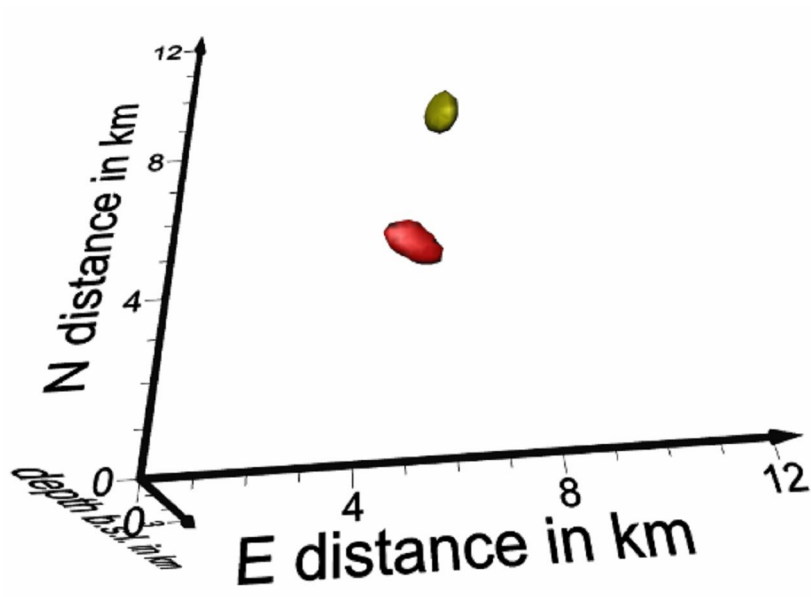**Figure 4.13** The Mt. Somma-Vesuvius SP map.

Figure 4.14 The Mt. Somma-Vesuvius 3D SPOP tomography of the SP map reported in figure 4.13.

Combining in pairs and altogether the SPOP, SDOP, SQOP and SOOP nuclei into single plots, the images in figure 4.15 are obtained [4].
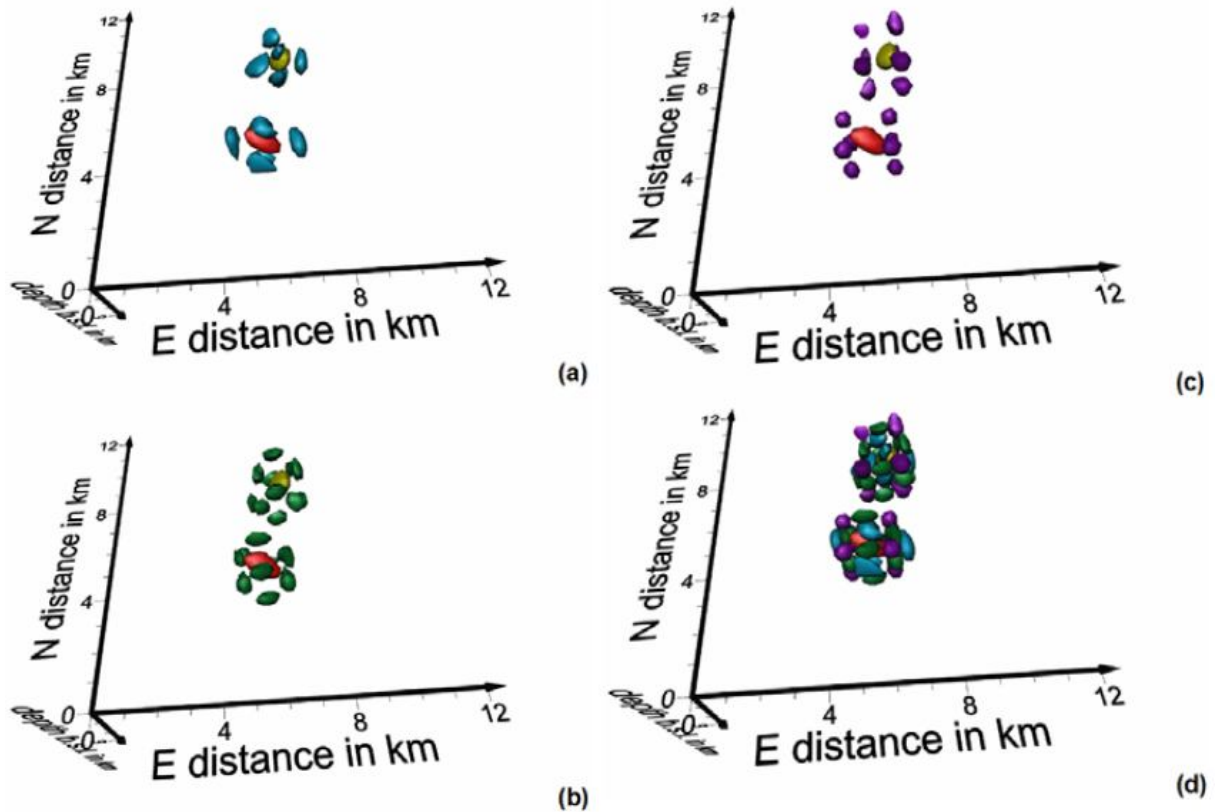

Figure 4.15 A joint representation of the SPOP and SDOP (a), SPOP and SQOP (b), SPOP and SOOP (c), SPOP, SDOP, SQOP and SOOP (d) nuclei, resulting from the application of the 3D multipole tomography method to the Mt. Somma-Vesuvius SP map in figure 4.13.

Figure 4.15 shows a quite regular assemblage of the SDOP, SQOP and SOOP multiplets. All the related nuclei appear clustered around the two poles of figure 4.13, tending to configure two distinct blocks.

Compared with the results from the previous two-prism model, we can state that the two blocks are so sufficiently distant from each other as to exclude any interaction between them, as in the example (a) in figure 4.11. The parameters of the SPOP, SDOP, SQOP and SOOP nuclei in figure 4.15 are listed in table 4.3 appendix f, from which the source bodies are estimated to be confined within the first 3 km of depth b.s.l.. The geometry of the source bodies responsible of the anomalies in figure 4.13 appears now

much better delineated than in the former study where only the SPOP and SDOP algorithms were used [32].

In conclusion, the SP field in the Mt. Somma-Vesuvius volcanic area can be thought of as the response of a gas-dominated hydrothermal engine made of a single large convective circuit. The charging branch, where the cold meteoric waters are channelled into the subsoil, is located in the area of the Mt. Somma caldera rim, and the discharging branch, where the hot uprising fluids flow out in the air, closely corresponds with the Vesuvius central crater where a vast fumaroles front is almost permanently active.

Conclusion

The main result of this thesis has been the development of the theory of the generalized 3D probability tomography method (3D GPT) to image source poles, dipoles, quadrupoles and octopoles, of a geophysical vector or scalar field dataset.

The theoretical derivation of the source quadrupole occurrence probability tomography (SQOP) and source octopole occurrence probability tomography (SOOP) has been given following a formal development similar to those of the source pole occurrence probability tomography (SPOP) and source dipole occurrence probability tomography (SDOP), previously published in detail for single geophysical methods, using an abstract formalism which makes no reference to any particular geophysical prospecting method.

These elementary sources have been used to image, in the most complete way and without any a priori assumption, shape and position of the most probable anomaly source bodies, by picking out the location of the centres and of peculiar points of the boundaries, such as corners, wedges and vertices. In this new formulation, poles and dipoles still have the original meaning to represent centres and boundaries, respectively, of elementary bodies with constant constitutive parameters, while quadrupoles and octopoles are assumed to simulate sharp corners, wedges and vertices elements. The purpose of the multipole analysis has been improving the resolution power of geophysical methods, using probability as a suitable paradigm allowing all possible equivalent solutions to be included into a unique 3D tomography image.

Then, the 3D GPT has been adapted to the geoelectrical, gravity and self potential methods. The multipole sources have been used to detect the position of the centres of the true sources and to highlight the features of their boundaries. A few tests on simple synthetic models and the analysis of three field examples have been documented, in

order to evaluate both feasibility and fidelity of the new approach to geophysical modelling.

The simple synthetic examples have shown the notably enhanced resolution power of the new approach and how the combined pole, dipole, quadrupole and octopole tomographies can provide a complete resolution of the most probable buried sources of the anomalies detected within a datum domain.

We have shown that the 3D multipole GPT method can be successfully applied to a field example related to a dipole–dipole geoelectrical survey carried out in the archaeological park of Pompei to recognize remains of the ancient Roman urban network including roads, squares and buildings, which were buried under the thick pyroclastic cover fallen during the 79 AD Vesuvius eruption.

The relative SQOP tomography has allowed a prismatic shape with vertical edges, associated with some aligned, elongated resistive bodies with sharp lateral bounds, disclosed by a previous SPOP and SDOP analysis, to be definitely ascribed to well-preserved remnants of some aligned walls of Roman edifices, buried and partially destroyed by the 79 AD Vesuvius pyroclastic fall.

We have applied, also, the theory of the probability tomography for the gravity method to a gravity survey carried out in the volcanic area of Mt. Etna (Sicily, Italy) to delineate the geometry of the Bouguer anomaly sources in the central volcanic area.

In conclusion, an assemblage of vertical prismatic blocks has appeared to be the most probable gravity model of the Etna apparatus within the first 5 km of depth below sea level.

Finally , an experimental SP dataset collected in the Mt. Somma-Vesuvius volcanic district (Naples, Italy) has been elaborated with the new theory in order to define location and shape of the sources of two SP anomalies of opposite sign detected in the northwestern sector of the surveyed area. The modelled sources have been interpreted as the polarization state induced by an intense hydrothermal convective flow mechanism within the volcanic apparatus, from the free surface down to about 3 km of depth b.s.l..

The probabilistic approach has mainly been efficient to solve the problems developed in this thesis. In fact all the geophysical methods are based on incomplete cognitive processes due to not comparable measurements, difficulties to have data sets enough thick and noise presence. Moreover the probabilistic approach has proved to fit well

with the imaging of the geophysical field interaction with the structures inside the investigated medium, without any constrain or a priori model assumption.

One of the possible developments of this thesis work will be the 3D GPT evolution towards a true inversion process in order to obtain at the same time information on the position, on the geometry and on the intensity of the sources of any geophysical anomaly.

To conclude, it is worth emphasising the role of the 3D multipole geophysical probability tomography approach in the definition of the sources of the SP anomalies which are observed on the ground surface in many application fields, among which volcanology, as in this study, seismology and archaeology. It is also worth stressing the importance that the probability tomography can have in the study of the time evolution of the SP signals in high-risk volcanic areas, where the electrokinetic source field may undergo a rapid increase of intensity in conjunction with an increase of the volcanic emission activity. The 4D tomography is in fact becoming a very promising monitoring technique especially in fast flow visualization.

Appendix A

The DD apparent resistivity $\rho_a(i,j,k)$ is defined as

$$\rho_a(i,j,k) = \frac{K}{I_{AB}} \Delta\phi_{MN} \tag{A1}$$

where I_{AB} is the intensity of the primary current injected into the ground through the current electrodes A and B, K is the well known DD geometrical factor given by

$$K = \pi a k(k+1)(k+2) \tag{A2}$$

with a being both the spread of the dipoles and the spacing between adjacent profiles (in the Pompei case it is $a=2$ m), and $\Delta\phi_{MN}$ is the potential difference across the electrodes M and N. Referring to figure 2.8, $\Delta\phi_{MN}$ is expanded as

$$\Delta\phi_{MN} = \phi(i,j,i+k) - \phi(i-1,j,i+k) - \phi(i,j,i+k+1) + \phi(i-1,j,i+k+1) \tag{A3}$$

hence it follows

$$\frac{\partial\rho_{a,0}(i,j,k)}{\partial\rho_m} = \frac{K}{I_{AB}} \frac{\partial}{\partial\rho_m} \big[\phi(i,j,i+k) - \phi(i-1,j,i+k)$$
$$- \phi(i,j,i+k+1) + \phi(i-1,j,i+k+1)\big] \tag{A4}$$

The four Frechet derivatives are taken from Mauriello and Patella [26] as follows

$$\frac{\partial\phi(i,j,i+k)}{\partial\rho_m} = \frac{I_{AB}\Delta V}{4\pi^2}$$
$$\cdot \frac{[x_m - ia][x_m - (i+k)a] + [y_m - ja]^2 + z_m^2}{\{[x_m - ia]^2 + [y_m - ja]^2 + z_m^2\}^{3/2} \{[x_m - (i+k)a]^2 + [y_m - ja]^2 + z_m^2\}^{3/2}} \tag{A5}$$

$$\frac{\partial \phi(i-1,j,i+k)}{\partial \rho_m} = \frac{I_{AB}\Delta V}{4\pi^2}$$

$$\cdot \frac{[x_m-(i-1)a][x_m-(i+k)a]+[y_m-ja]^2+z_m^2}{\left\{[x_m-(i-1)a]^2+[y_m-ja]^2+z_m^2\right\}^{3/2}\left\{[x_m-(i+k)a]^2+[y_m-ja]^2+z_m^2\right\}^{3/2}} \qquad (A6)$$

$$\frac{\partial \phi(i,j,i+k+1)}{\partial \rho_m} = \frac{I_{AB}\Delta V}{4\pi^2}$$

$$\cdot \frac{[x_m-ia][x_m-(i+k+1)a]+[y_m-ja]^2+z_m^2}{\left\{[x_m-ia]^2+[y_m-ja]^2+z_m^2\right\}^{3/2}\left\{[x_m-(i+k+1)a]^2+[y_m-ja]^2+z_m^2\right\}^{3/2}} \qquad (A7)$$

$$\frac{\partial \phi(i-1,j,i+k+1)}{\partial \rho_m} = \frac{I_{AB}\Delta V}{4\pi^2}$$

$$\cdot \frac{[x_m-(i-1)a][x_m-(i+k+1)a]+[y_m-ja]^2+z_m^2}{\left\{[x_m-(i-1)a]^2+[y_m-ja]^2+z_m^2\right\}^{3/2}\left\{[x_m-(i+k+1)a]^2+[y_m-ja]^2+z_m^2\right\}^{3/2}} \qquad (A8)$$

Appendix B

pole		dipole x-component		dipole y-component		dipole z-component		quadrupole xy-element	
MAV	%	MAV	%	MAV	%	MAV	%	MAV	%
0,655	95	$\|\pm0.473\|$	95	$\|\pm0.476\|$	95	$\|-0.673\|$	95	$\|\pm0.247\|$	95

quadrupole xx-element		quadrupole yy-element		quadrupole zz-element		quadrupole xz-element		quadrupole yz-element	
MAV	%	MAV	%	MAV	%	MAV	%	MAV	%
0.219 $\|-0.422\|$	95	0.262 $\|-0.436\|$	95	0.680	95	$\|\pm0.473\|$	95	$\|\pm0.479\|$	95

Table 2.1 SPOP, SDOP and SQOP primary maximum absolute values (MAV) and corresponding reduced levels in per cent (%), considered for the tracing of the isosurfaces bounding the nuclei in figure 2.4(a).

	Figure 2.4 (b)			Figure 2.5			Figure 2.6			Figure 2.7		
	MAV	% (a)	% (b)	MAV	% (a)	% (b)	MAV	% (a)	% (b)	MAV	% (a)	% (b)
pole	0.655	95	95	0.531	95	95	0.375	85	85	0.545	95	50
dipole x-component	$\|\pm0.473\|$	95	50	$\|\pm0.286\|$	95	50	0.310 $\|-0.268\|$	85	60	0.346 $\|-0.342\|$	95	40
dipole y-component	$\|\pm0.476\|$	95	50	$\|\pm0.390\|$	95	50	0.274 $\|-0.270\|$	85	60	0.413 $\|-0.398\|$	95	20
quadrupole xy-element	$\|\pm0.247\|$	95	50	$\|\pm0.196\|$	95	20	0.210 $\|-0.204\|$	85	60	0.445 $\|-0.447\|$	85	15

Table 2.2 SPOP, SDOP and SQOP primary maximum absolute values (MAV) and corresponding reduced levels in per cent (%), considered for the tracing of the isosurfaces bounding the nuclei appearing in figures 2.4(b), 2.5–2.7.

pole		dipole x-component		dipole y-component		dipole z-component		quadrupole xy-element	
MAV	%	MAV	%	MAV	%	MAV	%	MAV	%
0.241	30	0.147	50	0.086	50	0.222	75	0.152	30
$|-0.216|$	75	$|-0.131|$	50	$|-0.156|$	50	$|-0.176|$	50	$|-0.148|$	30

Table 2.3 SPOP, SDOP and SQOP primary maximum absolute values (MAV) and corresponding reduced levels in per cent (%), considered for the tracing of the isosurfaces bounding the nuclei appearing in figure 2.17.

Appendix C

$$s(\mathbf{r}, \mathbf{r}_m) = \frac{z_m - z}{\left[(x_m - x)^2 + (y_m - y)^2 + (z_m - z)^2\right]^{3/2}} \tag{C1}$$

$$\frac{\partial s(\mathbf{r}, \mathbf{r}_n)}{\partial x_n} = \frac{3(z_n - z)(x_n - x)}{\left[(x_n - x)^2 + (y_n - y)^2 + (z_n - z)^2\right]^{5/2}} \tag{C2}$$

$$\frac{\partial s(\mathbf{r}, \mathbf{r}_n)}{\partial y_n} = \frac{3(z_n - z)(y_n - y)}{\left[(x_n - x)^2 + (y_n - y)^2 + (z_n - z)^2\right]^{5/2}} \tag{C3}$$

$$\frac{\partial s(\mathbf{r},\mathbf{r}_n)}{\partial z_n} = \frac{(x_n - x)^2 + (y_n - y)^2 - 2(z_n - z)^2}{\left[(x_n - x)^2 + (y_n - y)^2 + (z_n - z)^2\right]^{5/2}} \tag{C4}$$

$$\frac{\partial^2 s(\mathbf{r},\mathbf{r}_g)}{\partial x_g \partial y_g} = \frac{15(x_g - x)(y_g - y)(z_g - z)}{\left[(x_g - x)^2 + (y_g - y)^2 + (z_g - z)^2\right]^{7/2}} \tag{C5}$$

$$\frac{\partial^2 s(\mathbf{r},\mathbf{r}_g)}{\partial x_g \partial z_g} = \frac{-3(x_g - x)\left[(x_g - x)^2 + (y_g - y)^2 - 4(z_g - z)^2\right]}{\left[(x_g - x)^2 + (y_g - y)^2 + (z_g - z)^2\right]^{7/2}} \tag{C6}$$

$$\frac{\partial^2 s(\mathbf{r},\mathbf{r}_g)}{\partial y_g \partial z_g} = \frac{-3(y_g - y)\left[(x_g - x)^2 + (y_g - y)^2 - 4(z_g - z)^2\right]}{\left[(x_g - x)^2 + (y_g - y)^2 + (z_g - z)^2\right]^{7/2}} \tag{C7}$$

$$\frac{\partial^3 s(\mathbf{r},\mathbf{r}_h)}{\partial x_h \partial y_h \partial z_h} = \frac{15(x_h - x)(y_h - y)\left[(x_h - x)^2 + (y_h - y)^2 - 6(z_h - z)^2\right]}{\left[(x_h - x)^2 + (y_h - y)^2 + (z_h - z)^2\right]^{9/2}} \tag{C8}$$

Appendix D

A	B	C	D
SPOP (+)	$\eta_m^{(p)}$ =0.950	$\left.\left|\eta_m^{(p)}\right|\right._{max}$ =0.952	(0.0, 0.0, 5.9)
x-SDOP (+)	$\eta_{n,x}^{(d)}$ =0.450	$\left.\left|\eta_{n,x}^{(d)}\right|\right._{max}$ =0.491	(-3.1, 0.1, 6.0)
x-SDOP (−)	$\eta_{n,x}^{(d)}$ =−0.440	$\left.\left|\eta_{n,x}^{(d)}\right|\right._{max}$ =0.467	(3.1, 0.0, 6.0)
y-SDOP (+)	$\eta_{n,y}^{(d)}$ =0.460	$\left.\left|\eta_{n,y}^{(d)}\right|\right._{max}$ =0.494	(-0.1, -3.0, 6.0)
y-SDOP (−)	$\eta_{n,y}^{(d)}$ =−0.440	$\left.\left|\eta_{n,y}^{(d)}\right|\right._{max}$ =0.467	(-0.1, 3.0, 6.0)
z-SDOP (+)	$\eta_{n,z}^{(d)}$ =0.450	$\left.\left|\eta_{n,z}^{(d)}\right|\right._{max}$ =0.481	(0.0, 0.1, 3.0)
z-SDOP (−)	$\eta_{n,z}^{(d)}$ =−0.450	$\left.\left|\eta_{n,z}^{(d)}\right|\right._{max}$ =0.484	(0.0, 0.0, 9.0)
xy-SQOP (+)	$\eta_{g,xy}^{(q)}$ =0.280	$\left.\left|\eta_{g,xy}^{(q)}\right|\right._{max}$ =0.297	(3.0, 3.0, 5.9) (-3.0, -3.0, 5.9)
xy-SQOP (−)	$\eta_{g,xy}^{(q)}$ =−0.280	$\left.\left|\eta_{g,xy}^{(q)}\right|\right._{max}$ =0.297	(3.1, -3.0, 6.0) (-3.0, 3.0, 6.0)
xz-SQOP (+)	$\eta_{g,xz}^{(q)}$ =0.240	$\left.\left|\eta_{g,xz}^{(q)}\right|\right._{max}$ =0.289	(-3.3, 0.0 3.1) (3.3, 0.0, 9.0)
xz-SQOP (−)	$\eta_{g,xz}^{(q)}$ =−0.240	$\left.\left|\eta_{g,xz}^{(q)}\right|\right._{max}$ =0.284	(3.3, 0.0, 3.1) (-3.3, 0.0, 9.0)
yz-SQOP (+)	$\eta_{g,yz}^{(q)}$ =0.240	$\left.\left|\eta_{g,yz}^{(q)}\right|\right._{max}$ =0.289	(0.0, -3.2, 3.1) (0.0, 3.3 9.0)
yz-SQOP (−)	$\eta_{g,yz}^{(q)}$ =−0.240	$\left.\left|\eta_{g,yz}^{(q)}\right|\right._{max}$ =0.284	(0.0, 3.2, 3.1) (0.0, -3.2, 9.0)
xyz-SQOP (+)	$\eta_{h,xyz}^{(o)}$ =0.	$\left.\left|\eta_{h,xyz}^{(o)}\right|\right._{max}$ =0.127	(3.1, 3.1, 3.0) (-3.1, -3.1, 3.0) (3.1, -3.1, 9.0) (-3.1, 3.1, 9.0)
xyz-SQOP (−)	$\eta_{h,xyz}^{(o)}$ =−0.	$\left.\left|\eta_{h,xyz}^{(o)}\right|\right._{max}$ =0.127	(3.1, -3.1, 3.1) (-3.1, 3.1, 3.1) (-3.1, -3.1, 9.1) (3.1, 3.1, 9.0)

Table 3.1 Characterization of the SPOP, SDOP SQOP and SOOP nuclei in figure 3.4. **A**: nucleus type; **B**: bounding isosurface; **C**: maximum absolute value (MAV); **D**: (*x*,*y*,*z*) of the MAV point.

Appendix E

$$\frac{\partial s_\varphi(\mathbf{r},\mathbf{r}_n)}{\partial x_n} = \frac{3(x-x_n)A_{1,n}(x,z)-\left|\mathbf{r}-\mathbf{r}_n\right|^2}{\left|\mathbf{r}-\mathbf{r}_n\right|^5} x'_\varphi \tag{E1}$$

$$\frac{\partial s_\varphi(\mathbf{r},\mathbf{r}_n)}{\partial y_n} = \frac{3(y-y_n)A_{1,n}(x,z)}{\left|\mathbf{r}-\mathbf{r}_n\right|^5} x'_\varphi \tag{E2}$$

$$\frac{\partial s_\varphi(\mathbf{r},\mathbf{r}_n)}{\partial z_n} = \frac{3(z-z_n)A_{1,n}(x,z)-\left|\mathbf{r}-\mathbf{r}_n\right|^2 z'_x}{\left|\mathbf{r}-\mathbf{r}_n\right|^5} x'_\varphi \tag{E3}$$

where $A_{1,n}(x,z)=(x-x_n)+(z-z_n)z'_x$, and

$$\frac{\partial s_\psi(\mathbf{r},\mathbf{r}_n)}{\partial x_n} = \frac{3(x-x_n)B_{1,n}(y,z)}{\left|\mathbf{r}-\mathbf{r}_n\right|^5} y'_\psi \tag{E4}$$

$$\frac{\partial s_\psi(\mathbf{r},\mathbf{r}_n)}{\partial y_n} = \frac{3(y-y_n)B_{1,n}(y,z)-\left|\mathbf{r}-\mathbf{r}_n\right|^2}{\left|\mathbf{r}-\mathbf{r}_n\right|^5} y'_\psi \tag{E5}$$

$$\frac{\partial s_\psi(\mathbf{r},\mathbf{r}_n)}{\partial z_n} = \frac{3(z-z_n)B_{1,n}(y,z)-\left|\mathbf{r}-\mathbf{r}_n\right|^2 z'_y}{\left|\mathbf{r}-\mathbf{r}_n\right|^5} y'_\psi \tag{E6}$$

where $B_{1,n}(y,z)=(y-y_n)+(z-z_n)z'_y$.

$$\frac{\partial^2 s_\varphi(\mathbf{r},\mathbf{r}_g)}{\partial x_g \partial y_g} = \frac{3(y-y_g)\left[5(x-x_g)A_{1,g}(x,z)-\left|\mathbf{r}-\mathbf{r}_g\right|^2\right]}{\left|\mathbf{r}-\mathbf{r}_g\right|^7} x'_\varphi \tag{E7}$$

$$\frac{\partial^2 s_\varphi(\mathbf{r},\mathbf{r}_g)}{\partial x_g \partial z_g} = \frac{15(x-x_g)(z-z_g)A_{1,g}(x,z)-3A_{2,g}(x,z)\left|\mathbf{r}-\mathbf{r}_g\right|^2}{\left|\mathbf{r}-\mathbf{r}_g\right|^7} x'_\varphi \tag{E8}$$

$$\frac{\partial^2 s_\varphi(\mathbf{r},\mathbf{r}_g)}{\partial y_g \partial z_g} = \frac{3(y-y_g)\left[5(z-z_g)A_{1,g}(x,z)-\left|\mathbf{r}-\mathbf{r}_g\right|^2 z'_x\right]}{\left|\mathbf{r}-\mathbf{r}_g\right|^7}x'_\varphi \tag{E9}$$

with $A_{1,g}(x,z)=(x-x_g)+(z-z_g)z'_x$, $A_{2,g}(x,z)=(z-z_g)+(x-x_g)z'_x$, and

$$\frac{\partial^2 s_\psi(\mathbf{r},\mathbf{r}_g)}{\partial x_g \partial y_g} = \frac{3(x-x_g)\left[5(y-y_g)B_{1,g}(y,z)-\left|\mathbf{r}-\mathbf{r}_g\right|^2\right]}{\left|\mathbf{r}-\mathbf{r}_g\right|^7}y'_\psi \tag{E10}$$

$$\frac{\partial^2 s_\psi(\mathbf{r},\mathbf{r}_g)}{\partial x_g \partial z_g} = \frac{3(x-x_g)\left[5(z-z_g)B_{1,g}(y,z)-\left|\mathbf{r}-\mathbf{r}_g\right|^2 z'_y\right]}{\left|\mathbf{r}-\mathbf{r}_g\right|^7}y'_\psi \tag{E11}$$

$$\frac{\partial^2 s_\psi(\mathbf{r},\mathbf{r}_g)}{\partial y_g \partial z_g} = \frac{15(y-y_g)(z-z_g)B_{1,g}(y,z)-3B_{2,g}(y,z)\left|\mathbf{r}-\mathbf{r}_g\right|^2}{\left|\mathbf{r}-\mathbf{r}_g\right|^7}y'_\psi \tag{E12}$$

with $B_{1,g}(x,z)=(y-y_g)+(z-z_g)z'_y$, $B_{2,g}(x,z)=(z-z_g)+(y-y_g)z'_y$.

$$\frac{\partial^3 s_\varphi(\mathbf{r},\mathbf{r}_h)}{\partial x_h \partial y_h \partial z_h} = \frac{15(y-y_h)\left[7(x-x_h)(z-z_h)A_{1,h}(x,z)-A_{2,h}(x,z)\left|\mathbf{r}-\mathbf{r}_h\right|^2\right]}{\left|\mathbf{r}-\mathbf{r}_h\right|^9}x'_\varphi \tag{E13}$$

with $A_{1,h}(x,z)=(x-x_h)+(z-z_h)z'_x$, $A_{2,h}(x,z)=(z-z_h)+(x-x_h)z'_x$, and

$$\frac{\partial^3 s_\psi(\mathbf{r},\mathbf{r}_h)}{\partial x_h \partial y_h \partial z_h} = \frac{15(x-x_h)\left[7(y-y_h)(z-z_h)B_{1,h}(y,z)-B_{2,h}(y,z)\left|\mathbf{r}-\mathbf{r}_h\right|^2\right]}{\left|\mathbf{r}-\mathbf{r}_h\right|^9}y'_\psi \tag{E14}$$

with $B_{1,h}(x,z)=(y-y_h)+(z-z_h)z'_y$, $B_{2,h}(x,z)=(z-z_h)+(y-y_h)z'_y$.

Appendix F

A	B	C	D
SPOP (+)	$\eta_m^{(p)}=0.903$	$\left.\eta_m^{(p)}\right|_{max}=0.904$	(0.1, 0.0, 6.1)
x-SDOP (+)	$\eta_{n,x}^{(d)}=0.375$	$\left.\eta_{n,x}^{(d)}\right|_{max}=0.398$	(-2.9, 0.1, 6.0)
x-SDOP (−)	$\eta_{n,x}^{(d)}=-0.38$	$\left.\eta_{n,x}^{(d)}\right|_{max}=0.408$	(3.0, 0.0, 6.1)
y-SDOP (+)	$\eta_{n,y}^{(d)}=0.375$	$\left.\eta_{n,y}^{(d)}\right|_{max}=0.391$	(-0.2, -3.1, 6.0)
y-SDOP (−)	$\eta_{n,y}^{(d)}=-0.371$	$\left.\eta_{n,y}^{(d)}\right|_{max}=0.395$	(-0.1, 3.1, 6.1)
z-SDOP (+)	$\eta_{n,z}^{(d)}=0.40$	$\left.\eta_{n,z}^{(d)}\right|_{max}=0.445$	(-0.1, 0.1, 3.1)
z-SDOP (−)	$\eta_{n,z}^{(d)}=-0.401$	$\left.\eta_{n,z}^{(d)}\right|_{max}=0.447$	(0.0, 0.1, 9.0)
xy-SQOP (+)	$\eta_{g,xy}^{(q)}=0.252$	$\left.\eta_{g,xy}^{(q)}\right|_{max}=0.258$	(3.0, 3.0, 5.9) (-3.0, -3.1, 5.9)
xy-SQOP (−)	$\eta_{g,xy}^{(q)}=-0.252$	$\left.\eta_{g,xy}^{(q)}\right|_{max}=0.258$	(3.0, -3.0, 6.0) (-3.0, 3.1, 6.1)
xz-SQOP (+)	$\eta_{g,xz}^{(q)}=0.270$	$\left.\eta_{g,xz}^{(q)}\right|_{max}=0.393$	(-3.3, 0.0 3.1) (3.3, 0.0, 9.0)
xz-SQOP (−)	$\eta_{g,xz}^{(q)}=-0.270$	$\left.\eta_{g,xz}^{(q)}\right|_{max}=0.39$	(3.1, 0.2, 3.1) (-3.3, 0.2, 9.0)
yz-SQOP (+)	$\eta_{g,yz}^{(q)}=0.275$	$\left.\eta_{g,yz}^{(q)}\right|_{max}=0.381$	(0.1, -3.2, 3.1) (0.0, 3.4 9.0)
yz-SQOP (−)	$\eta_{g,yz}^{(q)}=-0.275$	$\left.\eta_{g,yz}^{(q)}\right|_{max}=0.381$	(0.0, 3.3, 3.1) (0.1, -3.2, 9.0)
xyz-SQOP (+)	$\eta_{h,xyz}^{(o)}=0.104$	$\left.\eta_{h,xyz}^{(o)}\right|_{max}=0.113$	(3.1, 3.2, 3.1) (-3.1, -3.1, 3.0) (3.2, -3.1, 9.1) (-3.1, 3.0, 9.0)
xyz-SQOP (−)	$\eta_{h,xyz}^{(o)}=-0.105$	$\left.\eta_{h,xyz}^{(o)}\right|_{max}=0.114$	(3.2, -3.1, 3.1) (-3.1, 3.1, 3.1) (-3.1, -3.1, 9.1) (3.2, 3.1, 9.1)

Table 4.1. Characterization of the SPOP,SDOP,SQOP and SOOP nuclei in figure 4.2. **A**: nucleus type; **B**: bounding isosurface; **C**: Maximum absolute value (MAV); **D**: (x,y,z) of the MAV point.

A	B	C	D
SPOP (+)	$\eta_m^{(p)}=0.885$	$\left.\left\|\eta_m^{(p)}\right\|\right\|_{max}=0.886$	(0.0, 0.0, 6.0)
x-SDOP (+)	$\eta_{n,x}^{(d)}=0.143$	$\left.\left\|\eta_{n,x}^{(d)}\right\|\right\|_{max}=0.151$	(-3.6, -0.2, 6.0)
x-SDOP (−)	$\eta_{n,x}^{(d)}=-0.143$	$\left.\left\|\eta_{n,x}^{(d)}\right\|\right\|_{max}=0.152$	(3.5, 0.0, 6.0)
y-SDOP (+)	$\eta_{n,y}^{(d)}=0.143$	$\left.\left\|\eta_{n,y}^{(d)}\right\|\right\|_{max}=0.152$	(-0.1, -3.7, 6.0)
y-SDOP (−)	$\eta_{n,y}^{(d)}=-0.143$	$\left.\left\|\eta_{n,y}^{(d)}\right\|\right\|_{max}=0.153$	(0.0, 3.6, 6.1)
z-SDOP (+)	$\eta_{n,z}^{(d)}=0.161$	$\left.\left\|\eta_{n,z}^{(d)}\right\|\right\|_{max}=0.171$	(0.1, -0.3, 2.3)
z-SDOP (−)	$\eta_{n,z}^{(d)}=-0.161$	$\left.\left\|\eta_{n,z}^{(d)}\right\|\right\|_{max}=0.183$	(0.1, -0.3, 10.0)
xy-SQOP (+)	$\eta_{g,xy}^{(q)}=0.099$	$\left.\left\|\eta_{g,xy}^{(q)}\right\|\right\|_{max}\leq0.102$	(2.8, 2.8, 6.2) (-2.7, -2.8, 6.1)
xy-SQOP (−)	$\eta_{g,xy}^{(q)}=-0.099$	$\left.\left\|\eta_{g,xy}^{(q)}\right\|\right\|_{max}\leq0.102$	(2.8, -2.7, 6.1) (-2.8, 2.8, 6.1)
xz-SQOP (+)	$\eta_{g,xz}^{(q)}=0.094$	$\left.\left\|\eta_{g,xz}^{(q)}\right\|\right\|_{max}\leq0.126$	(-2.8, -0.2, 4.3) (3.3, -0.1, 7.3)
xz-SQOP (−)	$\eta_{g,xz}^{(q)}=-0.094$	$\left.\left\|\eta_{g,xz}^{(q)}\right\|\right\|_{max}\leq0.126$	(2.8, -0.2, 4.3) (-3.4, -0.1, 7.3)
yz-SQOP (+)	$\eta_{g,yz}^{(q)}=0.094$	$\left.\left\|\eta_{g,yz}^{(q)}\right\|\right\|_{max}\leq0.122$	(-0.2, -2.7, 4.4) (-0.1, 3.2, 7.3)
yz-SQOP (−)	$\eta_{g,yz}^{(q)}=-0.094$	$\left.\left\|\eta_{g,yz}^{(q)}\right\|\right\|_{max}\leq0.122$	(-0.2, 2.6, 4.5) (-0.1, -3.3, 7.3)
xyz-SQOP (+)	$\eta_{h,xyz}^{(o)}=0.046$	$\left.\left\|\eta_{h,xyz}^{(o)}\right\|\right\|_{max}=0.053$	(3.0, 3.2, 4.5) (-3.1, -3.1 4.4) (3.9, -3.8, 7.6) (-3.8, 3.7, 7.5)
xyz-SQOP (−)	$\eta_{h,xyz}^{(o)}=-0.046$	$\left.\left\|\eta_{h,xyz}^{(o)}\right\|\right\|_{max}=0.053$	(3.1, -3.2, 4.4) (-3.1, 3.2, 4.4) (-3.8, -3.7, 7.5) (3.8, 3.8, 7.5)

Table 4.2. Characterization of the SPOP,SDOP,SQOP and SOOP nuclei in figure 4.5. **A**: nucleus type; **B**: bounding isosurface; **C**: Maximum absolute value (MAV); **D**: (x,y,z) of the MAV point.

Anomaly	SPOP (+)	SPOP (-)
SPOP	(5.4, 6.3, 1.5)	(6.5, 9.9, 0.9)
x-SDOP (+)	(4.3, 6.2, 1.6)	(7.3, 10.0,1.0)
x-SDOP (−)	(6.9, 6.2, 1.6)	(5.4, 9.8, 1.0)
y-SDOP (+)	(5.3, 5.4, 1.8)	(6.3, 11.6, 1.0)
y-SDOP (−)	(5.3, 7.0, 1.7)	(6.4, 9.0, 0.9)
z-SDOP (+)	(5.5, 6.3, 0.9)	(6.4, 9.9, 1.9)
z-SDOP (−)	(5.5, 6.3, 2.7)	(6.5, 9.9, 0.4)
xy-SQOP (+)	(4.6, 5.5, 1.8) (6.5, 6.9, 1.8)	(5.5, 9.0, 1.2) (7.1, 11.5, 1.3)
xy-SQOP (−)	(4.6, 6.9, 1.8) (6.6, 5.5, 1.8)	(5.5, 11.3, 1.2) (7.1, 9.0, 1.3)
xz-SQOP (+)	(4.5, 6.0, 0.9) (6.5, 6.1, 2.7)	(5.4, 9.7, 0.2) (7.4, 10.2, 2.1)
xz-SQOP (−)	(6.5, 6.0, 0.8) (4.6, 6.1, 2.7)	(7.2, 9.9, 0.2) (5.2, 10.2, 2.2)
yz-SQOP (+)	(5.4, 5.2, 0.7) (5.4, 7.2, 2.6)	(6.3, 9.0, 0.3) (6.2, 11.6, 2.1)
yz-SQOP (−)	(5.2, 7.1, 0.7) (5.4, 5.2, 2.6)	(6.3, 11.3, 0.2) (6.3, 9.1, 2.1)
xyz-SQOP (+)	(4.5, 6.8, 0.7) (6.3, 5.3, 0.7) (4.7, 5.6, 2.7) (6.4, 7.0, 2.7)	(5.4, 8.8, 0.3) (6.9, 11.0, 0.2) (5.5, 11.2, 1.9) (7.0, 9.3, 2.0)
xyz-SQOP (−)	(4.6, 5.3, 0.7) (6.3, 5.6, 0.7) (4.7, 7.1, 2.7) (6.4, 6.8, 2.7)	(5.4, 10.8, 0.1) (6.9, 8.8, 0.3) (5.5, 9.3, 2.0) (7.0, 11.5, 2.3)

Table 4.3. Coordinates in km of the points with relative maximum absolute values for the SPOP, SDOP ,SQOP and SOOP nuclei in figure 4.15.

References

[1] Alaia R., Patella D. and Mauriello P., 2008a, "Application of the geoelectrical 3D probability tomography in a test-site of the archaeological park of Pompei (Naples, Italy)", *J. Geophys. Eng.* **5** 67-76.

[2] Alaia R., Patella D. and Mauriello P., 2008b, "Imaging quadrupolar geophysical anomaly sources by 3D probability tomography. Application to near surface geoelectrical surveys", *J. Geophys. Eng.* **5** 359-70.

[3] Alaia R., Patella D. and Mauriello P., 2009a, "Imaging multipole gravity anomaly sources by 3D probability tomography ", submitted to *J. Geophys. Eng.*

[4] Alaia R., Patella D. and Mauriello P., 2009b, "Imaging multipole self-potential sources by 3D probability", submitted to *Progr. Electromag. Res*.

[5] Bewley R., Cole M., David A., Featherstone R., Payne A., and Small F., 1996, "New features within the hedge at Avebury", Wiltshire: Aerial and geophysical evidence: Antiquity, **70**, 639–646.

[6] Bhattacharya B., Shalivahan B., Jardani A. and Bera A., 2007, "Three dimensional probability tomography of self-potential anomalies of graphite and sulphide mineralization in Orissa and Rajasthan, India", *Near Surface Geophysics* **5** 223-30.

[7] Cammarano F., Di Fiore B., Patella D. and Mauriello P., 2000, "Examples of application of electrical tomographies and radar profiling to cultural heritage", *Ann. Geofis.* **43** 309–24.

[8] Cammarano F., Mauriello P., Patella D. and Piro S., 1997, "Application of geophysical methods to archaeological prospecting", *Sci. Technol. Cultural Heritage* **6** 151–73.

[9] Chianese D. and Lapenna V., 2007, "Magnetic probability tomography for environmental purposes: test measurements and field applications", *J. Geophys. Eng.* **4** 63-74.

[10] Corwin R. F., 1990, "The self-potential method for environmental and engineering applications," *Geotechnical and Environmental Geophysics, Vol. 1: Review and Tutorial*, S. H. Ward (ed.), 127-146, SEG, Tulsa.

[11] Dey A. and Morrison H.F, 1979, "Resistivity modelling for arbitrary shaped two dimensional structures", Geophysical Prospecting 27, 1020-1036.

[12] Di Fiore B., Mauriello P., Monna D. and Patella D., 2002, "Examples of application of the tensorial resistivity probability tomography to architectonic and archaeological targets", *Ann. Geophys.* **45** 417–29.

[13] Di Maio R., Mauriello P., Patella D., Petrillo Z., Piscitelli S. and Siniscalchi A., 1998, "Electric and electromagnetic outline of the Mount Somma-Vesuvius structural setting" *J. Volcanol. Geoth. Res*. **82** 219-38.

[14] Gnedenko B.V., 1979, "Kurs Teorii Verojatnostej", Mir, Moscow. Published in Italian with the title "Teoria della Probabilità", Editori Riuniti, Rome, 391p.

[15] Herbich T., Misiewicz K., and Teschauer O., 1997, "Multilevel resistivity prospecting of architectural remains: The Schwarzach case study", Archaeological Prospection, **4**, 105–112.

[16] Hesse A., 1999, "Multi-parametric survey for archaeology: how and why, or how and why not?",*J. Appl. Geophys.* **41** 157–68.

[17] Iuliano T., Mauriello P. and Patella D., 2001, "A probability tomography approach to the analysis of potential field data in the Campi Flegrei caldera (Italy)", *Ann. Geofis.* **44** 403–20.

[18] Iuliano T., Mauriello P. and Patella D. ,2002a, "Advanced magnetic visualization of the Mt.Vesuvius shallow plumbing system by probability tomography", *Ann. Geophys.* **45** 431–8.

[19] Iuliano T., Mauriello P. and Patella D., 2002b, "Looking inside Mount Vesuvius by potential fields integrated geophysical tomographies", *J. Volcanol. Geoth. Res.* **113** 363-78.

[20] Landau L. D. and Lifšits E. M., 1982, " *Elektrodinamika splošnych sred"*, Nauka, Moscow.

[21] Lapenna V., Patella D. and Piscitelli S. ,2000, "Tomographic analysis of self-potential data in a seismic area of southern Italy", *An. Geofis.* **43** 361-74.

[22] Loddo M., Patella D., Quarto R., Ruina G., Tramacere A. and Zito G., 1989, "Application of gravity and deep dipole geoelectrics in the volcanic area of Mt. Etna (Sicily)", *J. Volcanol. Geoth. Res.* **39** 17-39.

[23] Loke M. H. and Barker R. D., 1995, "Least-squares deconvolution of apparent resistivity pseudosections", *Geophysics* **60** 1682–90.

[24] Matias H. C., Monteiro Santos F. A., Rodrigues Ferreira F. E., Machado C. and Luzio R., 2006, "Detection of graves using the micro-resistivity method", *An. Geophys.* **49** 1235-44.

[25] Mauriello P., Monna D. and Patella D., 1998, "3D geoelectric tomography and archaeological applications", *Geophys. Prospect.* **46** 543–70.

[26] Mauriello P. and Patella D., 1999a, "Resistivity anomaly imaging by probability tomography", *Geophys. Prosp.* **47** 411-29.

[27] Mauriello P. and Patella D., 1999b, "Principles of probability tomography for natural-source electromagnetic induction fields", *Geophysics* **64** 1403-17.

[28] Mauriello P. and Patella D., 2001a, "Gravity probability tomography: a new tool for buried mass distribution imaging", *Geophys. Prosp.* **49** 1-12.

[29] Mauriello P. and Patella D., 2001b, "Localization of maximum-depth gravity anomaly sources by a distribution of equivalent point masses", *Geophysics* **66** 1431-37.

[30] Mauriello P. and Patella D., 2008a, "Localization of magnetic sources underground by a probability tomography approach", *Progr. Electromag. Res. M* **3** 27-56.

[31] Mauriello P. and Patella D., 2008b, "Resistivity tensor probability tomography", *Progr. Electromag. Res. B* **8** 129-46.

[32] Mauriello P. and Patella D., 2008c, "Geoelectrical anomalies imaged by polar and dipolar probability tomography", *Progr. Electromag. Res.*, Vol. 87, 63-88.

[33] Møller I., Jacobsen B. H. and Christensen N. B., 2001, "Rapid inversion of 2-D geoelectrical data by multichannel deconvolution", *Geophysics* **66** 800–8.

[34] Monteiro Santos F. A., Andrade A. R. and Dupis A., 2007, "2D joint inversion of dc and scalar audio-magnetotelluric data in the evaluation of low enthalpy geothermal fields", *J. Geophys. Eng.* **4** 53–62.

[35] Nyàri Z and Kanli A I 2007 Imaging of buried 3D objects by using electrical profiling methods with GPR and 3D geoelectrical measurements *J. Geophys. Eng.* **4** 83–93.

[36] Oldenburg D. W., and Li Y., 1994, "Inversion of induced polarization data" Geophysics, **59**, 1327–1341.

[37] Oldenburg D. W., McGillivary P. R., and Ellis R. G., 1993, "Generalized subspace method for large-scale inverse problems", Geophysical Journal International, **114**, 12–20.

[39] Parasnis D. S., 1997, "Principles of Applied Geophysics*",* Chapman & Hall London

[40] Park S. K. and Van G. P., 1991, "Inversion of pole–pole data for 3-D resistivity structure beneath arrays of electrodes", *Geophysics* **56** 951–60.

[41] Patella D., 1997a, "Introduction to ground surface self-potential tomography", *Geophys. Prosp.* **45**   653-81.

[42] Patella D., 1997b, "Self-potential global tomography including topographic effects", *Geophys. Prosp.* **45** 843-63.

[43] Patella D. and Mauriello P., 1999, "The geophysical contribution to the safeguard of historical sites in active volcanic areas. The Vesuvius case-history", *J. Appl. Geophys.* **41** 241–58.

[44] Principe C., Rosi M., Santacroce R. and Sbrana A., 1987, "Explanatory notes to the geological map", In: R. Santacroce (ed.), Somma-Vesuvius. Quaderni de «La Ricerca Scientifica», 114/8, CNR, Rome, 11-51.

[45] Roy A., and Apparao A., 1971, "Depth of investigation in direct current methods" Geophysics, v. 36, p. 943-959.

[46] Saracco G., Labazuy P. and Moreau F., 2004, "Localization of self potential sources in volcano-electric effect with complex continuous wavelet transform and electrical tomography methods for an active volcano", *Geophys. Res. Lett.* **31** 1-5.

[47] Sharma P., 1997, "Environmental and engineering geophysics", Cambridge University Press.

[48] Smekalova T., Abrahamsen N., and Voss O., 1996, "Magnetic investigation of a Roman/early Germanic Iron Age iron-smelting center at Snorup", Denmark: 6th Nordic Conference on the Application of Scientific Methods in Archaeology, Esbjerg Museum, 227–245.

[49] Spera F.J., De Vivo B., Ayuso R.A. and Belkin H.E. , 1998. Special issue: Vesuvius. *Journal of Volcanology and Geothermal Research*, **82**, 247 p.

[50] Soleimani M.., Mitchell C. N., Banasiak R., Wajman R. and Adler A., 2009, "Four-Dimensional Electrical Capacitance Tomography Imaging Using Experimental Data", *Progr. Electromag. Res.*, Vol. 90, 171-186.

[51] Soupios P. M., Georgakopoulos P., Papadopoulos N., Saltas V., Andreadakis A., Vallianatos F., Sarris A. and Makris J. P., 2007, "Use of engineering geophysics to investigate a site for a building foundation", *J. Geophys. Eng.* **4** 94–103.

[52] Steeples D. W., 2001, "Engineering and environmental geophysics at the millennium", Geophysics, **66**, 31–35. Swank, J., 1892, History of the manufacture of iron in all ages: The American Geophysics, v. 39, p. 190-204.

[53] Takács E., Pethő G. and Szabó I., 2005, "Comparative investigations about the applicability of current density pseudosections in the interpretation of 2D VLF vertical magnetic anomalies", *Acta Geod. Geophys. Hung.* **40** 127-46.

[54] Varga M., Novàk A. and Szarka L., 2008, "Application of tensorial electrical resistivity mapping to archaeological prospection", *Near Surf. Geophys.* **6** 39–47.

[55] Weston, D. G., 2001, "Alluvium and geophysical prospection", Archaeological Prospection, **8**, 265–272.

[56] Witten A., Won I. J., and Norton S., 1997, "Imaging underground structures using broadband electromagnetic induction", Journal of Environmental and Engineering Geophysics, **2**, 105–114.

[57] Witten, A., Calvert G., Witten B., and Levy T., 2003, "Magnetic and electromagnetic induction studies at archaeological sites in southwestern Jordan", Journal of Environmental and Engineering Geophysics, **8**, 209–215.

[58] Won I. J., Keiswetter D., and Novikova E., 1998, "Electromagnetic induction spectroscopy", Journal of Environmental and Engineering Geophysics, **3**, 27–40.

[59] Zhou B. and Greenhalgh S. A., 2002, "Rapid 2-D/3-D crosshole resistivity imaging using the analytic sensitivity function", *Geophysics* **67** 755–65.

[60] Zlotnicki J. and Nishida Y., 2003, "Review on morphological insights of self-potential anomalies on volcanoes" *Surveys in Geophysics*, **24**, 291-338.